ISSN No. 0737-5352-35

AEROSOL HYGROSCOPICITY AND VISIBILITY ESTIMATES IN THE GREAT SMOKY MOUNTAINS NATIONAL PARK

Jenny L. Hand and Sonia M. Kreidenweis

Department of Atmospheric Science
Colorado State University
Fort Collins, CO

Funding Agency:
National Park Service # 1443-CA0001-920006, AMD#5/SUB#3

June, 1997

CIRA Cooperative Institute for Research in the Atmosphere

Colorado State University

AEROSOL HYGROSCOPICITY AND VISIBILITY ESTIMATES IN THE GREAT SMOKY MOUNTAINS NATIONAL PARK

Jenny L. Hand
Sonia M. Kreidenweis

Department of Atmospheric Science
Colorado State University
Fort Collins, CO

ABSTRACT

Summertime visibility in the National Parks in the Eastern United States is often very poor, due to high particulate mass concentrations and high relative humidities. As a part of the Southeastern Aerosol and Visibility Study (SEAVS) in the Great Smoky Mountains National Park during the summer of 1995, aerosol size distributions (D_p = 0.1-3 μm) were measured with an Active Scattering Aerosol Spectrometer (ASASP-X). A relative humidity (RH) controlled inlet allowed for both dry and humidified measurements. The objective of this experiment was to examine the aerosol size distribution and its variation with RH to characterize its effect on visibility in the region.

The ASASP-X was calibrated with polystyrene latex spheres (PSL) (m = 1.588), however, the instrument response was sensitive to the refractive index of the measured particles, which was typically much lower than that of PSL. An inversion technique accounting for varying particle real refractive index was developed to invert ASASP-X data to particle size.

Dry (RH < 15%) particle refractive indices were calculated using the partial molar refractive index method and 12-hour fine aerosol (< 2.5 μm) chemical compositions from the National Park Service Interagency Monitoring of Protected Visual Environments (IMPROVE) filter samples. A study average dry refractive index of $m = 1.49 \pm 0.02$ was determined. The dry aerosol number distributions inverted using the scaling method were fit with single mode lognormal curves, resulting in dry accumulation mode size parameters. A study average total volume concentration of 7 ± 5 μm^3 cm^{-3} was determined, with a maximum value of 26 μm^3 cm^{-3}. The large variability was due to extremes in meteorological situations occurring during the study. The study average volume median diameter was 0.18 ± 0.03 μm, with an average geometric standard deviation of 1.45 ± 0.06.

A newly-developed iteration method was used to determine wet refractive indices, wet accumulation mode volume concentrations and water mass concentrations as a function of relative humidity. Theoretical predictions of water mass concentrations were determined using a chemical equilibrium model assuming only ammonium and sulfate were hygroscopic. Comparisons of predicted and experimental water mass showed agreement within experimental uncertainties.

To examine the effects of particles on visibility, particle light scattering coefficients, b_{sp}, were calculated with derived size parameters, refractive index and Mie theory. Dry scattering agreed well with nephelometer measurements made at SEAVS, with an average b_{sp} of 0.0406 km^{-1}. Estimates of particle light scattering growth (b/b_o) were determined from ratios of wet and dry light scattering coefficients, and also agreed with nephelometer results.

The new inversion techniques were compared to earlier, simpler methods which ignored variations in aerosol chemical composition. The simpler method yielded smaller mean diameters, however, hygroscopicity estimates were comparable to those derived using daily varying chemical composition. This suggests that although the aerosol chemical composition is needed to determine aerosol size parameters, it may not be critical for deriving hygroscopicity (or other ratios of size parameters). This result may be specific to this study, as the variation in refractive index with RH assumed by previous models appears to be a good estimate for that observed during SEAVS.

ACKNOWLEDGMENTS

We would like to thank the following people at CSU for their support of this work: Rodger Ames, Derek Day, Eli Sherman, and Brian Jesse.

Several people at the Air Quality Division of the National Park Service/CIRA also contributed to this work: William Malm, Kirk Fuller, and Jim Sisler. To them we also express our gratitude.

Several people generously allowed us to use their computer programs in this work. Dr. Chris Pilinis of the University of Miami provided his EQUILIB program for estimating water mass concentration. Dr. Alfred Wiedensohler at the Institute of Tropospheric Research in Leipzig, Germany, made Evan Whitby's DISTFIT lognormal fitting program available to use with our aerosol size distributions. Dr. Peter McMurry and Bill Dick from the University of Minnesota provided helpful suggestions in deriving a scaling technique for data inversion.

Jenny Hand expresses her appreciation to her advisor, Dr. Sonia Kreidenweis, for her enthusiasm and availability during the course of this work. My gratitude also goes to Dr. Jeff Collett and Dr. Marty Fettman who gave of their time and helpful suggestions as committee members. Appreciation should also be extended to the CSU Atmospheric Chemistry group (especially Debra Y. Harrington) for their helpful suggestions in the preparation of this thesis. I must extend my overwhelming gratitude to my family: Mike, Ruth, Sharon, Dolan, and Cory, without whose help I am certain I would not have finished on time. And of course, Teegan, who provided so much laughter.

This research was supported by the National Park Service under contract number 1443-CA0001-920006, AMD#5/SUB#3

TABLE OF CONTENTS

APPENDICES

LIST OF TABLES

LIST OF FIGURES

FIGURES IN APPENDICES

APPENDIX A

APPENDIX B

CHAPTER 1. INTRODUCTION

In 1988, several national agencies (Environmental Protection Agency, Fish and Wildlife Service, Bureau of Land Management, National Park Service, and the Forest Service) initiated a national visibility and aerosol monitoring network to determine spatial and temporal trends in aerosol composition and related visibility reduction. The monitoring network was named IMPROVE (Interagency Monitoring of Protected Visual Environments) (Malm *et al.*, 1994a). One of the major objectives of IMPROVE was to characterize the background visibility in several regions of the United States. Along with particle light scattering and extinction, aerosol mass concentration and composition are measured at designated IMPROVE sites, one of which is the Great Smoky Mountains National Park (GRSM). The major visibility-reducing aerosol constituents were determined to be sulfates, nitrates, organics, elemental (absorbing) carbon, and soil. In most regions of the United States, sulfates and organics were primarily responsible for light extinction, however, in Southern California, nitrates were the major contributing factor in visibility reduction. Further discussion of temporal and spatial trends of aerosol loading and particle light extinction were reported by Malm *et al* . (1994a).

During the summer of 1995, the Southeastern Aerosol and Visibility Study (SEAVS) was conducted in the GRSM to continue the investigation of the spatial and temporal trends in aerosol composition and visibility reduction. Previous IMPROVE monitoring studies have shown that in the GRSM, temporal trends demonstrated higher concentrations of major aerosol constituents and correspondingly higher light extinction during summer (Malm *et al.*, 1994a). The high ambient relative humidities persisting in the study region lead to visibility issues due to aerosol growth from water uptake.

The objectives of CSU's involvement in SEAVS included measuring wet and dry aerosol size distributions to determine particle hygroscopicity. A Particle Measuring Systems (PMS) Active Scattering Aerosol Spectrometer (ASASP-X) was used to measure aerosol number distributions. A relative humidity controlled inlet allowed measurements to be performed at specific relative humidities. Measurements of aerosol number distributions at high and low relative humidities provided estimates of aerosol hygroscopicity. Experimental details can be found in Ames and Kreidenweis (1996).

Calibration of the ASASP-X instrument response for particles of varying refractive index was performed by applying a diameter scaling method based on refractive index developed for this purpose. Literature values of refractive index as a function of relative humidity (Shettle and Fenn, 1979) were initially applied in the data inversion. Dry (RH < 15%) daily varying refractive indices computed from IMPROVE aerosol chemical compositions were later applied. Accumulation mode number distributions derived from the data inversion were fit with a lognormal fitting program (DISTFIT, Whitby, 1991), from which accumulation mode lognormal size parameters were determined.

Calculations of daily dry real refractive indices were made using the partial molar refractive index method (Stelson, 1990). Chemical compounds (IMPROVE) included in the calculation were sulfate and ammonium (with associated hydrogen), organic carbon, and potassium nitrate. A small amount of water consistent with an ammonium bisulfate compound at 15% relative humidity was also included. Volume weighted refractive indices were computed for comparison, and the two methods were in good agreement. Complex refractive indices were calculated separately by including elemental carbon.

Wet refractive indices were determined using a newly-developed iterative method. Inputs included dry aerosol density, dry refractive index, aerosol mass and dry accumulation mode volume concentration (derived from the ASASP-X). Wet refractive indices were used to invert high relative humidity ASASP-X size distributions. Water mass was determined with the iterative method and compared to thermodynamically

predicted water mass assuming only ammonium and sulfate were hygroscopic (EQUILIB, Pilinis and Seinfeld, 1987). Comparisons of water mass ratios showed scatter around a 1:1 line, with 33 of the 61 total values corresponding to larger theoretical water mass ratios.

Results presented in this thesis include dry accumulation mode size parameters, particle light scattering coefficients (b_{sp}), light scattering growth curves (b/b_o), and particle hygroscopicity calculated from ratios of accumulation mode volume concentrations and volume median diameters. All of the results were calculated in two ways: from distributions inverted with a rural aerosol model of refractive index, and using the daily varying wet and dry refractive indices calculated in this thesis. Dry accumulation mode parameters calculated from daily varying refractive indices increased slightly when compared to those calculated using the rural aerosol model. Comparisons of hygroscopicity results suggested that this difference may cancel when ratioing parameters, resulting in similar aerosol growth values. Knowledge of the aerosol composition may therefore not be critical in making such observations.

Section 1.1. Experimental Background

Details of the experimental measurements taken during the SEAVS study were provided in Ames and Kreidenweis (1996), however, a general overview will be provided here to familiarize the reader with the motivation and methods for obtaining data, and to place the remainder of the thesis in context.

The field sight was located at Look Rock Tower (near Abrams Creek) at an elevation of 793 meters, on the western edge of the Great Smoky Mountains National Park overlooking the Tennessee Valley and Cumberland Plateau. Figure 1.1 illustrates the location of the sampling site and surrounding topography (Sherman *et al.*, 1997). The National Park Service/ Colorado State University study included the following measurement objectives: total particle number concentrations, determination of relative

humidity (RH) dependent aerosol size distributions, RH dependent and ambient particle light scattering measurements, and local meteorological conditions (Ames and Kreidenweis, 1996).

Relative humidity dependent measurements were performed daily using a RH controlled inlet, from which a radiance research nephelometer and an optical particle counter (ASASP-X) sampled. Total particle number concentration was measured with a Condensation Nuclei Counter (CNC) both night and day. Ambient light scattering was measured with a bank of nephelometers. All experimental details of the measuring system and protocol can be found in Ames and Kreidenweis (1996) and Day *et al* . (1996).

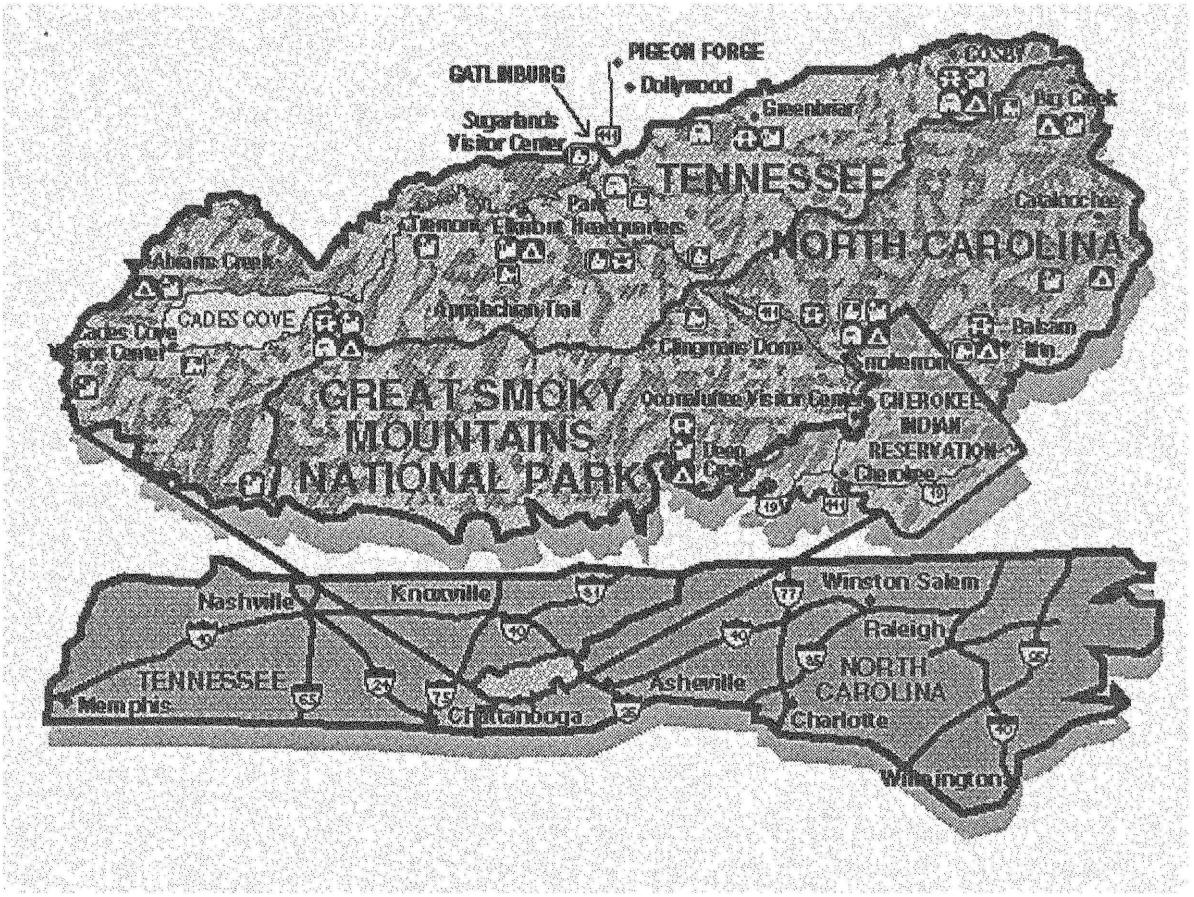

Figure 1.1 Great Smoky Mountains National Park and surrounding area (Sherman *et al.* 1997).

Unique meteorological periods occurring during SEAVS were characterized by Sherman *et al.* (1997). Table 1.1 summarizes specific meteorological events. These events

will be investigated in more detail later by evaluating differences in chemical composition, aerosol size parameters, and light scattering measurements during each period.

Table 1.1 Meteorological periods during SEAVS, as defined by Sherman *et al.* (1997). Classification of study periods was based on visibility conditions and synoptic scale air mass source regions.

Descriptor	*Calendar dates*	*Julian dates*	*Percent days (1988 - 1995) with larger visual range*	*Air mass category*
Study Beginning	7/21–7/22	202–203	79 %	Tr
Dust Event	7/23–7/26	204–207	33 %	Tr to mT-g to cP2
Post-Dust Event	7/27–7/28	208–209	45 %	Tr to mT-a
Hurricane–Influenced Period				
Pre-Hurricane Erin	7/29–8/2	210–214	42 %	Tr to mT
Hurricane Erin	8/3–8/5	215–217	8 %	mT-a to Tr
Post-Hurricane Erin	8/6–8/8	218–220	71 %	Tr; mT-g influence
Stagnation Period				
Transition	8/9–8/13	221–225	95.5 %	Tr to cP2
Hazy	8/14–8/18	226–230	> 98 %	cP2
Post-Hazy	8/19–8/20	232–233	95 %	Tr
cPk	8/21–8/22	234–235	> 98 %	cPk
Ending	8/23–8/24	236–237	35 %	cP2 to mT-a

CHAPTER 2: OPTICAL PARTICLE COUNTER

2.1. Theory

The optical particle counter used in this study was a Particle Measuring Systems (PMS) Active Scattering Aerosol Spectrometer Probe (ASASP-X). The measuring range of the ASASP-X (D_p = 0.09 to 3.00 μm) is divided into four overlapping size ranges, each with 15 size channels. Particles were sized with the following method. The light scattered by a particle passing through a He-Ne laser (λ=632.8 nm) was focused to a photodiode, which converted the intensity to a voltage. Depending on the magnitude of the voltage, the particle was classified into a particular size channel. This sizing depended upon the manufacturer calibration which determined the relationship between voltage and size channel. The standardized calibration performed by PMS for the ASASP-X included polystyrene latex spheres (PSL) and glass beads. For each of the four ranges, discriminator level voltages (DLV) were defined for each of the 15 size channels. Each range was normalized, so that the DLV varied from 0 to 10 volts. The voltage was amplified by programmable amplifiers allowing it to be related to a specific diameter for all four ranges. The largest diameter range (range 0) corresponded to the smallest gain (smallest voltage amplification). For smaller size ranges, the voltage decreased and the range relative gain increased. A diameter-voltage relationship was thus established by the manufacturer. Figure 2.1.1 demonstrates the DLV for all ranges when normalized between 0 and 10 volts.

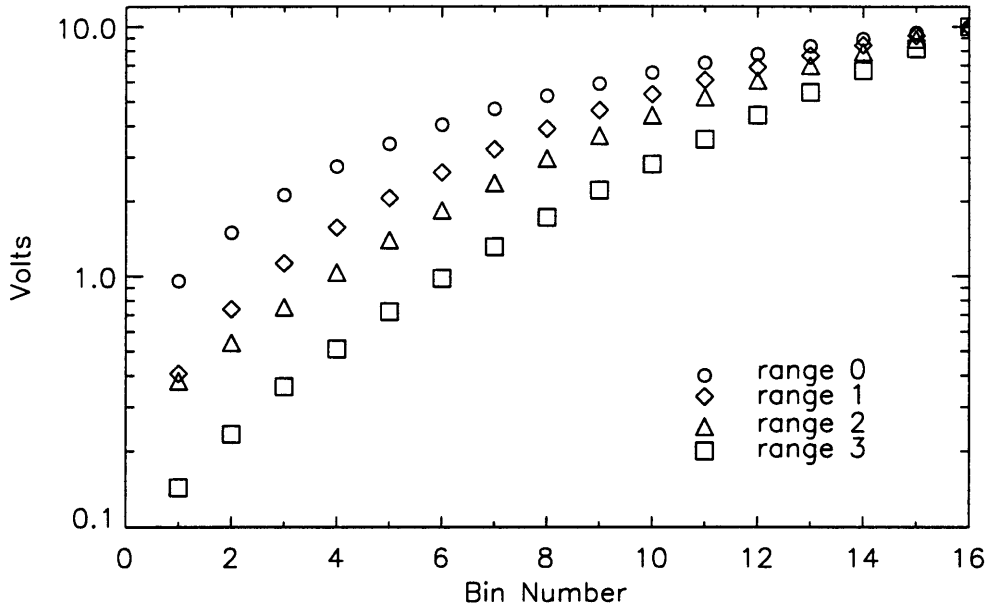

Figure 2.1.1. Discriminator level voltages (DLV) for the ASASP-X ranges.

Not taken into account during this calibration was the effect of refractive index on the light scattered from the particle. The smoothed manufacturer calibration was based on PSL spheres (m =1.588-0i) , and the resulting empirical relationship between voltage and diameter assumed the instrument was insensitive to the optical properties of measured particles (PMS Manual, 1977). To correct the calibration for particles of other refractive index, Mie scattering theory was employed which assumed measured particles were spherical. Following the methods of Garvey and Pinnick (1983), Pinnick and Auvermann (1979), and Kim and Boatman (1990), the theoretical scattering response for the ASASP-X was calculated using the following equation:

$$R = \frac{\pi}{k^2}\int_{\alpha}^{\beta}\left[\left|S_1(\theta) + S_1(\pi-\theta)\right|^2\right] + \left[\left|S_2(\theta) + S_2(\pi-\theta)\right|^2\right]\sin\theta\, d\theta \qquad (2.1.1)$$

where $S_1(x, m, \theta)$ and $S_2(x, m, \theta)$ are the Mie scattering functions corresponding to light with its electric vector polarized perpendicular and parallel to the scattering plane, respectively. These functions depend on the index of refraction, m, the particle size parameter, $x=kr$ (k is the wavenumber and r is the particle radius), and the scattering angle θ. The integration is from $\alpha = 35°$ to $\beta = 120°$, corresponding to the optics in the ASASP-X. The BHMIE code provided in Bohren and Huffman (1983) was used to calculate $S_1(x, m, \theta)$ and $S_2(x, m, \theta)$. Theoretical response functions were then calculated for particles of different refractive index. Figure 2.1.2 provides examples of theoretical response functions for different real refractive indices.

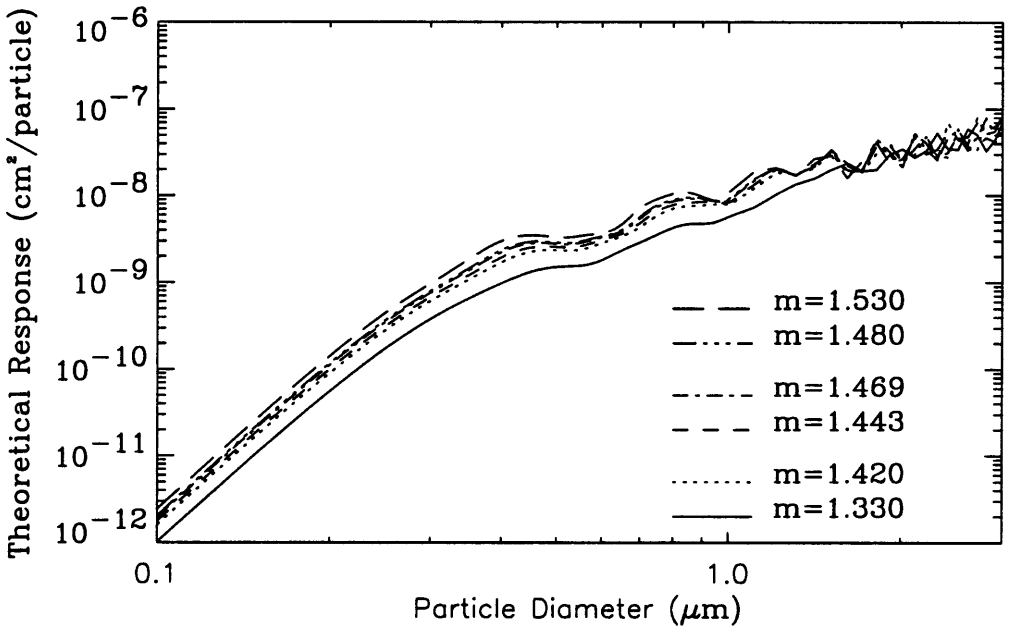

Figure 2.1.2. Theoretical response functions for the ASASP-X.

The experimental voltage was related to theoretical response by converting voltage (DLV) to a scattering cross-section (TR) using the following equation:

$$TR = \frac{DLV}{NC \cdot RG} \qquad (2.1.2)$$

where NC is the normalization constant (V cm^{-2}) and RG is the relative gain of a specific range. Determination of NC and RG will be discussed in Section 2.3.

Refractive indices of atmospheric aerosols are generally significantly lower than that of PSL (Stelson, 1990). By not correcting the instrument calibration for true refractive index of a particle, measured sizes are underestimated, as reported by other researchers (Hering and McMurry, 1991; Kim and Boatman, 1990; Hand and Kreidenweis, 1996; Kim, 1995). This underestimation of aerosol size due to instrument calibration was the main motivation for developing a unique calibration for the ASASP-X in this thesis. The following sections detail the development of this calibration.

Section 2.2. Calibration

The calibration for the ASASP-X used in this thesis required determining the values of the discriminator level voltages (DLV) for each diameter size channel, relative gains for each range, and a normalization constant used to relate theoretical scattering cross-sections to experimental voltage values. The calibration developed here differs somewhat from that derived in Ames and Kreidenweis (1996) for the same instrument; sensitivity of results to calibration procedures will be investigated by comparing results derived from two different calibration methods (see Appendix A2).

Although the ASASP-X operating manual provided the values of discriminator level voltages, they were measured for this instrument after the field study concluded. Details and descriptions of these measurements can be found in Ames and Kreidenweis (1996), where the first experimental values determined were used in this work. These voltage values agree very well with those reported in the PMS manual.

To determine the relationship between theoretical particle scattering and experimental voltages, measurements of PSL spheres were made because of their known monodisperse size and refractive index. Six sizes of PSL spheres from Interfacial Dynamic Corporation were used to calibrate the ASASP-X: 0.19, 0.25, 0.30, 0.41, 0.47, and 0.87 μm diameter. Calibrations were performed both in the field and in the Atmospheric Simulation Laboratory at CSU after the conclusion of the study. PSL spheres were atomized and sampled with the ASASP-X both from the atomizer and after passing through a differential mobility analyzer (DMA) set to the corresponding voltage/size. The ASASP-X channel corresponding to the maximum counts for a given size during these measurements was the same for both sampling methods. More detailed discussion of this experiment can be found in Ames and Kreidenweis (1996). These measurements were used in this thesis to determine the relative gain and normalization constant for the ASASP-X.

The measured DLV for each range were used to determine gain amplification. The channel voltage corresponding to the same diameter (assigned by PMS) in two consecutive ranges were ratioed to determine the gain between two ranges. For example, range 1, channels 10 and 14 overlap with range 0, channels 1 and 2. The lower limit channel voltage of range 1, channel 10 (0.957 V) was ratioed to range 1, channel 10 (5.356 V) to obtain a gain of 5.5967 between ranges 0 and 1. An average of all the overlapping channels between these two ranges resulted in a gain of 5.62. This procedure was repeated for the other consecutive ranges to obtain average gain values between the other ranges. Figure 2.2.1 shows discriminator level voltages for all ranges normalized by their respective relative gains, resulting in a smooth, continuous calibration curve.

Because the PMS diameter assigned to a particular bin may not be accurate, the measurements of PSL spheres with diameters existing in the overlapping region of two size ranges were used to determine gain amplification as a check on the values used to obtain Figure 2.2.1. For each measurement, the channel corresponding to maximum counts was

recorded for the respective range. The upper and lower limit discriminator level voltages corresponding to the maximum count channel were averaged to obtain one voltage value per channel, referred to as the maximum channel voltage (V_M). For two overlapping ranges, V_M was ratioed to obtain the gain value between the two ranges. The same procedure was performed for relevant PSL sizes in other ranges. Gains between ranges 0-1, 1-2, and 2-3 were obtained and then normalized by the gain for range 0. These values were typically within ± 20% of those derived from the first method described, using PMS defined diameter bins (Figure 2.2.1).

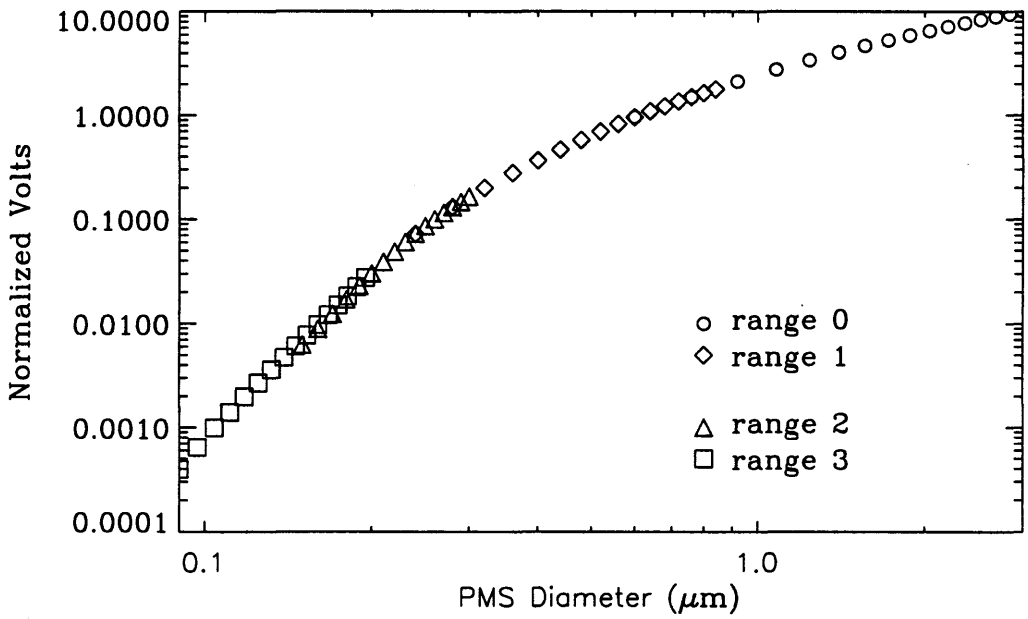

Figure 2.2.1. Discriminator level voltages normalized by relative gain for the ASASP-X, derived using overlapping size channels.

The relative gains (relative to range 0) used to create Figure 2.2.1 are reported in Table 2.2.1. Also reported in Table 2.2.1 are gain values from other investigators for comparison. Notice that the voltages in Figure 2.2.1 now fall between 0.0001 and 10 V in comparison to Figure 2.1.1 due to the normalization by relative gain.

To determine the normalization constant (V cm^{-2}) which relates voltage to theoretical response, Mie scattering response was calculated for m=1.588 (PSL) at each of the PSL diameters used in the calibration. The maximum channel voltage (V_M) in which that particle appeared was divided by the calculated scattering response value (cm^2). For the various PSL sizes included in the calibration, an average NC of 1.4×10^8 V cm^{-2} was obtained. The product of NC and RG (denoted C) provides a comparison of the constant used to normalize each range. These values are also found in Table 2.2.1, along with values used in previous studies.

Table 2.2.1 Relative gains for each range, with the corresponding normalization constant.

Range	Garvey & Pinnick (1983)		Ames & Kreidenweis (1996)		Current Calibration	
	Gain	C	Gain	C	Gain	C
0	1	1.9×10^8	1	1.65×10^8	1	1.4×10^8
1	6.321	1.2×10^9	4.02	6.63×10^8	5.62	7.87×10^8
2	67.81	1.29×10^{10}	51.21	8.45×10^9	60.68	8.50×10^9
3	441.0	8.38×10^{10}	341.82	5.64×10^{10}	364.22	5.10×10^{10}
NC (Vcm^{-2})	1.9×10^8		1.65×10^8		1.4×10^8	

The constants derived in this thesis tend to be lower, or fall between the constants presented by other investigators. The effects of this smaller normalization constant will be investigated in Appendix A2. Determination of channel limit diameter is discussed in the following section.

Section 2.3. Determination of Channel Diameters

To determine the diameter-channel relationship, the normalization constant, NC, derived in the previous section was used to relate the PSL theoretical response to the

normalized DLV in each range. Two diameter-channel relationships will be derived in this section, those for m=1.588 (PSL) and m=1.530, corresponding to dry ammonium sulfate. Figure 2.3.1 shows the Mie theoretical response for m=1.588 (PSL). Also plotted on Figure 2.3.1 is the diameter-voltage relationship for PMS defined diameters with DLV converted to scattering response using NC =1.4×10^{8} V cm^{-2}. For smaller particles, a shift in diameter values was required because the PMS defined channel-diameters do not fall directly on the Mie theoretical scattering response. The newly-defined diameters required to "match up" channel limit scattering response and Mie theoretical response were determined by an interpolation method. Figure 2.3.1 demonstrates the differences between these diameters.

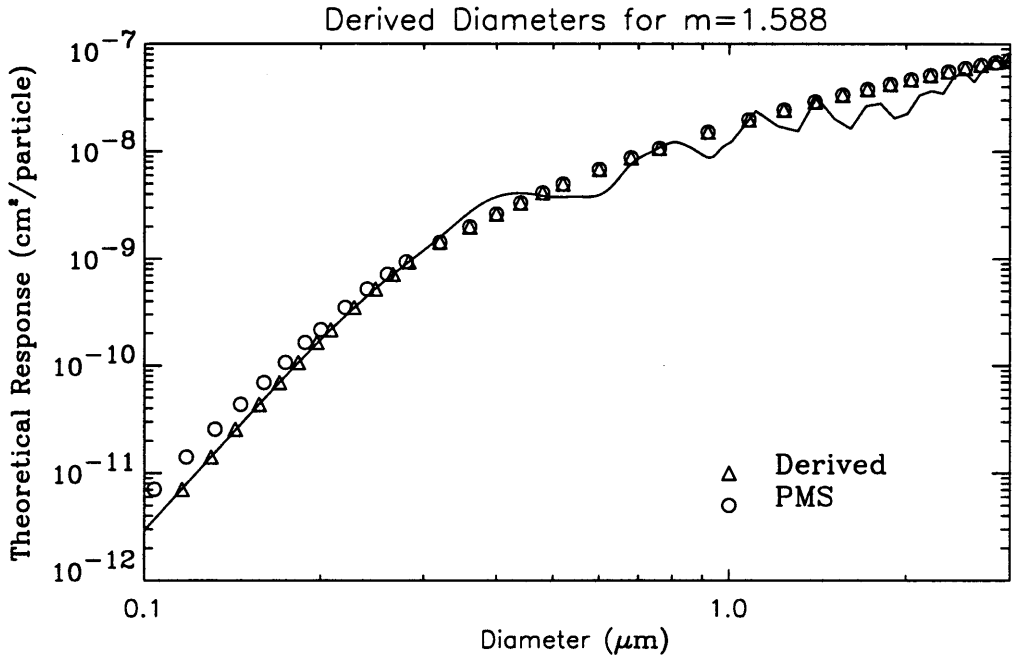

Figure 2.3.1 Derived and PMS diameters for PSL (m =1.588).

Due to the overlapping nature of the ASASP-X size ranges, a scheme for dealing with measured counts in the overlapping size channels was required. In developing this

scheme, the 60 original size channels were reduced to 34. As discussed in Ames and Kreidenweis (1996), the discriminator level voltages in ranges 2 and 3 had more experimental measurement uncertainty than in the larger size ranges. In these lowest two ranges, two to three size channels were grouped together to account for the noise in voltage measurements. In the lowest size range (range 3), the first and second channels were discarded completely. In other ranges, 2 to 3 consecutive size channels were grouped together, leading to fewer overall channels. This method was similar to that in Ames and Kreidenweis (1996). The overlapping scheme used in this work was simplified by the continuous voltage calibration curve derived in the previous section. The size channels in overlapping regions lie directly on top of one another (see Figure 2.2.1), allowing for some channels to be discarded. The particles with diameters corresponding to the upper end of a size range were sized with more precision than at the lower end (PMS Manual, 1977). Whenever possible, the lower channels of an overlapping range were therefore discarded while the upper channels of the smaller range were retained. This method for dealing with overlapping size ranges resulted in no averaging of counts between channels.

Previous researchers have investigated the effects of the multivalued region of the Mie theoretical response on size distributions (Hering and McMurry, 1990; Kim, 1995, Richards *et al.*, 1985; Pueschel *et al.*, 1990). For PSL, this region occurs around D_p = 0.4- 0.6 μm (see Figure 2.3.1). For a particular theoretical response, a unique diameter cannot be determined in this range. In deriving size channels in this region, two methods were investigated: smoothing through the region, and lumping the entire diameter range into one channel. Although the lumped diameter method seemed more appropriate, applying it in the calibration resulted in unusual peaks and dips in the number distributions which were suspect. Similar results were obtained by Pueschel *et. al* (1990) for a similar calibration. A smoothed set of diameters falling parallel to the original PMS calibration was therefore applied in the multivalued region. The resonances in the Mie theoretical response curve corresponding to $D_p > 1.0$ μm made it difficult to assign diameters to size channels

in this region. PMS defined diameters were therefore chosen in the largest size range (range 0).

The final 34 size channels correspond to a specific set of scattering response values (cm^2). These scattering values remain constant; determining the corresponding particle diameters for a different refractive index requires shifting the diameters to the respective Mie theoretical response curve (Hand and Kreidenweis, 1996). Figures 2.3.1 and 2.3.2 show the resulting channels for m=1.588 and m=1.530. Table 2.3.1 reports the lower channel limit scattering response and diameter derived for m = 1.588 and m = 1.530.

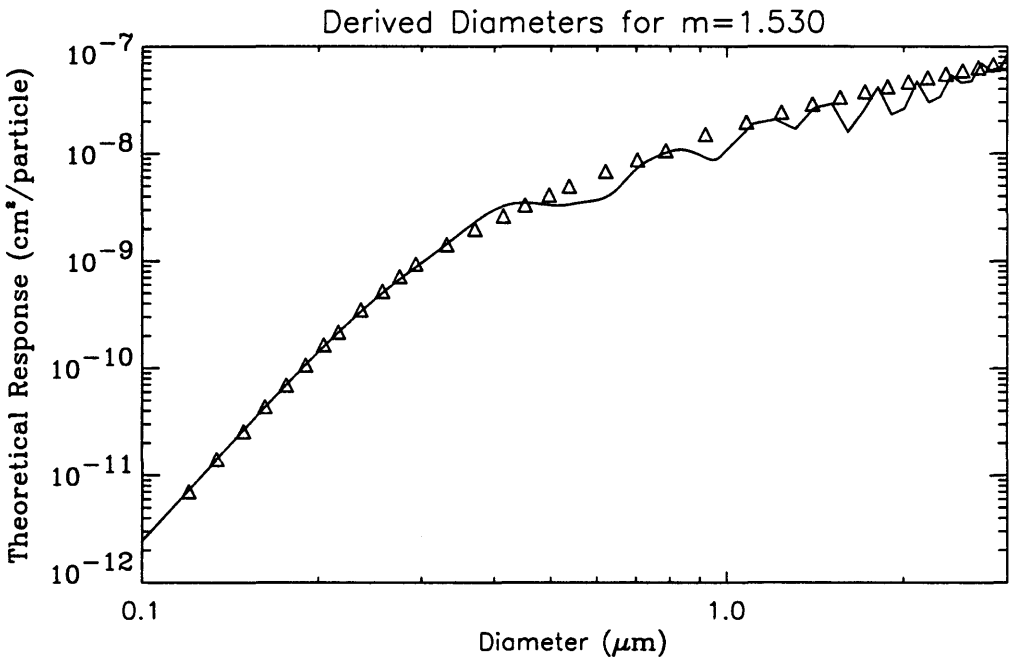

Figure 2.3.2. Derived diameters for m = 1.530, with the corresponding Mie theoretical response.

Two consistency checks were made on this diameter set. The first check was performed using PSL calibration measurements. The PSL data were inverted using the derived smoothed diameter set for m = 1.588. A lognormal fitting program (DISTFIT, Whitby, 1991) was applied to the resulting number distributions. The calculated number

Table 2.3.1. Lower limit channel response and diameter for m = 1.588 and m=1.530.

Bin	Scattering Cross-Section (cm^{-2})	m= 1.588 D_p (μm)	m=1.530 D_p (μm)
1	7.0856×10^{-12}	0.116	0.120
2	1.4128×10^{-11}	0.130	0.134
3	2.5671×10^{-11}	0.143	0.149
4	4.3478×10^{-11}	0.157	0.162
5	6.9424×10^{-11}	0.170	0.176
6	1.0682×10^{-10}	0.183	0.190
7	1.6430×10^{-10}	0.197	0.204
8	2.1621×10^{-10}	0.208	0.216
9	3.4936×10^{-10}	0.228	0.236
10	5.1980×10^{-10}	0.248	0.257
11	7.1496×10^{-10}	0.266	0.275
12	9.3706×10^{-10}	0.283	0.293
13	1.4306×10^{-9}	0.320	0.331
14	1.9887×10^{-9}	0.360	0.370
15	2.6176×10^{-9}	0.400	0.414
16	3.3149×10^{-9}	0.440	0.452
17	4.1036×10^{-9}	0.480	0.497
18	4.9609×10^{-9}	0.520	0.538
19	6.8025×10^{-9}	0.600	0.621
20	8.7250×10^{-9}	0.680	0.704
21	1.0663×10^{-8}	0.760	0.787
22	1.5136×10^{-8}	0.920	0.920
23	1.9700×10^{-8}	1.08	1.08
24	2.4286×10^{-8}	1.24	1.24
25	2.8936×10^{-8}	1.40	1.40
26	3.3493×10^{-8}	1.56	1.56
27	3.7757×10^{-8}	1.72	1.72
28	4.2193×10^{-8}	1.88	1.88
29	4.6643×10^{-8}	2.04	2.04
30	5.1086×10^{-8}	2.20	2.20
31	5.5379×10^{-8}	2.36	2.36
32	5.9629×10^{-8}	2.52	2.52
33	6.3707×10^{-8}	2.68	2.68
34	6.7567×10^{-8}	2.84	2.84
	7.1471×10^{-8}	3.00	3.00

median diameter was compared to the indicated PSL diameter, to determine if the particles were sized correctly. Of particular interest was the comparison of PSL particle sizes in the multivalue region. For the instrument calibrations performed during SEAVS with 0.41 μm PSL particles, an average number median diameter of 0.413 ± 0.007 μm was determined. Figure 2.3.3 provides an example of a PSL (0.41 μm) number distribution and corresponding lognormal curve fit.

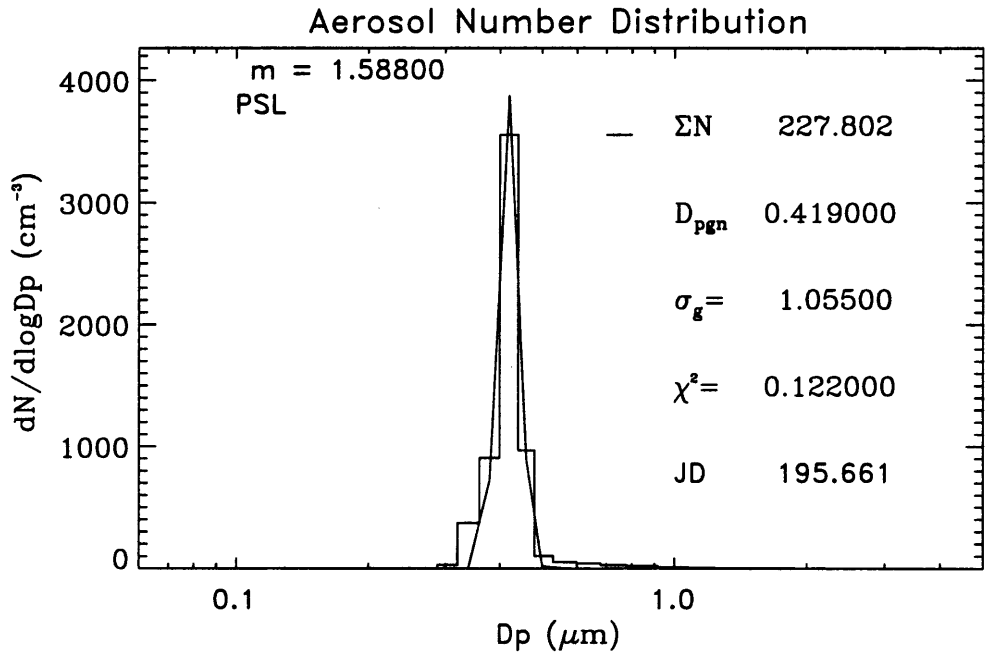

Figure 2.3.3. PSL (D_p = 0.41 μm) number distribution and lognormal fit.

This check was also used to investigate the effects of a lumped versus smoothed diameter set through the multivalue region. When using a lumped diameter channel in the multivalue region, fit number median diameters were different from the known PSL diameters due to the width of the channel where maximum counts occurred. The distribution was also fit with a larger geometric standard deviation. For the smoothed

diameter set, the median diameters always agreed very well with PSL indicated diameters, and reasonable geometric standard deviations were determined. It should be noted that for the 0.21 μm PSL, the lognormal curve fits consistently resulted in a median diameter of 0.25 μm, while the 0.19 μm PSL particles agreed well with the lognormal number median diameter. Because both of these PSL particles were sized in range 2 (two to three channels apart), it was concluded that there was some discrepancy with the 0.21 μm PSL spheres.

The second check performed on the diameter set involved the overlapping size ranges. As noted in Figure 2.2.1, when normalized by the appropriate relative gain, the discriminator level voltages resulted in a continuous calibration curve. For the overlapping size channels, the number of counts in each channel should be the same. For example, in range 3, channels 10-13 overlap with range 2, channel 1. The sum of the counts in channels 10-13 (range 3) and the counts in channel 1 (range 2) should be the same if the relative gains were appropriate. For all ranges, these comparisons were very close, with an average percent difference in counts of 0.01%. Based on these checks, the diameters derived in this thesis were assumed to be an appropriate calibration choice and were used to invert ASASP-X data.

Section 2.4. Diameter Scaling Method

The re-calibration of channel diameters based on refractive index in Section 2.3 was a time-consuming and tedious process. A method by which a set of diameters could be scaled based on refractive index was needed and will be developed in this section. The motivation for developing a scaling method will become apparent in Chapter 4 when daily varying refractive indices of dry aerosol measured during SEAVS will be calculated. Speedy derivation of diameters for arbitrary refractive index will be essential for ASASP-X data inversion.

As seen in Figure 2.1.2, Mie theoretical response curves (*TR*) for a variety of real refractive indices have basically the same shape: linear from D_p 0.1 ~ 0.4 μm, a resonance (multivalue) region from D_p = 0.4 ~ 0.6 μm, and resonances when D_p > 1 μm. Being able to relate Mie scattering curves to one another was essential in this scaling process. The theoretical response for a 0.1 μm diameter particle for real refractive indices ranging from m =1.33 to 1.530 were calculated from equation (2.1.1). The ratio of the theoretical response value at D_p = 0.1 μm for a given refractive index (TR_i) and for that of m = 1.530 ($TR_{1.530}$) was determined, as in equation (2.4.1):

$$f_{TR,i} = \frac{TR_{1.530}}{TR_i} \qquad (2.4.1)$$

Scattering values for particle diameters ranging from 0.1 - 3.0 μm corresponding to a given refractive index were multiplied by f_{TR} , resulting in a "collapse" of the Mie curve to the m = 1.530 position (see Figure 2.4.1).

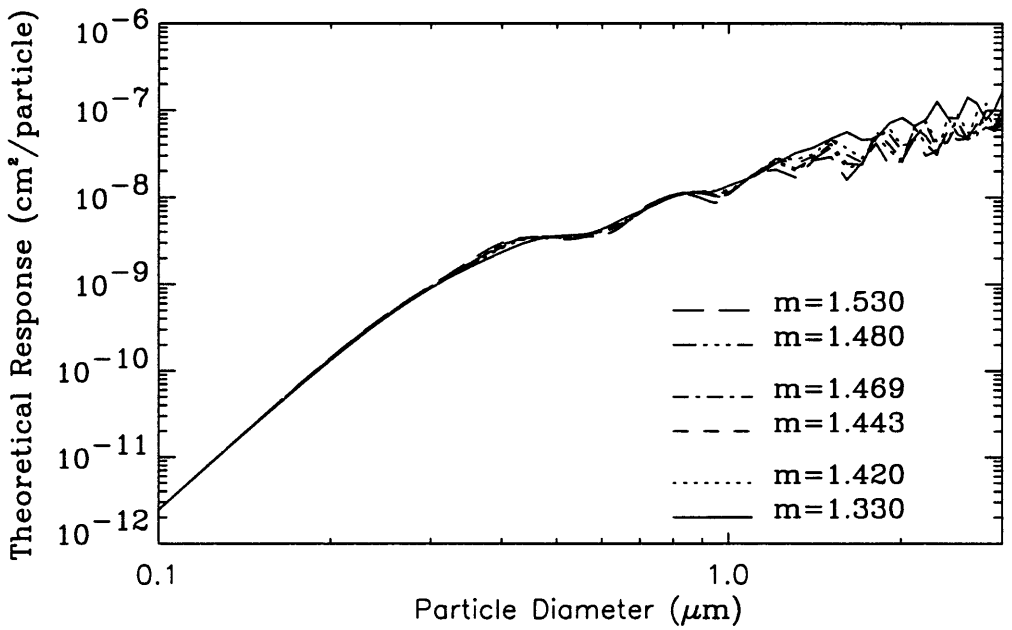

Figure 2.4.1 "Collapsed" Mie curves around m =1.530.

The scaling factor for the theoretical response (f_{TR}) needed to be translated to a diameter scaling factor, f_D. By performing a linear regression in the 0.1 - 0.4 μm diameter range on the original and "collapsed" Mie curves for a given refractive index, two linear equations of the form $TR = aD_p + b$ were determined, where a was the slope, and b was the intercept. These two equations were used to determine a diameter scaling factor in the following way.

Two values of scattering response were chosen (1×10^{-10} and 1×10^{-9} cm^2/particle). These were substituted into both the original and "collapsed" linear equations, from which the values of D_p were determined. A ratio of the original and scaled diameters resulted in a diameter scaling factor, f_D, analogous to the theoretical response scaling factor, f_{TR}. A fit of f_D versus real refractive index (Figure 2.4.2) resulted in a polynomial, equation (2.4.2), with a correlation coefficient of $R^2 = 0.9999$,

$$f_D = 1.759m^2 - 5.9873m + 6.0436 \qquad (2.4.2)$$

where m is refractive index. By using this equation, an original set of diameters (m=1.530) were scaled to a new refractive index by calculating f_D, and multiplying all diameters in the original set by f_D.

Although this scaling was determined from a specific set of seven refractive indices, it was also successfully applied for other refractive indices not used in the development of the equation (see Figure 2.4.3). The advantages of this scaling included a quick determination of new diameters to expedite data inversion, and scaling of diameters in the region $D_p > 1$ μm where resonances in scattering response make it difficult to determine a unique diameter. The disadvantage was that for a refractive index approaching that of water, the Mie curves flatten and the scaling becomes less appropriate (see Figure 2.4.3). The lowest refractive indices in this study for which this scaling procedure will be applied is $m = 1.38$. In Chapter 3, this scaling method will be applied to data inversion assuming a

rural aerosol model for refractive index as a function of relative humidity. In Chapter 6, it will be applied to derived daily refractive indices.

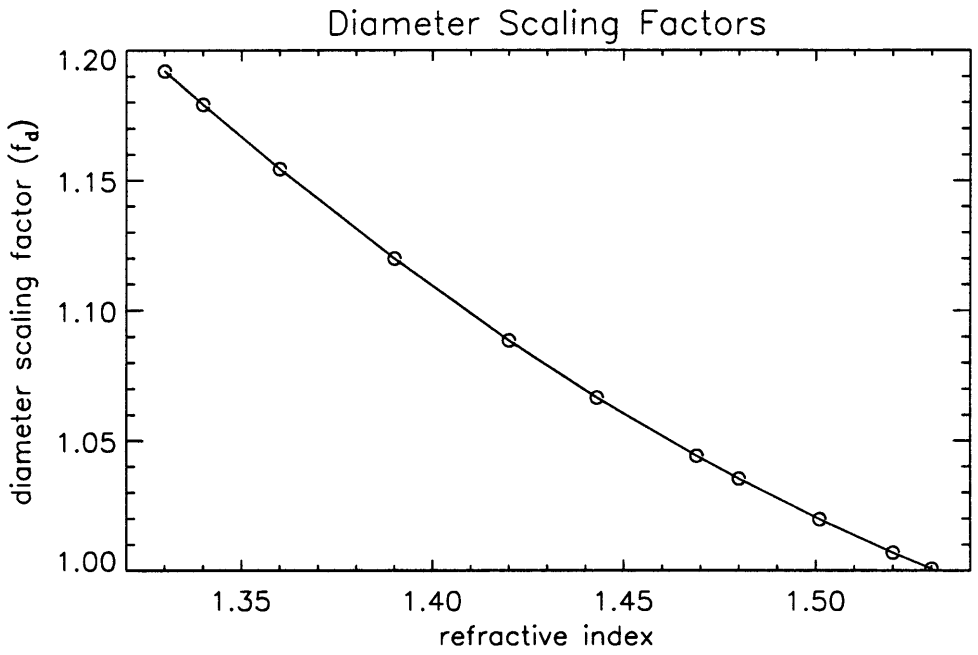

Figure 2.4.2. Diameter scaling factor (f_D) as a function of real refractive index.

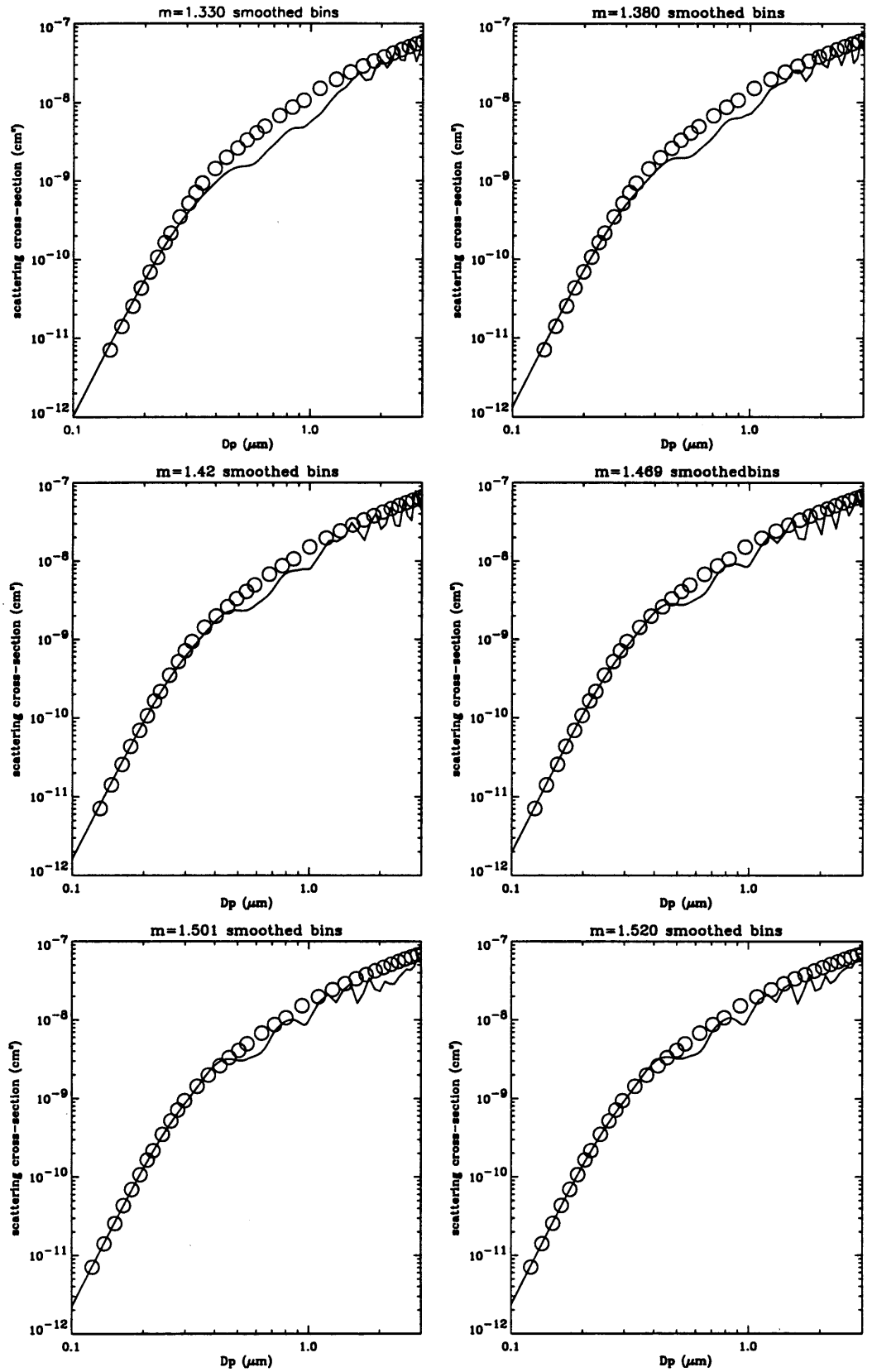

Figure 2.4.3. Scaled diameters for various real refractive indices.

CHAPTER 3. DATA INVERSION AND RESULTS USING A RURAL AEROSOL MODEL REFRACTIVE INDEX

The initial ASASP-X data inversion was performed by employing a rural aerosol model of refractive index based on relative humidity (Shettle and Fenn, 1979). The values of refractive index used in Ames and Kreidenweis (1996) were applied in this section for data inversion and can be found in Table 3.1.1. No absorbing characteristics of the aerosol were considered, therefore the imaginary part of the complex refractive index was ignored.

Table 3.1.1. Rural aerosol model of refractive index

Relative Humidity (%)	Real refractive index, *m*, for rural aerosol model (Shettle and Fenn,1979)	Interpolated values of refractive index, *m*	Relative humidity of applied refractive index (%)
Dry	1.530-0.00660 *i*	1.530	40 > RH
50	1.520-0.00626 *i*	1.520	40 < RH < 60
70	1.501-0.00560 *i*	1.501	60 < RH < 73
75		1.469	73 < RH < 77
80	1.443-0.00370 *i*	1.443	77 < RH < 83
85		1.420	83 < RH

The calibration used for data inversion was described in the previous sections, and diameter size channels as a function of refractive index were determined using the scaling procedure described in Section 2.4. The results presented in this section include dry accumulation mode size distribution parameters, hygroscopicity, and particle light scattering. The present results differ from those in Ames and Kreidenweis (1996) in two respects: the new calibration and refractive index scaling of instrument response, and the fitting of a lognormal size distribution function to the data. In Appendix A, sensitivity studies are presented to demonstrate the effects of these different assumptions on the derived results.

Section 3.1. Lognormal Size Distribution Function.

Atmospheric aerosol size distributions are often conveniently described as a lognormal size distribution function of the form (Seinfeld, 1986):

$$n(\ln D_p) = \frac{N}{(2\pi)^{1/2}\ln\sigma_g} \exp\left[-\frac{(\ln D_p - \ln\overline{D}_{pg,n})^2}{2\ln^2\sigma_g}\right] \qquad (3.1.1)$$

where $\overline{D}_{pg,n}$ is the number median diameter, σ_g is the geometric standard deviation, D_p is the particle diameter, and N is the total number concentration. From these parameters, other size distribution parameters can be derived. Total volume concentration was calculated from equation (3.1.2).

$$V = \frac{\pi}{6} N D_{pvm}^3 \qquad (3.1.2)$$

where D_{pvm} is the volume mean diameter and is given by equation (3.1.3).

$$D_{pvm} = \overline{D}_{pg,n} \exp(1.5 \cdot \ln^2 \sigma_g) \qquad (3.1.3)$$

The volume median diameter, D_{pgv}, was calculated from equation (3.1.4).

$$D_{pgv} = \overline{D}_{pg,n} \exp(3 \cdot \ln^2 \sigma_g) \qquad (3.1.4)$$

To determine ASASP-X size distribution parameters, the DISTFIT lognormal fitting program (Whitby, 1991) was employed. Single mode lognormal functions were fit to the number distribution data in order to represent the accumulation mode (D_p = .1 ~1

μm) of the distribution. The reasons for fitting the lognormal size distribution function to the ASASP-X data were threefold. The first reason is demonstrated by a sample SEAVS ASASP-X aerosol volume distribution in Figure 3.1.1.

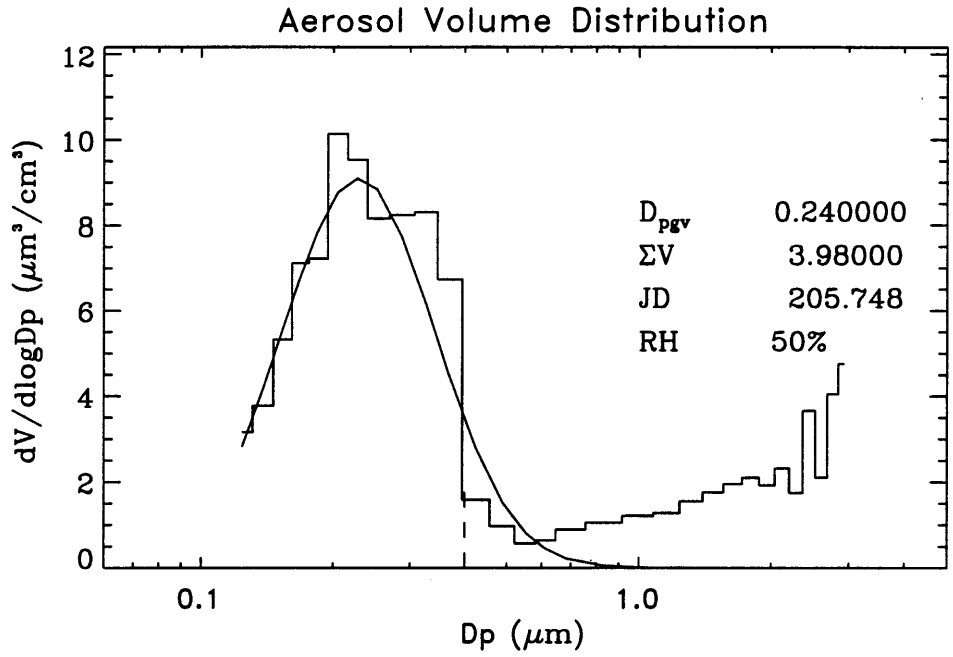

Figure 3.1.1. Sample SEAVS aerosol volume distribution.

An obvious decrease in the distribution around $D_p = 0.4$ μm in Figure 3.1.1 is often noticeable in distributions measured with optical particle counters and is most likely an artifact of the flat region of the Mie response curve in that size range (Hering and McMurry, 1991, Richards, *et al.*, 1985). This large decrease in the size distribution was smoothed by the lognormal curve (see Figure 3.1.1).

The second reason for fitting the data was that the lognormal function was capable of capturing particle sizes smaller than the measuring range of the ASASP-X (D_p < 0.1 μm). By including these sizes, a more realistic approximation of the accumulation mode number distribution was determined (see Figure 3.1.2), and the number median

diameter, $\overline{D}_{pg,n}$, was computed. This parameter was unobtainable using the method in Ames and Kreidenweis (1996) because the smaller size range of the number distribution was not captured. The number distribution parameters were required for light scattering calculations, as discussed in Section 3.3.

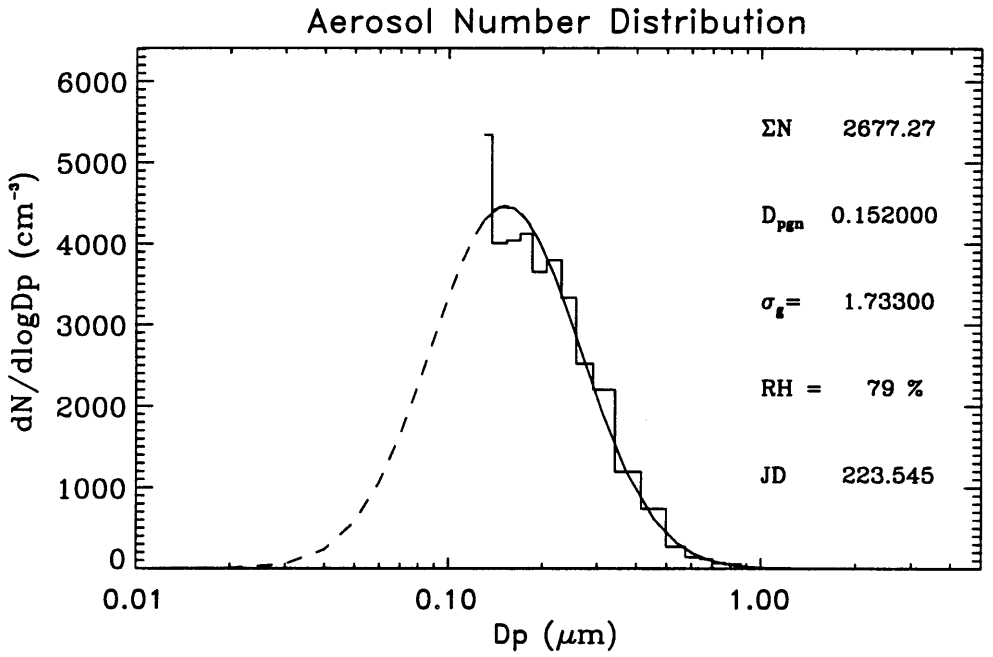

Figure 3.1.2. Sample SEAVS number distribution. The dashed line corresponds to the lognormal curve and demonstrates the extrapolated part of the distribution.

Finally, the fitting automatically determined the accumulation mode for each distribution whereas the accumulation mode cut-off diameter had to be chosen arbitrarily in Ames and Kreidenweis (1996). Comparisons of derived quantities assuming no size distribution function were compared to results obtained using the lognormal fit (see Appendix A), and showed good agreement between the two methods.

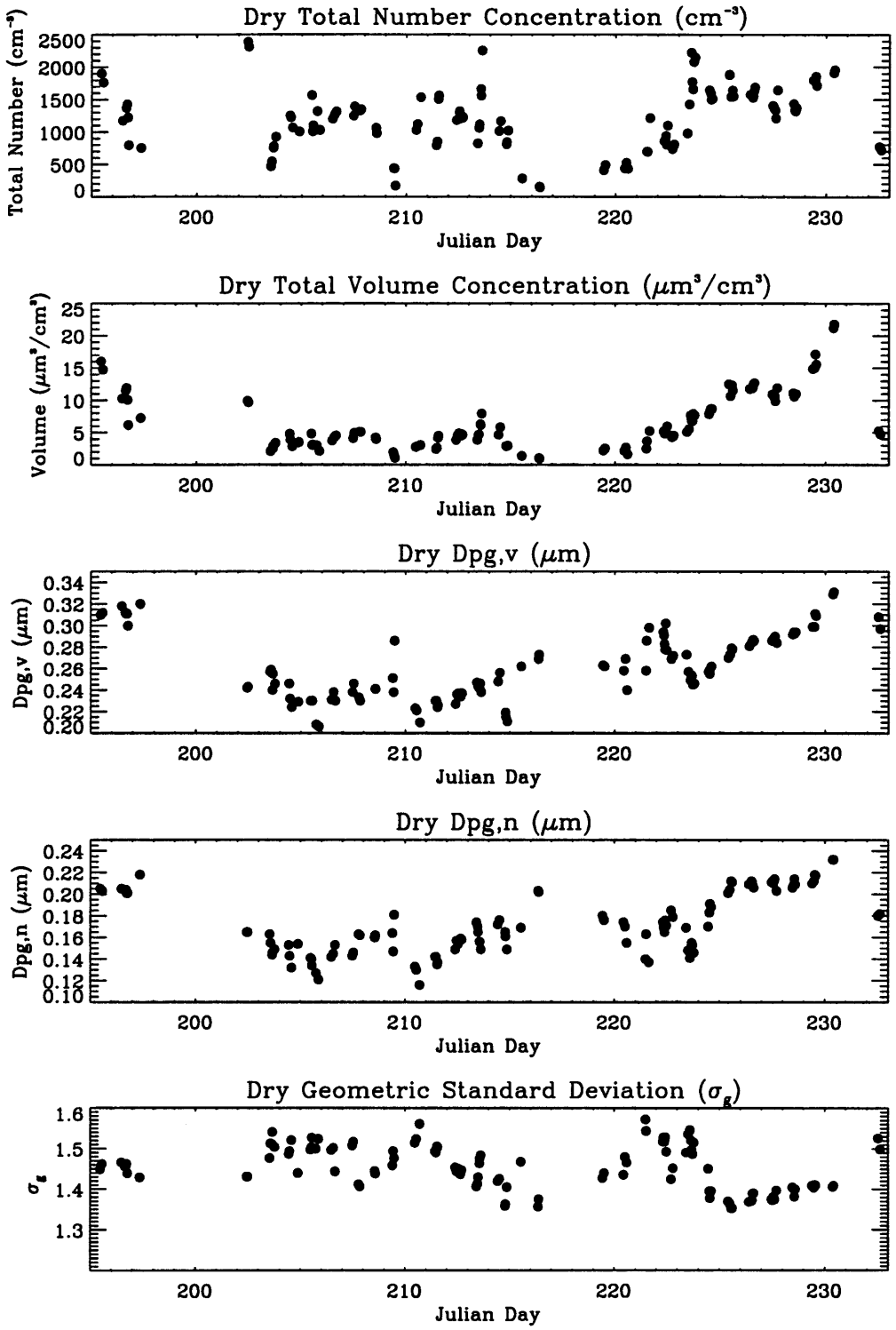

Figure 3.1.3. Dry accumulation mode size parameters using a rural aerosol model.

Timelines of dry accumulation mode size parameters calculated for dry (RH<15%) aerosol are presented in Figure 3.1.3 for JD 195-232. The trends in the size parameters tended to follow the meteorological trends occurring in the site region, as defined in Sherman *et al.* (1997) (see Table 1.1 in Chapter 1). Most noticeably, accumulation mode total number and volume concentrations increased during the extreme haze period at the end of the study. The geometric standard deviation, σ_g, remained very stable during this period. Study averages for dry accumulation mode aerosol lognormal size parameters assuming a real dry refractive index of m =1.530 are reported in Table 3.1.2.

Table 3.1.2. Dry accumulation mode lognormal size parameters for dry real refractive index of m =1.530.

Size Parameter	Study Average	Standard Deviation	Study Maximum	Study Minimum
N (cm^{-3})	1200	± 500	2384	145
V ($\mu m^3 cm^{-3}$)	7	± 4	21.77	0.98
$\overline{D}_{pg,n}$ (μm)	0.17	± 0.03	0.232	0.116
$D_{pg,v}$ (μm)	0.26	± 0.03	0.331	0.206
σ_g	1.45	± 0.06	1.664	1.353

Section 3.2. Particle Hygroscopicity

The major objective of the CSU SEAVS experiment was the determination of aerosol hygroscopicity. A solid aerosol particle will remain in crystalline form until a thermodynamically preferred relative humidity satisfying equation 3.2.1 is reached (termed the relative humidity of deliquescence, RHD)

$$RHD = a_{w,sat} \qquad (3.2.1)$$

where $a_{w,sat}$ is the water activity of the saturated solution (Tang, 1996). Equation (3.2.1) ignores the Kelvin effect, which is generally unimportant for $D_p > 0.1$ μm for thehumidities examined in this study. At the RHD, the particle will spontaneously begin to take up water (deliquesce) and grow. As relative humidity is increased, equilibrium between the aerosol particle and the surrounding water vapor is maintained and the particle continues to grow with the addition of water according to a growth curve corresponding to its particular composition. For the same solution drop which is dried, a hysteresis effect is demonstrated when the particle "descends" on a different branch (efflorescence) than that of the deliquescence curve. The particle will release water and return to crystalline form at a relative humidity lower than the RHD. Figure 3.2.1 shows the hysteresis effect for ammonium sulfate (Nemesure *et al.*, 1995). Different pure salts demonstrate different growth characteristics depending on their corresponding RHD and solution thermodynamics, as demonstrated in Figure 3.2.1 for the ammonium sulfate system.

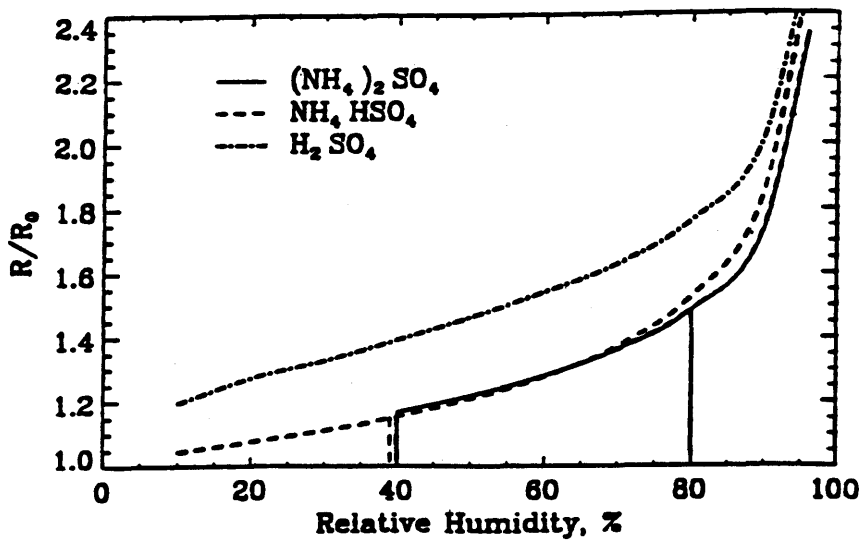

Figure 3.2.1 Hygroscopic growth for the ammonium sulfate system (Nemesure *et al.*, 1995)

Hygroscopicity of the aerosol measured during SEAVS was calculated using ratios of lognormal size parameters. The pairs of wet and dry distributions used to calculate these ratios were the same as those in Ames and Kreidenweis (1996). Two methods were used: ratioing wet to dry volume median diameters ($D_d/D_{d,o}$) and ratioing

wet to dry accumulation mode total volume concentration ($D_V/D_{V,o}$). Equations 3.2.2 and 3.2.3 were used to calculate growth curves from wet-to-dry diameter and volume ratios, respectively:

$$\frac{D_d}{D_{d,o}} = \frac{D_{pgv,wet}}{D_{pgv,\,dry}} \qquad (3.2.2)$$

$$\frac{D_v}{D_{v,o}} = \left[\frac{V_{tot,wet}}{V_{tot,\,dry}}\right]^{1/3} \qquad (3.2.3)$$

Figures 3.2.2(a) and 3.2.2(b) show the resulting growth curves for both methods, with fourth-order polynomial fits to the data. Values of $D_v/D_{v,o}$ demonstrated more scatter than diameter ratios but with larger growth at higher RH. Tang *et al.* (1978) showed that pure sulfate particles had growth factors ranging from 1.5 to 1.8 at 80 % RH, depending on the particle acidity. Svenningsson *et al.* (1992) observed two hygroscopic modes when measuring hygroscopic growth. At 85 % RH, the more-hygroscopic mode mean growth factor was 1.44 ± 0.14 while the less-hygroscopic mode mean growth was 1.1 ± 0.07, with no significant size dependence. Svenningsson *et al.* (1992) concluded that both the hygroscopic modes included insoluble material because the measured growth was much less than that of pure salt. Two hygroscopic modes were previously observed by other investigators (McMurry and Liu, 1978; McMurry and Stolzenburg, 1989; Covert *et al.*, 1991). It was suggested by Svenningsson *et al.* (1992) that the less-hygroscopic mode probably contained soot and organics, while the more-hygroscopic mode most likely consisted of more soluble material such as the major ions, along with some insoluble material. From the fourth-order polynomials plotted in Figures 3.2.2 (a,b), the hygroscopic growth at 85% for the rural aerosol model varied between 1.24 and 1.28 depending on the method of calculation. These results fell between the values obtained by Svenningsson *et al.* (1992), suggesting some insoluble material was present. A noticeable feature of both curves in Figure 3.2.2 (a,b) was their smooth and continuous

shape; no abrupt change in D/D_o occurred for any RH, suggesting the particles were measured on the efflorescence curve, or their composition was something that deliquesced at low RH. More discussion of this feature can be found in Section 4.4.

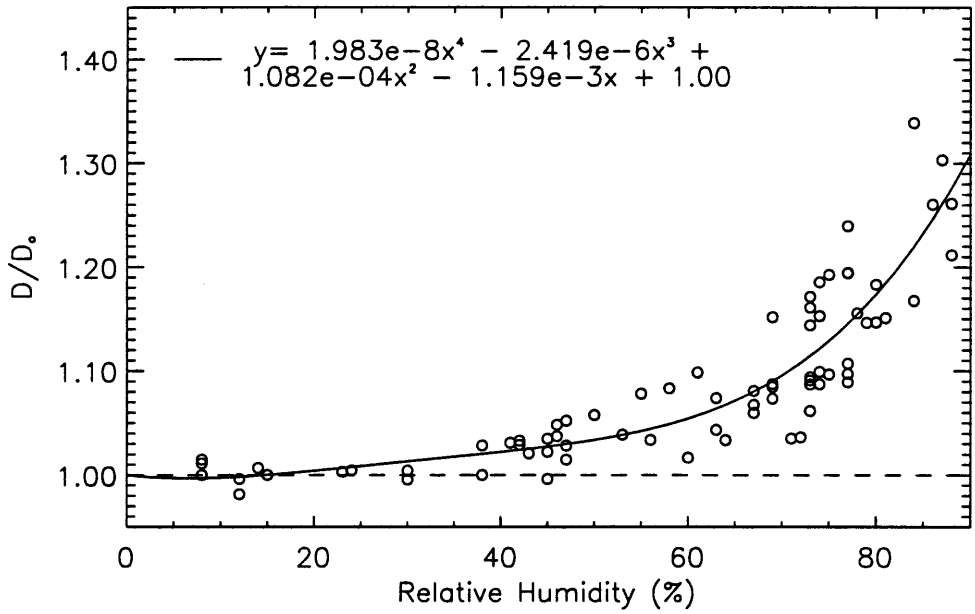

Figure 3.2.2(a) Hygroscopic growth using diameter ratios.

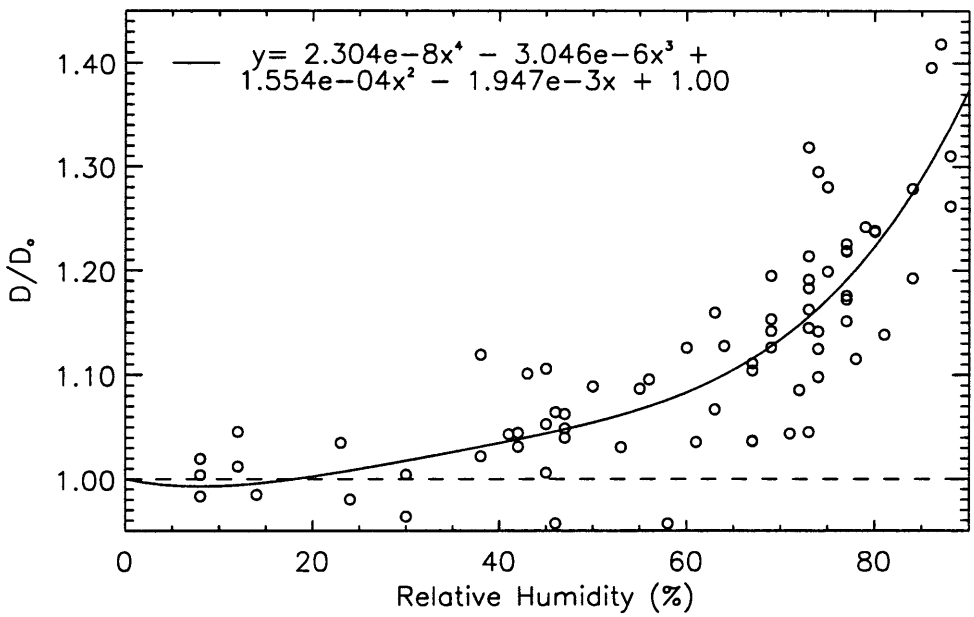

Figure 3.2.2(b) Hygroscopic growth using volume ratios.

Section 3.3. Particle Light Scattering (b_{sp})

Light extinction is contributed to by several components, and the extinction coefficient can be described by equation 3.3.1 (in units of inverse length):

$$b_{ext} = b_{sp} + b_{ap} + b_{sg} + b_{ag} \tag{3.3.1}$$

where b_{sp} and b_{ap} correspond to scattering and absorption by particles, respectively, and b_{sg} and b_{ag} are scattering and absorption by gases. Absorption by particles is due mainly to elemental carbon (soot). Scattering by air molecules is called Rayleigh scattering and the major absorbing gas is nitrogen dioxide. Particle light scattering coefficients can be calculated from equation 3.3.2, where the subscript denoting scattering (*sp*) is replaced by (*ap*), if the absorption coefficient is desired.

$$b_{sp} = \int_0^\infty \frac{\pi}{4} Q_{sp}(x, \lambda, m) D_p^2 \left(\frac{dN}{d\log D_p} \right) d\log D_p \tag{3.3.2}$$

The Mie scattering efficiency, Q_{sp}, is a function of size parameter ($x=\pi D_p/\lambda$), scattered wavelength of light, λ, and particle refractive index, m. The calculation of scattering coefficient, b_{sp}, also depends upon the aerosol number size distribution ($dN/d\log D_p$) and the geometric area of the particles (D_p^2) (Hegg, *et al.*, 1993).

For calculations performed using ASASP-X number distributions, the lognormal size function was convenient to use in a numerical integration of equation 3.3.2. The lognormal number size distribution was divided into 100 size bins, evenly spaced in $\ln D_p$, ranging from 0.01 - 10 μm. The number concentration in each bin was calculated using the difference of a cumulative distribution function, $F(D_p)$, calculated at bin diameters $D_{p,i}$ and $D_{p,i+1}$ (Seinfeld, 1986).

$$F(D_{p,i}) = \frac{N}{2} + \frac{N}{2}\mathrm{erf}\left(\frac{\ln(D_{p,i}/\overline{D}_{pg,n})}{\sqrt{2}\ln\sigma_g}\right) \quad (3.3.3)$$

where N, $\overline{D}_{pg,n}$, and σ_g were defined as lognormal parameters. The particle bin boundary diameter is given by $D_{p,i}$, and *erf* is the error function. The bin number concentration, N_i, determined from equation (3.3.4), was summed over all bins and compared with the total lognormal number concentration, N, to assure consistency.

$$N_i = F(D_{p,i+1}) - F(D_{p,i}) \quad (3.3.4)$$

The midpoint bin diameter, $D_{pm,i}$, of each bin was calculated with equation (3.3.5), and converted into the size parameter with $\lambda = 0.530$ μm, chosen to represent the midpoint of the visible spectrum.

$$D_{pm,i} = \sqrt{D_{p,i} \cdot D_{p,i+1}} \quad (3.3.5)$$

Scattering efficiency, $Q_{sp}(x, m, \lambda)$, was calculated using Mie theory (Bohren and Huffman, 1983), assuming spherical, internally mixed homogeneous particles. For each bin, the scattering efficiency, Q_{sp}, and scattering coefficient were calculated using equation (3.3.6) at the midpoint diameter. The refractive index applied in this calibration corresponded to those in the rural aerosol model. For dry (RH < 15%) distributions, the refractive index was always taken to be $m = 1.530$.

$$b_{sp,i} = \frac{\pi}{4} N_i Q_{sp,i}(x,m,\lambda) D_{pm,i}^2 \quad (3.3.6)$$

The total scattering coefficient, b_{sp} , was then calculated by equation (3.3.7).

$$b_{sp} = \sum_i b_{sp,i} \qquad (3.3.7)$$

Figure 3.3.1 shows timelines of b_{sp} (km^{-1}) for dry (RH<15%, m=1.530) accumulation mode aerosol with a study average of 0.044 km^{-1}. Nephelometer measurements at SEAVS showed good agreement, except for the last two days when the nephelometer was unreliable (Day *et al.*, 1996). The scattering coefficients calculated from a semi-empirical fit based on work by Malm *et al.* (1994a), given by equation (3.3.8), are also plotted.

$$b_{sp} \approx eff_{drum}[sulfate]f(RH) + 0.003[Inorg]f(RH) + 0.004[OC] + 0.001[soil] \qquad (3.3.8)$$

(Equation (3.3.8) from Derek Day, personal communication). The closed brackets in equation (3.3.8) denotes species concentration in μg m^{-3}. The coefficients thus represent species mass scattering efficiencies . The term eff_{drum} is the mass scattering efficiency of sulfate computed from daily DRUM sampler measurements made during SEAVS. The growth term, ($f(RH)$), which appears in the first and second terms, represents the change in mass scattering efficiency with relative humidity for hygroscopic particles (Malm *et al.*, 1994b). The dry scattering efficiency for organic carbon was taken as 0.004 km^{-1}μg m^{-3} and for soil as 0.001 km^{-1}μg m^{-3} . The soil constituents for this calculation were assumed to be silicon, aluminum, and iron. Inorganic aerosol, [inorg], included $NO3^-$, Na^+, and Cl^-, and a dry scattering efficiency of 0.003 km^{-1}μg m^{-3} was assumed for these.

The trends were consistent with meteorological periods, e.g., b_{sp} increased during the hazy event, when decreased visibility was expected. Although trends agreed for the two methods of computing b_{sp} , ASASP-X data were significantly lower than those using

the semi-empirical relationship, as shown in Figure 3.3.1. From equation (3.3.2), the components which affect the calculations of b_{sp} were the scattering efficiency, Q_{sp}, the particle area, D_p^2, and the number distribution. If the refractive index used in the calculation was smaller, the scattering would decrease, but the inverted size distributions would lead to larger size parameters. Tang (1996) and Hegg *et al.* (1993) found that in calculations of light scattering coefficients, the chemical effect (species composition) is outweighed by the size effect. In Chapter 6, the effects of lower refractive index and larger particle area will be investigated.

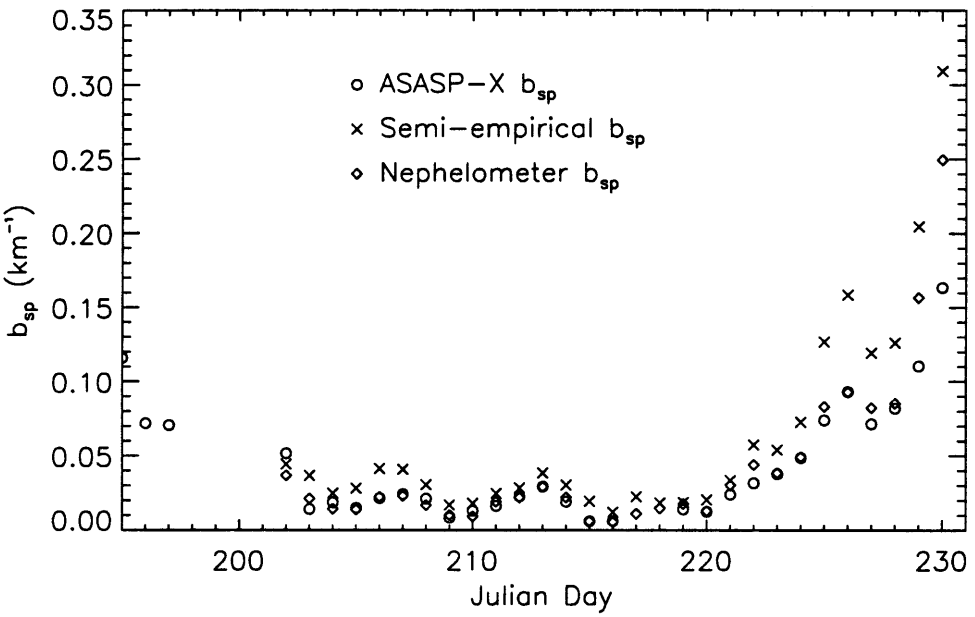

Figure 3.3.1 Timeline of dry b_{sp} (km^{-1}) for rural aerosol model (RH < 15%, m = 1.530) plotted with nephelometer measurements and semi-empirical estimates.

Section 3.4. Particle Light Scattering Growth Curve (b/b_o)

As mentioned in the previous section, the effects of relative humidity on scattering efficiencies for hygroscopic particles will modify the particle light scattering coefficient, b_{sp}. As particles take up water, light scattering characteristics change through decreased refractive index, and increased size (area). Ames and Kreidenweis (1996) demonstrated the effects of increased relative humidity on scattering coefficients

for a lognormal distribution of ammonium sulfate with equivalent dry mass of 1 μg m^{-3} and σ_g of 1.6. The most efficient scattering for this case occurred at relative humidities greater than 80%, and for dry diameters near 0.3 μm.

The differences between wet and dry scattering coefficients can be expressed as the ratio of these coefficients, analogous to expressing the hygroscopicity as the ratio of wet and dry particle diameters. This ratio will be called the scattering growth curve, b/b_o. The refractive indices for higher relative humidities were approximated by the rural aerosol model and the distributions used in the calculation of b/b_o were those used in the D/D_o calculations (Section 3.2). Results of b/b_o are shown in Figure 3.4.1, along with the fourth-order polynomial fit to the data. At 85 % RH, a growth of ~1.9 was observed. Relative humidity controlled nephelometer measurements at SEAVS resulted in a growth of ~2.1 at 85 % RH (Day *et al.*, 1996). In Appendix B, these values will be compared with those using measured chemical composition to estimate wet and dry refractive indices.

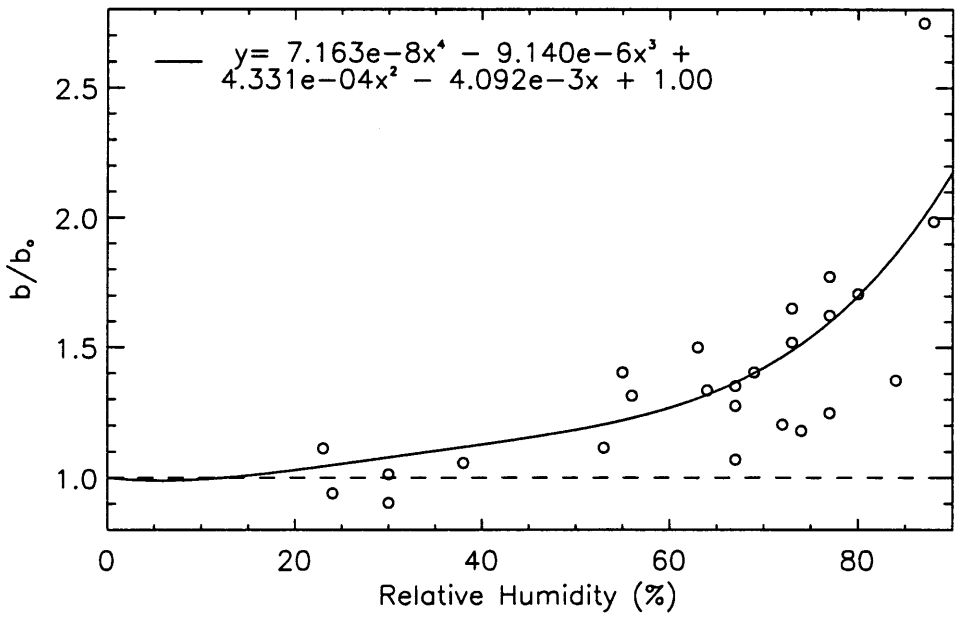

Figure 3.4.1. Rural aerosol model scattering growth curve, b/b_o.

CHAPTER 4: DRY REFRACTIVE INDEX AND CHEMICAL COMPOSITION

In this study, the aerosol refractive index was needed for the inversion of size distribution data, and for the calculation of derived quantities, such as the aerosol scattering coefficient. Previous hygroscopicity and light scattering results presented in Sections 3.2 and 3.3 were obtained by assuming a model for refractive index as a function of relative humidity (Shettle and Fenn, 1979). Chemical measurements made during SEAVS demonstrated the daily variations in the chemical composition. Because aerosol refractive index depends on its chemical composition, the daily variations in dry refractive index needed to be applied to the ASASP-X data inversion.

Refractive index can be calculated by two different methods with known aerosol chemical composition. For this study, the chemical compositions measured by the IMPROVE network were used. Before considering the different species measured and included in the refractive index calculations, the methods for calculating refractive index will be presented.

Section 4.1. Partial Molar Refraction Method (PMR).

The partial molar refractive index method (PMR), as outlined in Stelson (1990), is as follows. The mean real refractive index, $\overline{m}$, can be calculated from:

$$\overline{m} = \left(\frac{1 + 2R/V}{1 - R/V} \right)^{1/2} \tag{4.1.1}$$

where

$$\frac{R}{V} = \frac{\sum_i (R_i/M_i)[S_i]}{[AV]} \tag{4.1.2}$$

and M_i is the molecular weight of species i (g mol^{-1}), R_i is the partial molar refraction of species i (cm^3 mol^{-1}), V_i is the molar volume (cm^3 mol^{-1}), $[S_i]$ is the concentration of species i (μg m^{-3}), and $[AV]$ is the aerosol volume in μm^3 cm^{-3}. If volume conservation on mixing is assumed, the aerosol volume can be written as the following:

$$[\mathrm{AV}] \approx \sum_i \frac{[\mathrm{S_i}]}{\rho_i} \tag{4.1.3}$$

The right hand side of equation (4.1.3) can be written as:

$$\sum_i \frac{[\mathrm{S_i}]}{\rho_i} = \frac{\sum_i [\mathrm{S_i}]}{\bar{\rho}} \tag{4.1.4}$$

where ρ_i is the density of species i (g cm^{-3}), and $\bar{\rho}$ is the mean aerosol density, computed from equation (4.1.5), assuming volume conservation (Hasan and Dzubay, 1983). For each species, $(R/M)_i$, ρ_i, and refractive index (m_i) must be internally consistent.

$$\bar{\rho} = \left[\mathrm{X_i} / \rho_i \right]^{-1} \tag{4.1.5}$$

In equation (4.1.5), X_i is the mass fraction of species i. Using equations (4.1.3) and (4.1.4), equation (4.1.2), can be written as equation (4.1.6).

$$\frac{\mathrm{R}}{\mathrm{V}} = \bar{\rho} \sum_i \frac{\mathrm{R_i}}{\mathrm{M_i}} \cdot \mathrm{X_i} \tag{4.1.6}$$

The aerosol mean real refractive index is then calculated from equations (4.1.6) and (4.1.1). In order to use the partial molar refractive index method, values of $(R/M)_i$, ρ_i,

and mass concentration must be known or assumed for each species. Choices of chemical species and parameters used in the calculations for this thesis will be discussed in Section 4.4.

Section 4.2. Volume Weighted Eefractive Index Method (VWR).

The second method for calculating refractive index is the volume weighting method (VWR) (Hasan and Dzubay, 1983; Ouimette and Flagan, 1982; Shettle and Fenn, 1979). For this method, the component index of refraction, m_i, the component density, ρ_i, and the mass fraction, X_i, must be known or assumed in order to calculate mean aerosol refractive index, $\overline{m}$:

$$\overline{m} = \bar{\rho} \sum_i \frac{m_i X_i}{\rho_i} \qquad (4.2.1)$$

Mean aerosol density was calculated by equation (4.1.5). In this thesis, both methods were used to calculate refractive index, however, only the partial molar refractive index method results were employed in the data inversion and analysis as the two methods yielded virtually identical results.

Section 4.3. Chemistry

The species chemical concentrations used in the refractive index calculations were from the SEAVS IMPROVE samples and analyses. The following chemical components were initially explored: $SO_4^=$, NH_4^+, NO_3^-, organic carbon (OC), and soil constituents (metals). Elemental carbon (EC) will be considered in Section 4.5. The metals included in the calculation of soil mass were silicon, aluminum, iron, calcium, and magnesium. These

metals were assumed to be in the following oxide forms: SiO_2, Al_2O_3, Fe_2O_3, CaO, and MgO. Total soil mass was calculated by equation (4.3.1)

$$[SOIL] = 2.14[Si] + 1.89[Al] + 1.43[Fe] + 1.4[Ca] + 1.66[Mg] \quad (4.3.1)$$

where the multiplicative constants take into account oxygen mass. Organic carbon mass was assumed to be 1.4 times the measured mass, where the 1.4 factor takes into account hydrogen, carbon and oxygen mass due to the unknown form of the organic carbon (Derek Day, personal communication). Nitrate was assumed to be in the form of potassium nitrate; reasons for this are discussed in Section 4.3.2.

The mass concentration timelines in Figure 4.3.1 show peaks for most of the measured chemical constituents during the hazy periods of the study (JD 195-200 and 225-230). On average, ammonium, sulfate and organic carbon were the major contributors to aerosol mass.

The timeline of molar ratio of ammonium to sulfate can be found in Figure 4.3.2. The degree of neutralization of sulfate varied during SEAVS, with a study average of 1.1 ± 0.3, suggesting an average composition close to that of ammonium bisulfate. Nitrite concentrations were small in comparison, and nitrate mass concentrations trends did not necessarily follow those of sulfate and ammonium (see Figure 4.3.3). Soil peaks occurred during the dust storm (JD 205-208) and again around the hazy period (JD 225-230). Of the various soil species, silicon had the highest overall concentration, with aluminum next and iron third (see Figure 4.3.4).

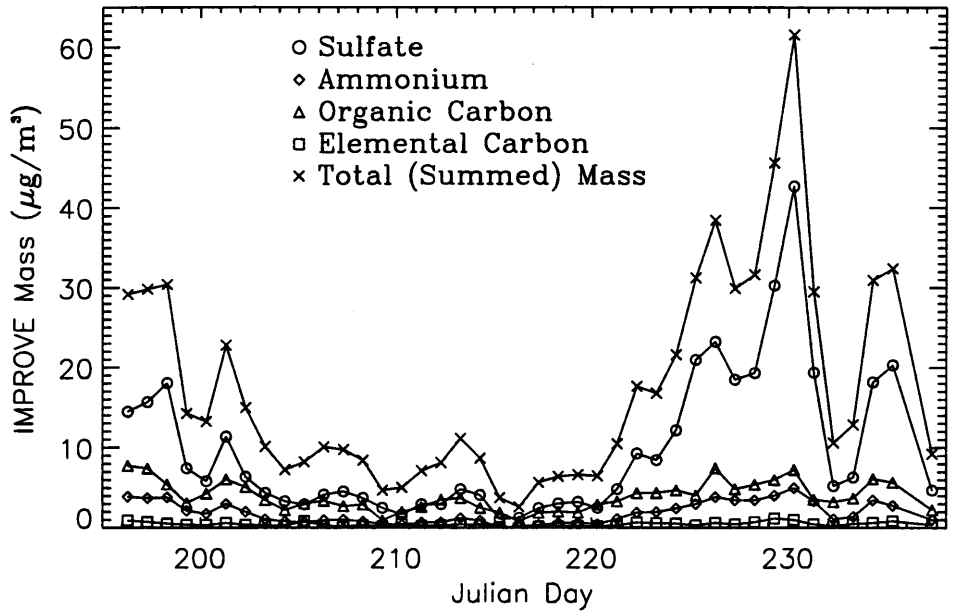

Figure 4.3.1. IMPROVE mass concentration (μg m^{-3}) during SEAVS. Total mass is the sum of all the masses shown.

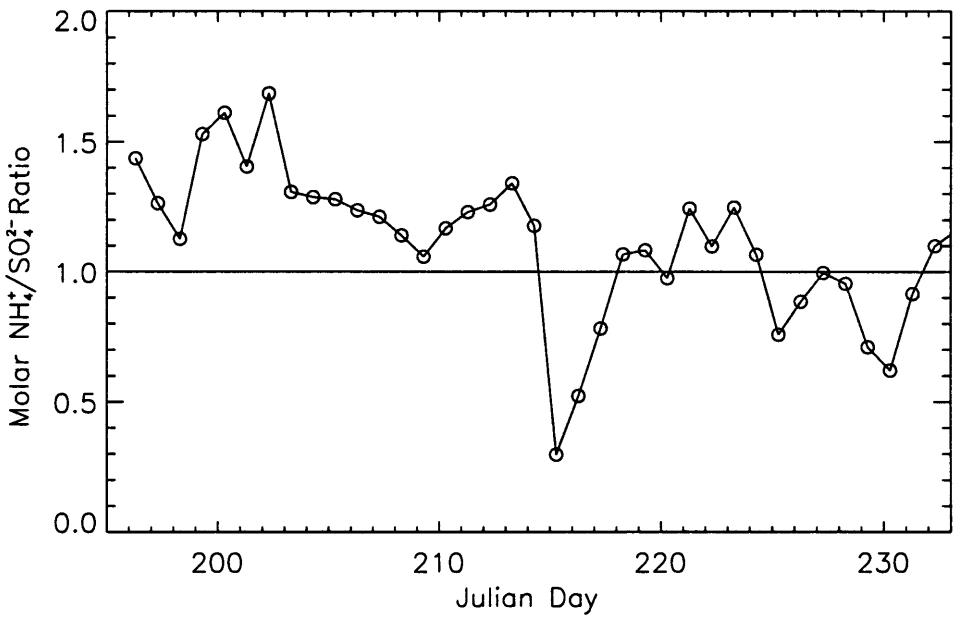

Figure 4.3.2. SEAVS IMPROVE ammonium to sulfate molar ratio.

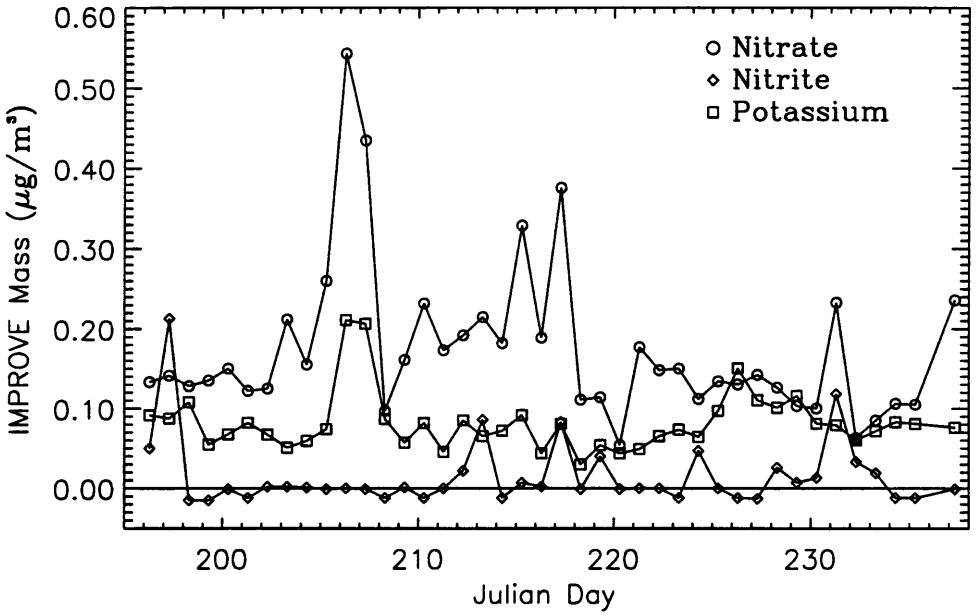

Figure 4.3.3 SEAVS IMPROVE mass concentrations of potassium, nitrate, and nitrite.

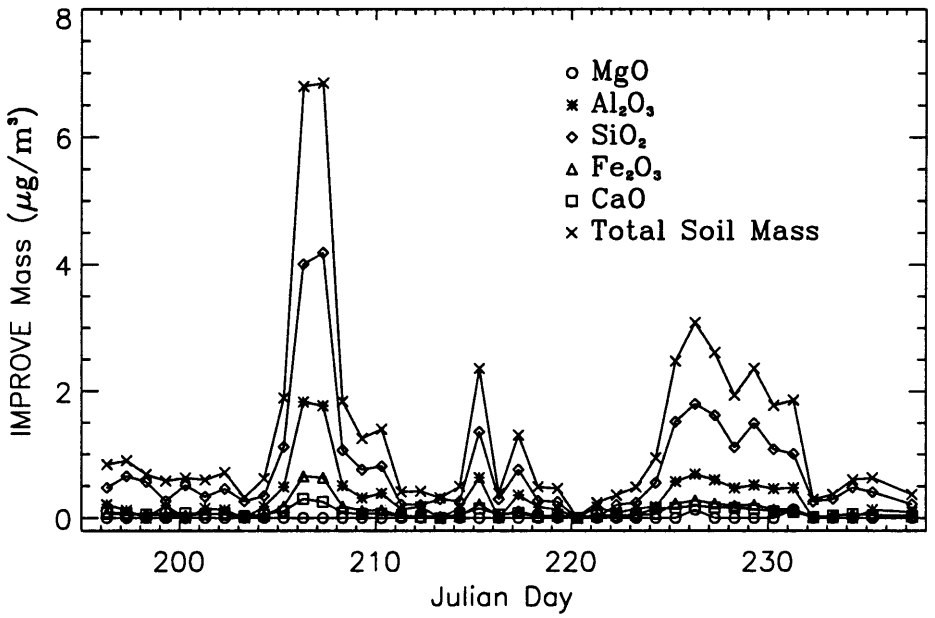

Figure 4.3.4. SEAVS IMPROVE soil mass concentrations during SEAVS. Total soil mass is the sum of all soil components.

Section 4.3.1. Choices of Chemical Composition for Refractive Index Calculations

For the initial choices of chemical compounds to include in the calculation of dry real refractive index, those species with known values of molar refractive index, R, and density, ρ, were chosen. These initial choices were the following: ammoniated sulfate compound (ranging in degree of neutralization from $(NH_4)_2SO_4$ to H_2SO_4), organic carbon, potassium nitrate, and soil. At this stage, elemental carbon was not included due to its absorbing characteristics. Nitrate was assumed to be in the form of potassium nitrate because, as seen in Figure 4.3.2, sulfate was not fully neutralized, therefore, NH_4NO_3 was not expected to exist in significant amounts. IMPROVE mass measurements demonstrated that potassium was present for the duration of the study (Figure 4.3.3), and potassium nitrate molar refraction and density values were available.

To determine the ammonium sulfate compound mass, the degree of neutrality of sulfate and the associated unknown hydrogen mass was considered. Equation 4.3.1 was derived to calculate hydrogen mass (H^+_{mass})based on the ammonium to sulfate molar ratio, m_r.

$$H^+_{mass} = (m_{SO_4^=})[1-\frac{m_r}{2}](2\frac{M_H}{M_{SO_4^=}}) \qquad (4.3.1)$$

where M_H is the molecular weight of hydrogen, M_{SO4} is the molecular weight of sulfate, and the mass concentration of sulfate is m_{SO4} ($\mu g\ m^{-3}$). The resulting ammoniated sulfate compound mass was the sum of $SO_4^=$, NH_4^+, and H^+ masses.

Ammoniated sulfate compound density was also determined based on ammonium to sulfate molar ratio. Density was known for certain degrees of neutralization, but for compounds with molar ratios in between the known values, a linear interpolation was performed to obtain density. Table 4.3.1 provides values used in the interpolation

method. A similar procedure was performed to determine ammoniated sulfate compound refractive index, which was required with VWR. For the calculation of refractive index using PMR, ammonium and sulfate were treated as ions, for which values of *R/M* were found in Stelson (1990). Values of *R/M* were not available for ammoniated sulfate compounds with the full range of degrees of neutrality seen during SEAVS. Sulfate and ammonium were treated as one compound when calculating total density. Table 4.3.1 provides values which were included in refractive index calculations. The species refractive indices reported for the ammoniated sulfate compounds (rows 1 through 4) were derived with the partial molar method by assuming sulfate and ammonium were in ion form.

Table 4.3.1 Physical constants of species used in refractive index calculations.

Species	density g cm^{-3}	R/M	refractive index	source
H_2SO_4	1.8	NA	1.40823	S*
NH_4HSO_4	1.78	NA	1.47897	S*
$(NH_4)_3H(SO_4)_2$	1.83	NA	1.52739	S*
$(NH_4)_2SO_4$	1.76	NA	1.53092	T
OC	1.4	0.2275	1.55	S*
EC	2.0	0.259-0.104*i*	1.96 - 0.66*i*	Snf,S,OF
KNO_3	2.109	0.1304	1.462	S*
H_2O	0.99707	0.2061	1.333264	CRC, S
$SO_4^=$	NA	0.140	NA	S
NH_4^+	NA	0.271	NA	S
SiO_2	2.32	0.1237	1.486	CRC, S,S*
Al_2O_3	3.97	0.1042	1.765	CRC, S,S*
Fe_2O_3	5.24	0.1391	3.011	CRC, S,S*
CaO	3.3	0.1334	1.833	CRC,S,S*
MgO	3.58	0.1121	1.735	CRC,S,S*

S refers to values directly from Stelson (1990)
*S** refers to values derived from those in Stelson (1990)
T refers to values directly from Tang (1996)
CRC refers to the Handbook of Chemistry and Physics, 61st Edition (1980-1981)
Snf refers to Seinfeld (1986)
OF refers to Ouimette and Flagan (1982)

Preliminary dry refractive indices from the partial molar method are presented in Figures 4.3.5 and Figures 4.3.6. Refractive indices for the mixture of soil components only are shown in Figure 4.3.5. For most of the SEAVS study, the soil refractive index fluctuated around m=1.6. However, on JD 220, a much larger refractive index was computed. On this particular day, the only major contributing compound to soil mass was iron, which has a refractive index of approximately 3 (see table 4.3.1). Figure 4.3.6 shows daily dry refractive indices with the following components added to soil: $SO_4^=$, NH_4^+, OC, and KNO_3. Figure 4.3.6 represents refractive indices calculated from those components without soil. The inclusion of soil acted to raise the refractive index values, especially during episodes when the soil mass concentration peaked, such as during the dust event (JD 205-208). The inclusion of KNO_3 generally had minimal effect on the refractive index.

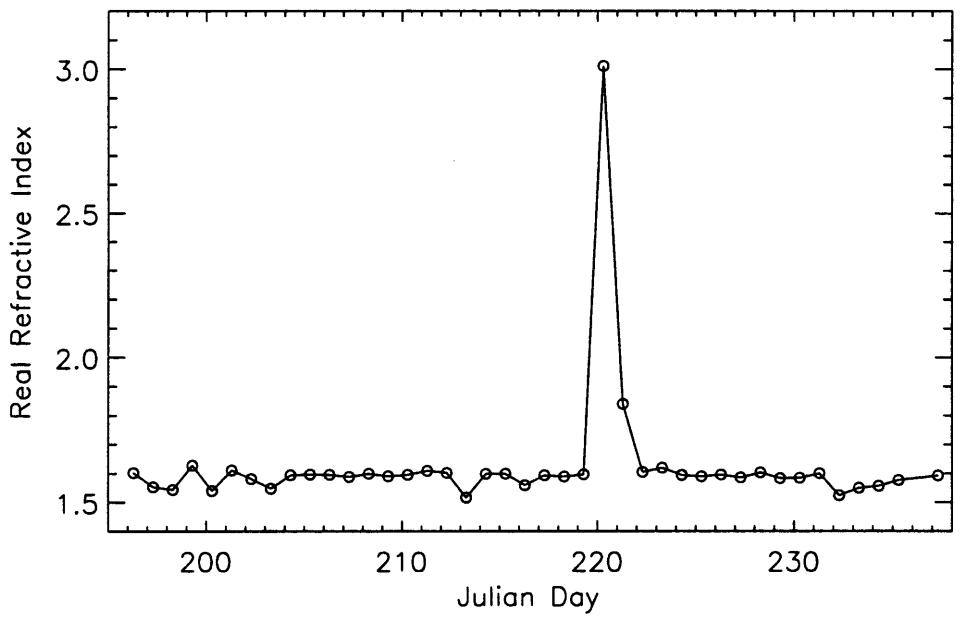

Figure 4.3.5 Daily dry refractive index of soil only, using the PMR method.

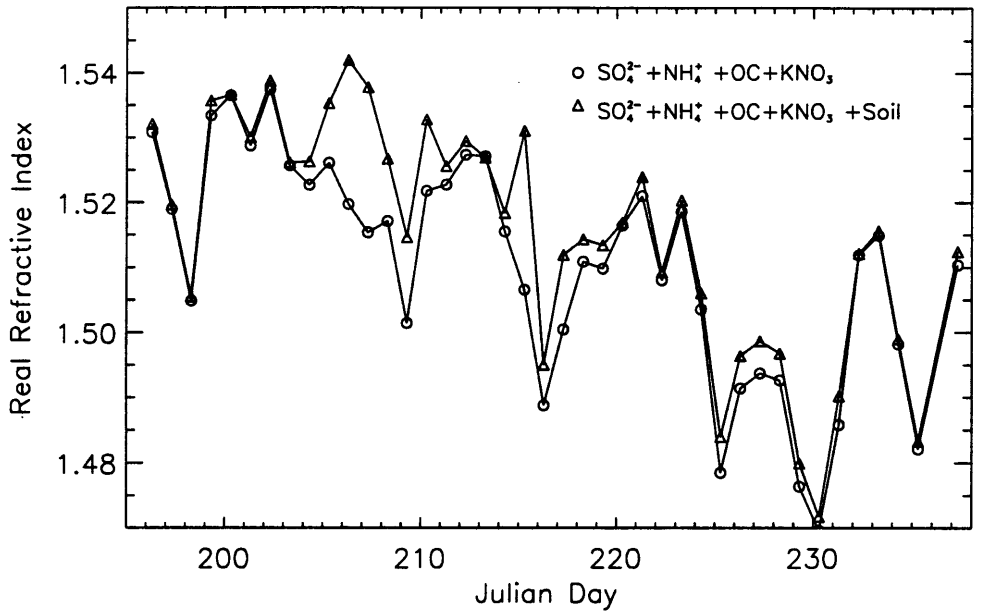

Figure 4.3.6. Daily dry refractive index including other components, computed with and without soil using the PMR method.

Section 4.4. Final Choices for Refractive Index.

In choosing the final chemical species included in the refractive index calculations, two changes to initial choices were considered: subtracting soil and adding water.

Soil

As was seen in the previous section, the inclusion of soil acted to increase refractive index. The uncertainty in whether to include soil in the refractive index calculation originated from the soil particle size. The size parameters derived from ASASP-X data only consider the accumulation mode, D_p <1 μm. Figure 4.4.1 demonstrates a second volume mode which occurred during the dust episode (JD 206~208). The size distributions suggest that soil or dust contributes primarily to the larger (> 1 μm) particle fraction, nonetheless, it is probable that some of the accumulation mode consisted of soil mass because soil components have been observed for sizes less

than 2.5 μm (Perry *et al.*, 1996). Since the fraction of the accumulation mode volume attributed to soil was unknown, and it was deemed inappropriate to include all of the measured soil mass in the accumulation mode refractive index calculations, the limiting case of no soil in the accumulation mode fraction was assumed.

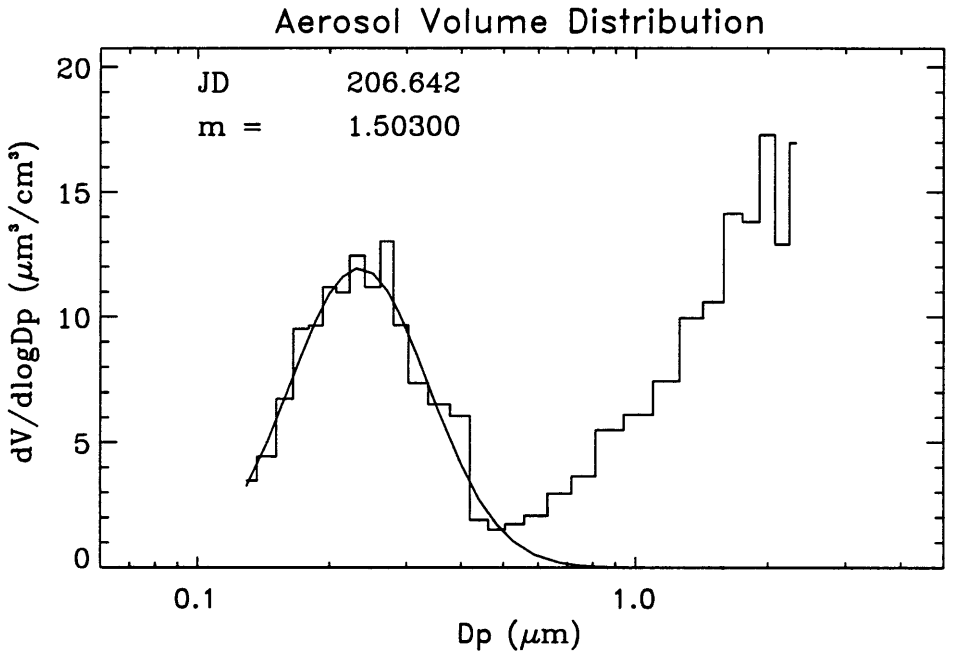

Figure 4.4.1. SEAVS aerosol volume distribution measured during the dust episode. The second mode contributes significant volume concentration.

Water

The ambient relative humidity (RH) at the SEAVS site varied from 65 % to 98 % during the study. The aerosol sampled with the relative humidity controlled inlet might typically have been dried rather than humidified to a specific relative humidity value. It could be concluded that the aerosol were usually measured on the efflorescence curve, possibly explaining the smooth growth curves presented in Chapter 3. During SEAVS, aerosol sampled at RH < 15 % were assumed to be dry. Tang and Munkelwitz (1994) demonstrated that NH_4HSO_4 exists as a solution of 90 % by mass salt, 10 % by mass water in equilibrium with 15 % RH. On the efflorescence branch, NH_4HSO_4 does not

crystallize until RH ~ 2.5 % (Nemesure *et al.*, 1995), a relative humidity lower than that typically used for "dry" measurements at SEAVS. The study average ammoniated sulfate species was close to that of NH_4HSO_4, therefore it was assumed that the "dry" aerosol was not in crystalline form. Bound water mass was assumed to be 10 % of the ammonium and sulfate solution concentration, consistent with the results of Tang and Munkelwitz (1994). This water mass was combined with the other species for dry refractive index calculations.

The final species included in the refractive index calculations remained the same as in the initial calculations: organic carbon, potassium nitrate, and ammoniated sulfate compound, but with the addition of water (and subtraction of soil). Dry refractive indices used for calculations in the remainder of this thesis were derived from these assumptions. Figure 4.4.2. provides timelines of dry refractive indices calculated with the partial molar and volume weighted method. The two methods show good agreement. In the remainder of this thesis, dry refractive indices from the PMR method will be applied.

Section 4.5. Complex Refractive Indices

For the previous calculations, it was assumed that the aerosol constituents had no absorbing components, and thus the computed refractive indices had only real parts. The effect of elemental carbon on refractive index will now be considered. Using dry aerosol total mass and real refractive index calculated in the previous section, a complex refractive index was calculated using the volume weighting method (equation 4.5.1),

$$\overline{m} = \bar{\rho} \sum_i \frac{X_i m_i}{\rho_i} \qquad (4.5.1)$$

where $m_i = n_i + ik_i$. Equation (4.5.1) can then be written as:

$$\overline{m} = \bar{\rho}\sum_i \frac{X_i\, n_i}{\rho_i} + \bar{\rho}\sum_i \frac{X_i\, k_i}{\rho_i} i \qquad (4.5.2)$$

In this case only two terms were included in the summation; $i = 1$ was for the non-absorbing dry species and $i = 2$ was for elemental carbon, assuming $m_{ec} = 1.96 - 0.66i$ and $\rho_{ec} = 2$ g cm^{-3} (Ouimette and Flagan, 1982; Seinfeld, 1986). The daily varying complex refractive indices are shown in Figure 4.5.1, plotted with the real daily varying refractive index for comparison.

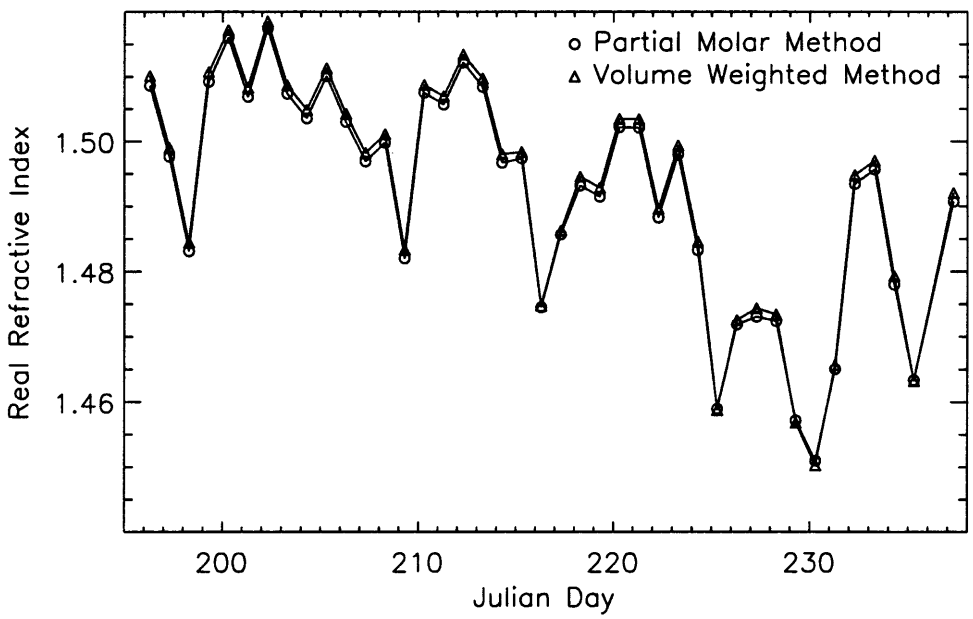

Figure 4.4.2. Daily varying dry refractive indices for SEAVS using SO_4^{-2}, NH_4^+, H^+, OC, KNO_3, and bound H_20.

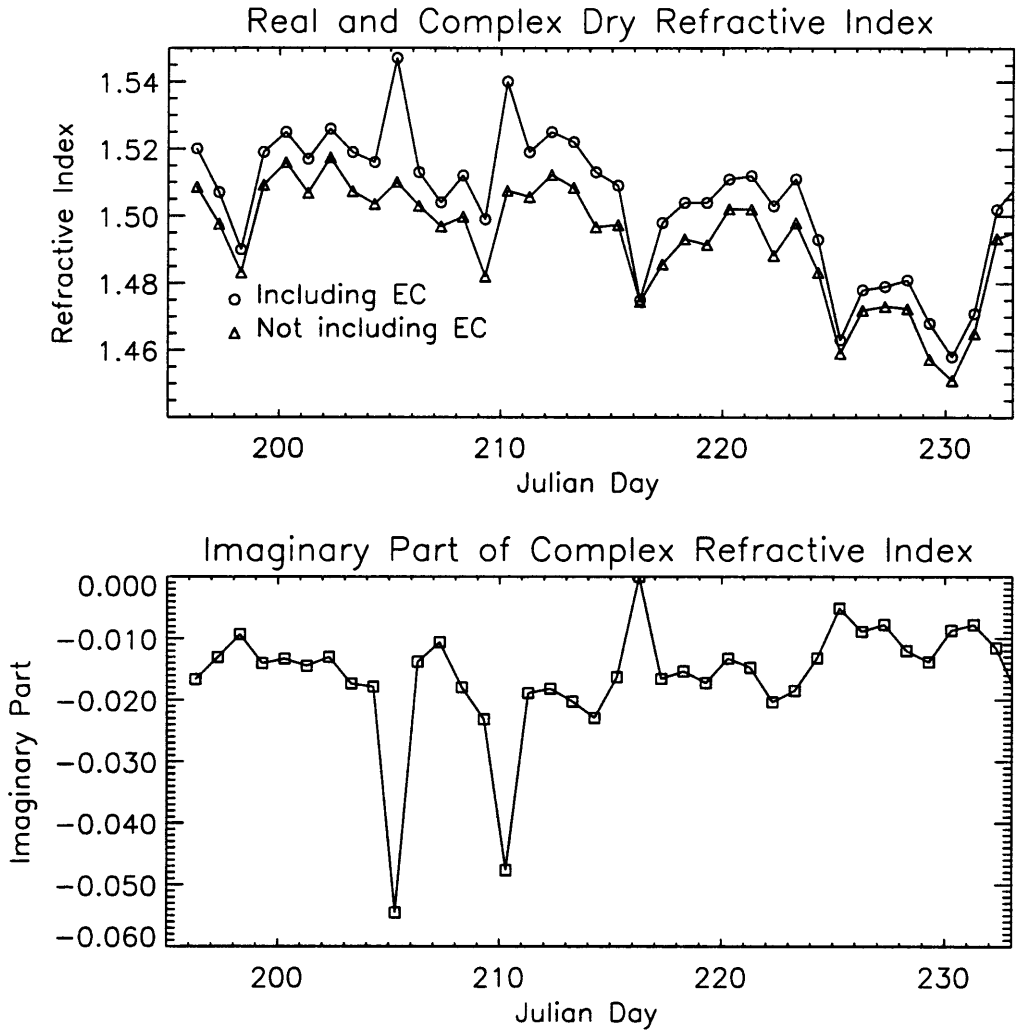

Figure 4.5.1. Complex refractive index calculated by including elemental carbon. Real refractive indices are also plotted for comparison.

Although on average elemental carbon was only 3 % of the total mass, it acted to increase the real refractive index. The imaginary part of the complex refractive index increased on days when the elemental carbon mass increased, and was zero when elemental carbon mass was zero. Ouimette and Flagan (1982) reported that soot would have a large effect on the volume weighting calculation due to the imaginary part of its refractive index. This effect was noticeable on days with a larger elemental carbon mass fraction (9% and 10%).

The effects of elemental carbon on the ASASP-X response were investigated by using Mie scattering. In Figure 4.5.2, instrument response functions for a range of values for the imaginary part (k) of the complex refractive index for $\Re e(m) = 1.52$ are plotted to demonstrate the effects of aerosol absorption. The value of k had no effect on scattering response for small particles ($D_p < 0.2$ μm). For increasing k, the scattering decreases for $D_p > 0.4$ μm. In the larger particle size range, for certain diameters, a complex refractive index could have a scattering response similar to a non-absorbing particle with a smaller real refractive index (notice the $\Re e(m) = 1.40$ response curve in Figure 4.5.2). The effects of the complex refractive index on ASASP-X data inversion and derived quantities could be significant for larger particle sizes. Calculations of particle light extinction coefficients using the complex refractive indices derived in this section will be presented in Chapter 6.

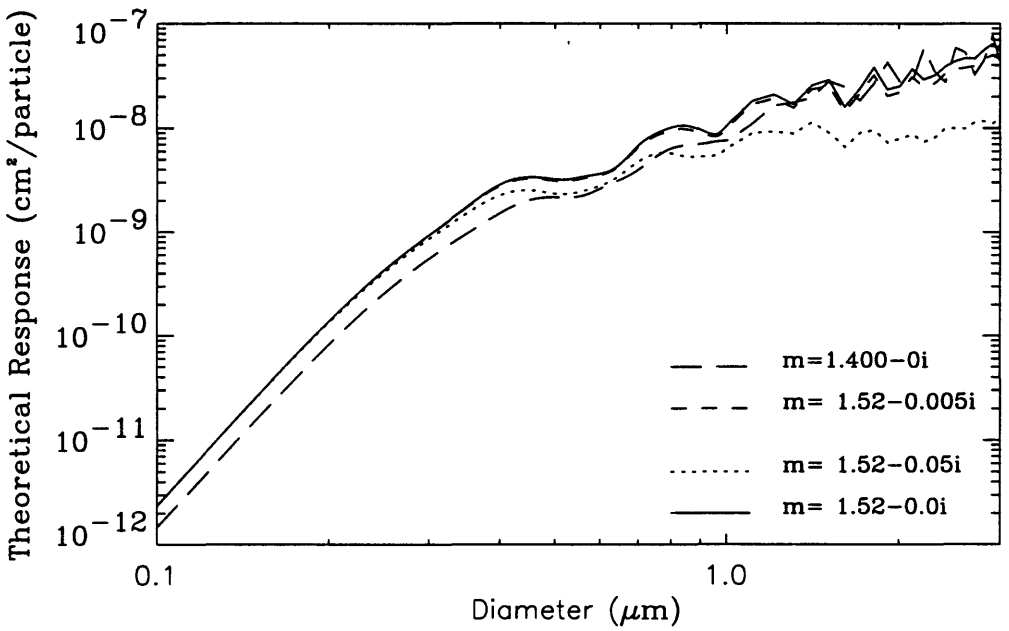

Figure 4.5.2. Mie scattering response for complex and real refractive indices.

CHAPTER 5. DETERMINATION OF WET REFRACTIVE INDEX

Section 5.1. Method

To calculate aerosol hygroscopic growth from optical particle counter data, both dry and wet properties of the aerosol must be known. In the previous section, the refractive index and density for the dry aerosol were determined, based on daily varying chemical composition. In this section, an iterative process is proposed and applied to determine the relative humidity-dependent properties of the aerosol. The pairs of dry and wet distributions for which the iterative method was applied were those used for the hygroscopicity calculations. Several concepts previously presented in this thesis, such as the data inversion and scaling method (Chapter 2), and calculations of refractive index and density (Chapter 4) were used in the iterative method. Figure 5.1.1 presents the procedure followed for the iteration method, for which each step will be described here. For each pair of distributions used to estimate hygroscopicity, the known dry parameters were aerosol accumulation mode mass ($\rho_{dry}V_{dry}$), density, real refractive index, and ASASP-X dry volume. Dry size parameters used in this section will be presented in Chapter 6.

Starting with an initial guess of wet refractive index (usually m = 1.35), ASASP-X wet distribution data were inverted using the scaling procedure discussed in Section 2.4. DISTFIT (Whitby, 1991) was applied to the resulting size distributions and wet volume and other lognormal size parameters were calculated. Using both the dry (V_{dry}) and wet volume (V_{wet}), the water volume (V_{H2O}) was calculated using equation 5.1.1. Water mass (M_{H2O}), and wet density (ρ_{wet}), were then calculated from equations (5.1.2) and (5.1.3), respectively. Water density and refractive index values used were ρ_{H2O} = 0.9971 g cm^{-3} and m_{H2O} = 1.33264. A new value of wet refractive index (m_{wet}) was calculated from equation (5.1.4) and then used to invert ASASP-X data. The entire process was repeated until the refractive index converged within a difference of 0.00001. Once this convergence

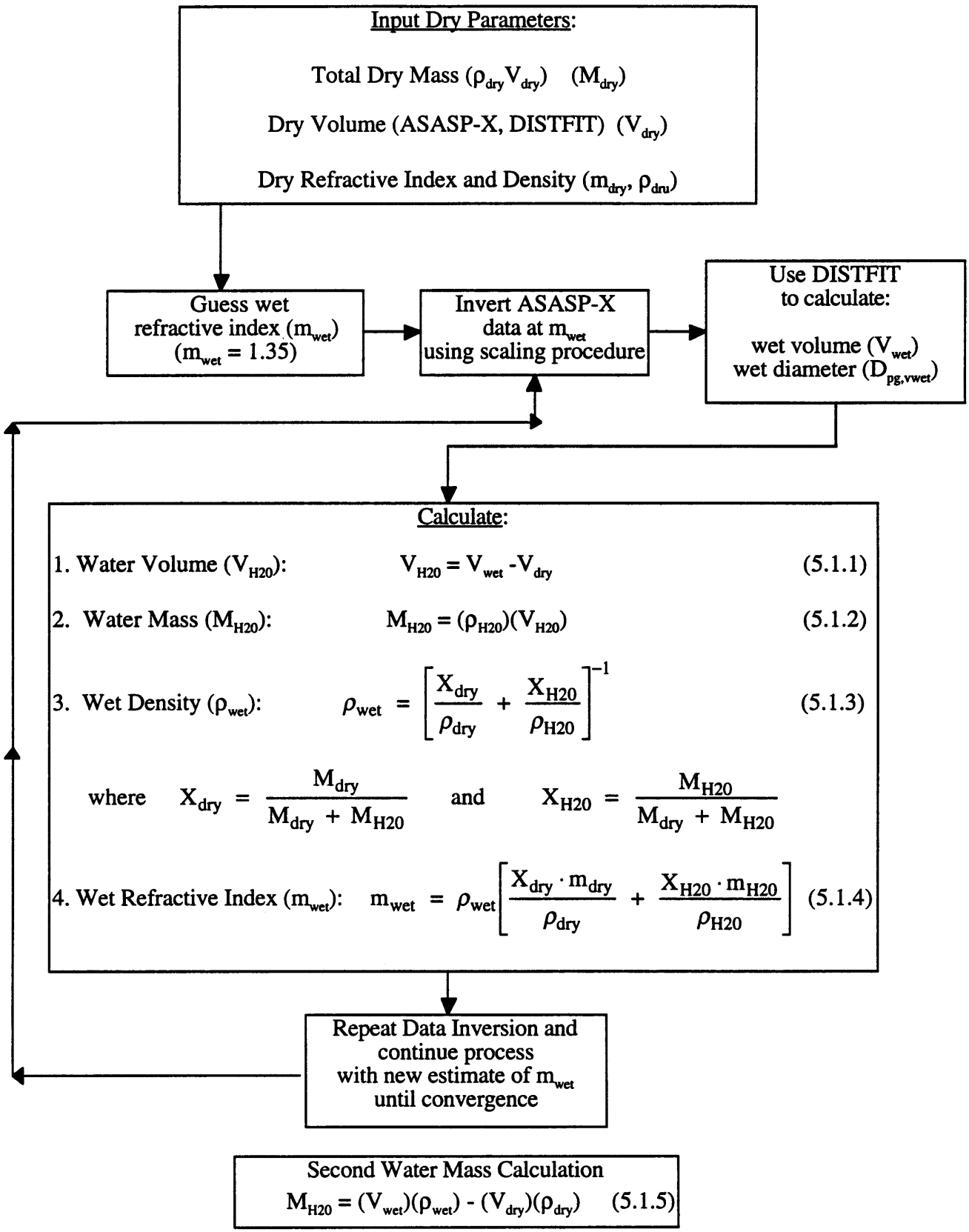

Figure 5.1.1. Wet iteration method

occurred, a second water mass calculation was performed as an internal consistency check (equation (5.1.5)). On average, this convergence required 12 iterations. For the 72 distributions for which the iterative process was applied, 11 did not converge, usually for distributions measured at low relative humidities.

Section 5.2. Sensitivity of Iteration on Input Values

Sensitivity of results from the iterative method to uncertainty in the input values was investigated. Sensitivity tests were performed for the starting value of wet refractive index, the input dry volume derived from the ASASP-X, and dry density and refractive index.

The starting wet refractive index had no impact on the resulting converged values. The initial iteration always resulted in a large increase of wet refractive index (e.g., m=1.35 to m=1.42) regardless of whether the initial wet refractive index was m=1.35 or m=1.33. Based on this outcome, the starting value of wet refractive index was taken to be m=1.35 for all iterations.

In order to understand the sensitivity of converged results to the dry input values, the iteration method (equations 5.1.1-5.1.5) was reduced to its functional dependence on one value, namely, the dry mass fraction, X_d. Dry and wet mass (M_d, M_w) can be written as equations (5.2.1) and (5.2.2), respectively.

$$M_d = \frac{\pi}{6} N_d \rho_d D^3_{pvm,d} \qquad (5.2.1)$$

$$M_w = \frac{\pi}{6} N_w \rho_w D^3_{pvm,w} = M_d + M_{H20} \qquad (5.2.2)$$

where N_w and N_d are the wet and dry accumulation mode number concentrations and $D_{pvm,w}$ and $D_{pvm,d}$ are the volume mean wet and dry diameters. Dividing equation (5.2.1) by (5.2.2) results in the dry mass fraction, X_d, (equation 5.2.3).

$$X_d = \frac{M_d}{M_d + M_{H20}} = \frac{N_d \rho_d D^3_{pvm,d}}{N_w \rho_w D^3_{pvm,w}} \qquad (5.2.3)$$

The wet volume mean diameter can be determined by multiplying the volume mean diameter corresponding to a wet distribution inverted at $m = 1.53$ by the diameter scaling factor, f_d. Recall from Section 2.4 that f_d depends on a particular refractive index (for this application, the wet refractive index, m_w). Substituting $f_D \cdot D_{pvm(1.530)}$ for $D_{pvm,w}$ in equation (5.2.3), and rearranging, equation (5.2.4) was derived.

$$f(X_d) = \frac{N_d \rho_d D^3_{pvm,d}}{N_w \rho_w D^3_{pvm\,(1.53)}}\left[1.759m_w^2 - 5.9873m_w + 6.0436\right]^{-3} - X_d \qquad (5.2.4)$$

where $$m_w = \rho_w \left[\frac{X_d m_d}{\rho_d} + \frac{(1-X_d) m_{H20}}{\rho_{H20}}\right]$$

and $$\rho_w = \left[\frac{X_d}{\rho_d} + \frac{(1-X_d)}{\rho_{H2O}}\right]^{-1}$$

The entire right hand side of equation (5.2.4) is a function only of known dry parameters, $D_{pvm,(1.53)}$, and the unknown X_d. Thus, equation (5.2.4) is the reduced equation for the iterative method in terms of one parameter, X_d. Figure 5.2.1 illustrates the solution to equation (5.2.4) for three different days. The roots of equation (5.2.4) for the three days correspond to the converged values of X_d. As seen from Figure 5.2.1, the solutions to equation (5.2.4) were well behaved functions of dry mass fraction, with single roots corresponding to the converged value of X_d for a given set of converged wet parameters. The curves for the three different days demonstrate the differences in converged X_d (and therefore m_w and ρ_w) for different dry inputs.

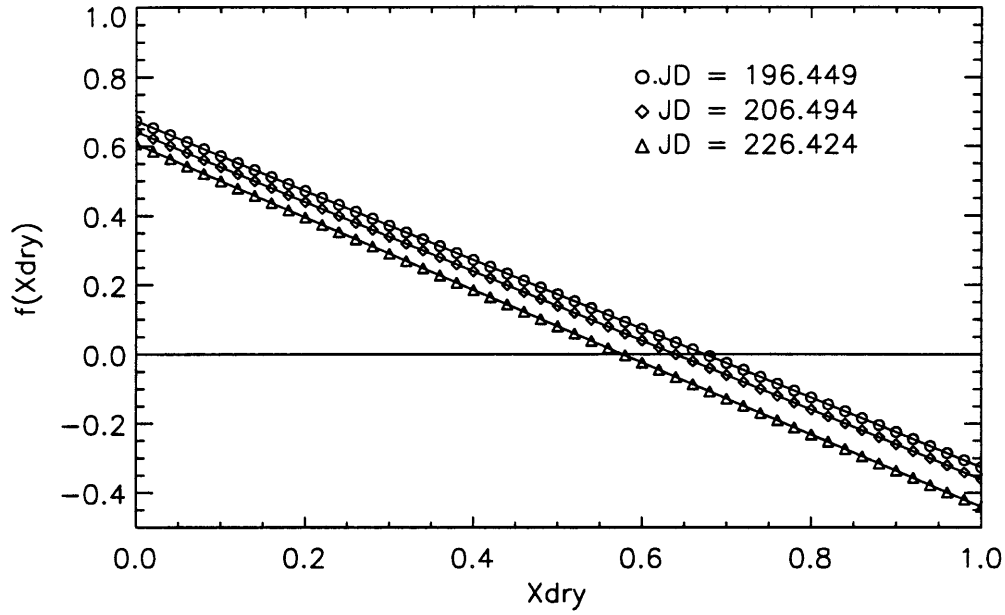

Figure 5.2.1. Solutions to equation (5.2.4) demonstrating the dependence of the iteration method on the dry mass fraction.

Sensitivity of X_d to dry input values was investigated by varying values of ρ_d, m_d, and $D_{pvm,d}$ in equation (5.2.4) by ± 10%. The actual values of these dry parameters corresponding to the days in Figure 5.2.1 are reported in Table 5.2.1. In Table 5.2.2, the effects of these variations on X_d are reported.

Table 5.2.1. Dry parameters for three SEAVS study days. Dry mass fraction values correspond to converged values in Figure 5.2.1.

JD	ρ_d (g cm^{-3})	m_d	$D_{pvm,d}$ (μm)	X_d
196.449	1.605	1.509	0.2591	0.675
206.494	1.5949	1.503	0.1851	0.635
226.424	1.6062	1.4719	0.2538	0.577

Table 5.2.2. Percent changes of converged X_d due to 10 % variations in dry parameters.

JD	ρ_d (g cm^{-3})		m_d		$D_{pvm,d}$ (μm)	
%	+10	-10	+10	-10	+10	-10
196.449	+2	-4	+23	-19	+32	-27
206.494	+6	-4	+24	-17	+34	-26
226.424	+6	-5	+23	-15	+30	-25

An increase in dry parameters resulted in an increase in X_d for all days. Variations in dry density had the smallest effect compared to dry refractive index and volume mean diameter variations. Decreasing dry parameters by ten percent resulted in decreases in the converged values of X_d for all days, with variations in the volume mean diameter having the greatest effect. Positive variations in dry parameters usually resulted in larger variations in X_d compared to negative variations for all three days. Sensitivity of iterated results to volume mean diameter was equivalent to sensitivity to variations in dry volume. Investigating this sensitivity was important because total number concentration may not remain constant from wet-to-dry distributions, therefore the total dry volume may undergo fluctuations during the duration of the measurements. Data were disgarded for conditions with variations in total number concentration (Ames and Kreidenweis, 1996), but this procedure was not exact.

A small dry volume limit test was performed for these three distributions by assuming zero dry volume and applying the iterative method. For the cases in Figure 5.2.1, the wet refractive index and density reduced to that of water, as would be expected for no dry volume concentration.

Section 5.3. Experimental Water Mass

Two methods for were used for calculating water mass (equations 5.1.2 and 5.1.5). The first method (method 1) calculated from equation (5.1.2) took into account

water density and wet and dry volume. The second method (method 2) determined from equation (5.1.5) included wet and dry density as well as wet and dry volume. Both calculations resulted in the same experimental water mass concentration, as expected from a manipulation of equations (5.1.1)-(5.1.5).

Figures 5.3.1 (a-d) present water mass and water mass fraction (X_{H20}) as a function of wet parameters. Figure 5.3.1a presents water mass as a function of relative humidity. For increasing RH, water mass also increased, as expected. Figure 5.3.1b shows increasing wet volume with increasing water mass (at varied RH). Figures 5.3.1c and 5.3.1d present X_{H20} as a function of wet density and wet refractive index. Increased water mass fraction resulted in decreased refractive index and density, as expected. It should be recognized, however, that the data presented in Figure 5.3.1(a-d) were measured over the entire study at various relative humidities (and various chemical compositions), therefore, some scatter will result.

Section 5.4. Predicted Water Mass From Theory

In order to compare experimentally derived water mass to theory, the EQUILIB chemical equilibrium model (Pilinis and Seinfeld, 1987) was applied. This model was chosen for its ability to interpolate between degrees of neutrality for ammoniated sulfate species, but it does not account for nonequilibrium water content in the efflorescence branch. The required inputs to the model were species mass concentrations for the ammonium/chloride/nitrate/sodium/sulfate/water system, along with temperature and relative humidity. For this application, it was assumed that sulfate species were the only hygroscopic species. Daily IMPROVE mass concentrations of SO_4^{-2} and NH_4^+ were input as total H_2SO_4 and NH_3, along with the relative humidity corresponding to each measured distribution. The temperature dependence of the relative humidity of deliquescence (RHD) was determined from equation (5.4.1) (Kim and Seinfeld, 1993):

$$\ln RHD(T) = \ln RHD(T_o) - \alpha\left(\frac{1}{T} - \frac{1}{T_o}\right) \qquad (5.4.1)$$

For $(NH_4)HSO_4$ and $(NH_4)_3H(SO_4)_2$, RHD was assumed to be independent of temperature because α (a constant specific to each salt) was unknown, however, for $(NH_4)_2SO_4$, $\alpha = 0.8$. For the temperature range observed during SEAVS, (17 - 32°C, Sherman, *et al.*, 1997) the deliquescence relative humidity for $(NH_4)_2SO_4$ ($RHD(T_o)$ = 79.97% at T_o = 298.15 K) varied from 79.96% to 79.98%. Running EQUILIB at the temperature extremes (17°C and 32°C) did not affect the resulting predicted water mass. It was therefore assumed that temperature was not an important factor in the ammoniated sulfate system, and a constant temperature of 25°C was used for each model run.

To check EQUILIB results, total sulfate and ammonium concentrations in the aerosol phase were compared to input concentrations, and there was good agreement. Gas phase ammonia was not predicted for any of the cases, as was expected because sulfate was never completely neutralized.

EQUILIB predicted much larger water mass concentrations for most cases. There were some cases when the experimental mass was larger, and some cases when the agreement was fairly good. A closer look at these specific cases, with particular investigation of ammonium to sulfate molar ratio and relative humidity, follows.

Case I (EQUILIB water ≈ Experimental water)

Cases when experimental water agreed within 10% of predicted water occurred four times (out of a total of 61 cases). These cases corresponded to an average ammonium to sulfate molar ratio of 1.22 and relative humidity between 43-73 %.

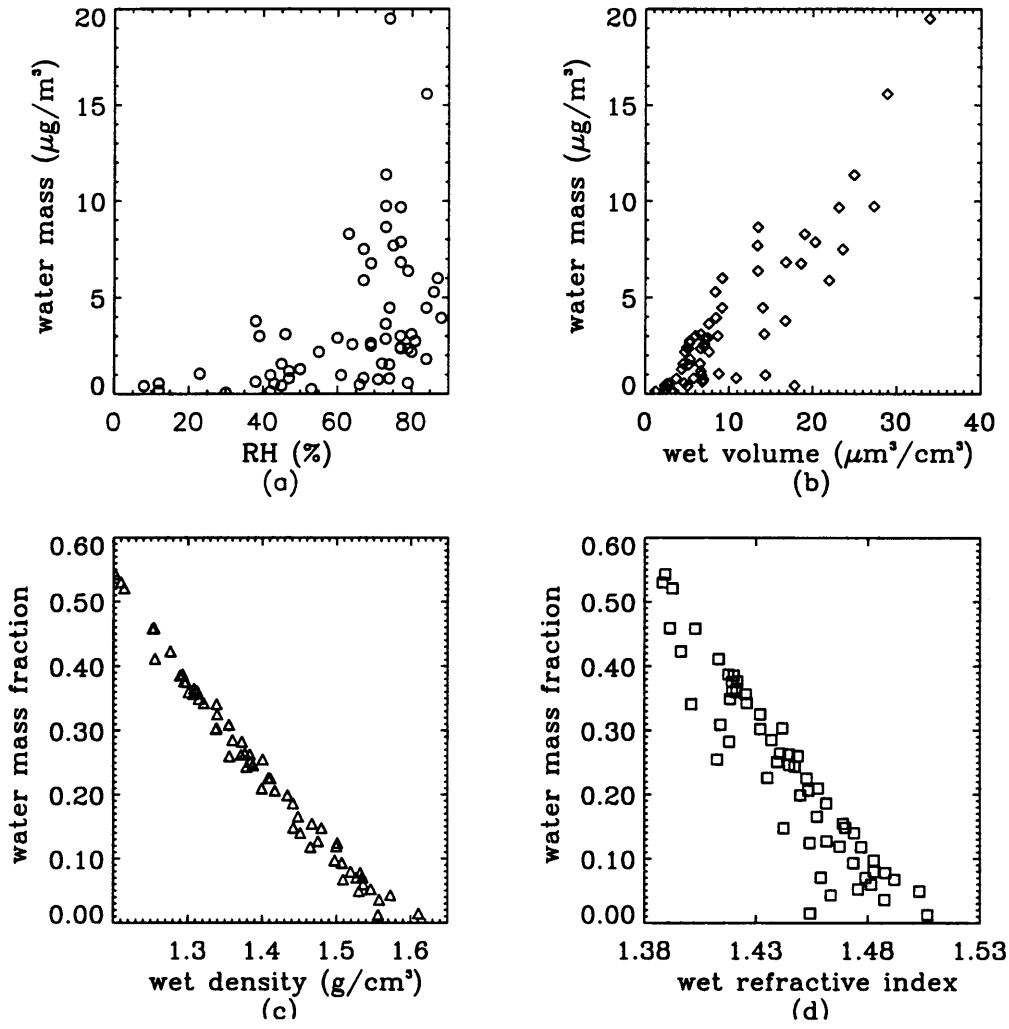

Figure 5.3.1. Water mass and water mass fraction (X_{H2O}) versus wet parameters.

Case II (EQUILIB water < Experimental water)

Nineteen cases had experimental water values at least 20% greater than theory predicted. For nine of these cases, EQUILIB predicted no water, corresponding to relative humidities below that of deliquescence for most ammoniated sulfate compounds (typically below 40% RH), and for molar ratios > 1.1

Case III (EQUILIB water > Experimental water)

These 42 cases corresponded to a range in relative humidity (8-88 %). With the exception of a few cases, the average molar ratio of ammonium to sulfate was 0.88. For pure ammoniated sulfate compounds, EQUILIB most likely predicted more water due to high hygroscopic growth of the acidic aerosols.

The frequency of larger theoretically predicted values of water mass led to the investigation of the dry mass used in the iteration and EQUILIB calculations. IMPROVE ammonium and sulfate mass concentrations representing the accumulation mode were used as inputs to EQUILIB, since the iteration calculations used only accumulation mode mass derived from ASASP-X volume concentrations and dry density values (D_p approximately less than 1 μm). Figure 5.4.1 demonstrates the differences between these two masses.

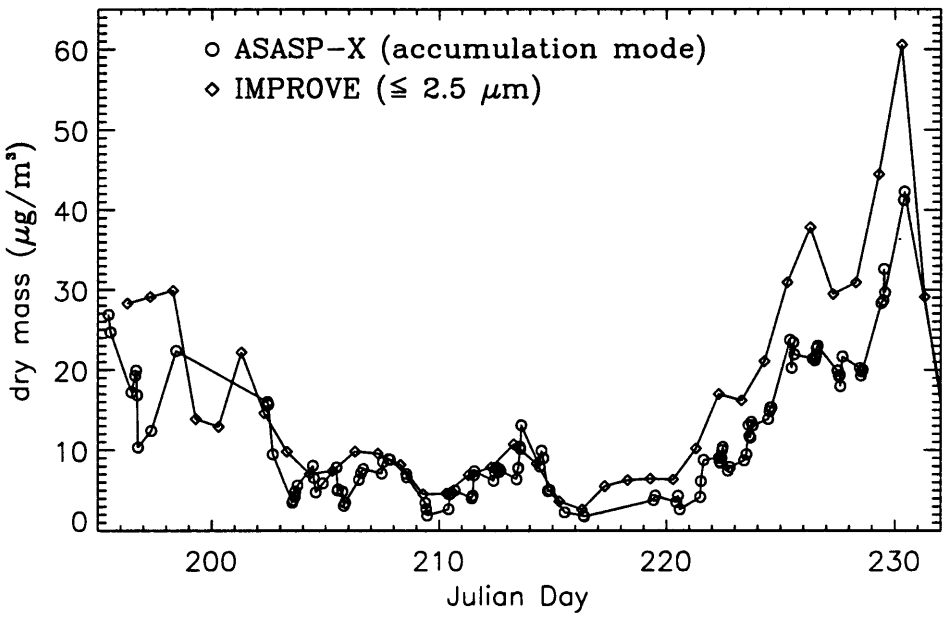

Figure 5.4.1. Dry accumulation mode and IMPROVE mass during SEAVS.

Especially noticeable is the higher IMPROVE mass during the periods when ammonium and sulfate were major contributors to total mass (see Figure 4.3.1). Although the fractional contributions of ammonium and sulfate to the accumulation mode mass were

set to be the same as for the IMPROVE mass, the resulting ammonium and sulfate accumulation mode mass concentrations were generally much lower than those from IMPROVE. Higher IMPROVE values of ammonium and sulfate mass concentrations in EQUILIB would lead to larger values of predicted water mass, especially during the hazy period (JD 226-230) when the aerosol particles were acidic and therefore quite hygroscopic.

Figure 5.4.2 presents a scatter plot of EQUILIB and experimental water mass ratios (ratios of water mass concentration to ammonium and sulfate mass concentration). Twenty-eight cases corresponded to larger experimental values, 33 cases corresponded to larger EQUILIB values, and 7 of these cases were in good agreement (within 15% difference). Figure 5.4.3(a,b) illustrates the variation of water mass ratio with relative humidity during SEAVS.

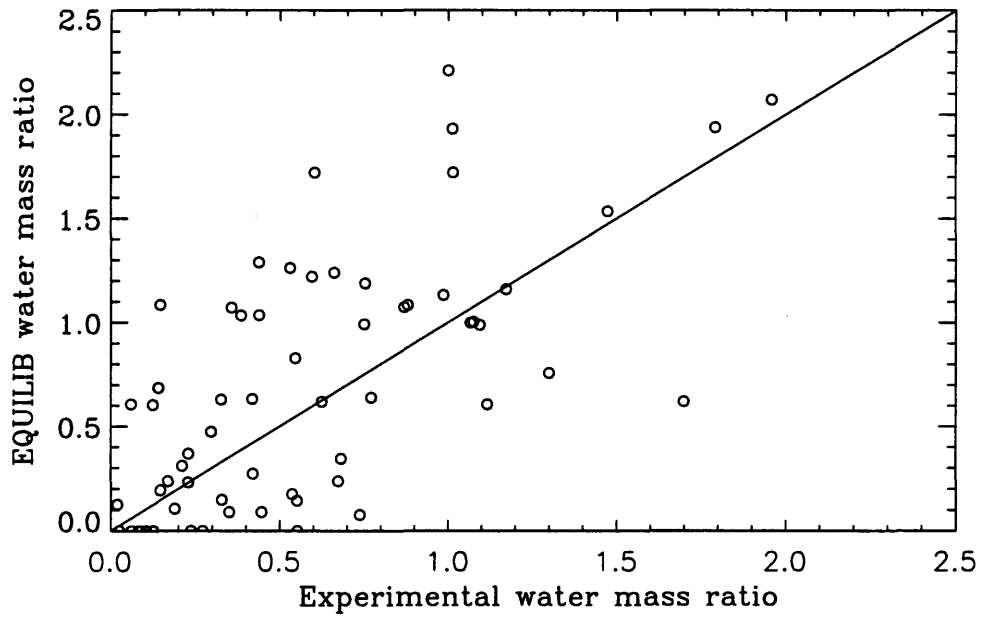

Figure 5.4.2. Comparisons of EQUILIB and experimental water mass ratio (assuming only ammonium and sulfate species were hygroscopic).

The sensitivity studies reported in Section 5.2 were extended to the derived water mass ratios presented in Figure 5.4.2. Equation (5.4.1) was derived to determine these effects, where X_d is the dry mass fraction, and R denotes the water mass ratio.

$$\frac{dR}{R} = -\left(\frac{d(X_d)}{X_d}\right)\cdot\left(\frac{1}{1-X_d}\right) \qquad (5.4.1)$$

It should be noted from equation (5.4.1) that a positive deviation in X_d resulted in a decrease in the water mass ratio, R, as would be expected because a larger dry mass fraction would correspond to less water. Table 5.4.1 reports percent changes in R corresponding to the largest percent changes in X_d from Table 5.2.2.

Table 5.4.1. Sensitivity of water mass ratio to changes in X_d. Percent changes in X_d correspond to positive and negative variations in volume mean diameter.

JD	% Change in X_d		% Change in R	
196.449	+32	-27	-98	+83
206.494	+34	-26	-93	+71
226.424	+30	-25	-71	+59

Derived water mass ratio is very sensitive to changes in dry volume mean diameter ($D_{pvm,d}$), and less sensitive to changes in dry density and refractive index. Accurate determination of $D_{pvm,d}$ is therefore very important for deriving water mass concentration, however calculation of this parameter depends on accurate estimates of density and refractive index due to the nature of the data inversion.

Other differences between experimental and predicted values of water mass could be due to the presence of organic carbon. Saxena *et al.* (1995) reported the negative and positive effects of organic carbon on particle hygroscopicity for various locations. For an urban location, the effect of organics was to diminish the water absorption by inorganics by 25-35% in the relative humidity range of 83-93%. For a nonurban location, organics enhanced water absorption by inorganics by 25-40% in the relative humidity range of 80-88%. Similar analyses were performed for these data, however, no clear trends were observed, partly due to the sparseness of the data. It was conceivable, however, that the

presence of organic carbon did act to influence the particle hygroscopicity due to its relative abundance in the aerosol total mass.

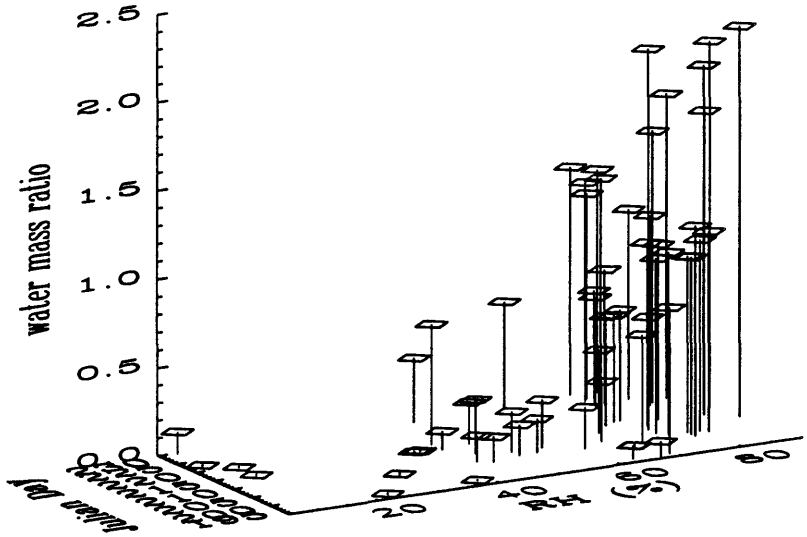

(a) EQUILIB

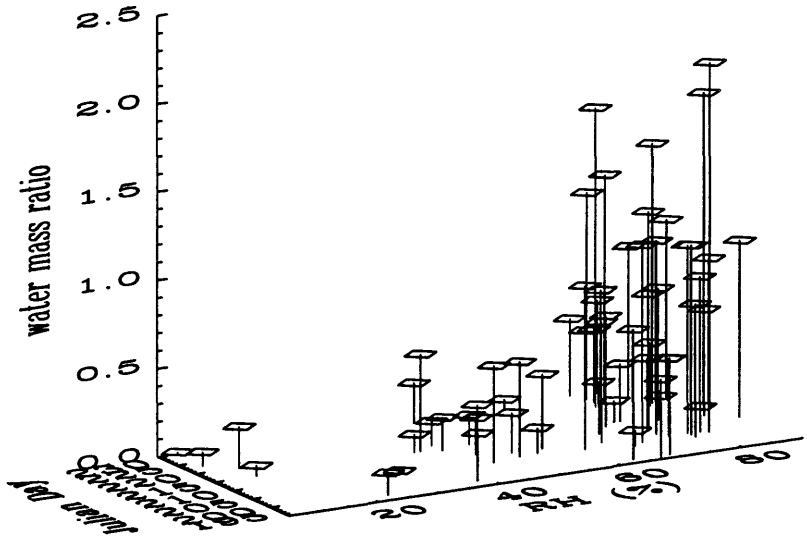

(b) Experimental

Figure 5.4.3.(a,b) EQUILIB and experimental water mass ratio as a function of relative humidity during SEAVS.

CHAPTER 6. SEAVS RESULTS BASED ON DAILY VARYING CHEMICAL COMPOSITION

The previous chapters presented the calculations of the daily varying aerosol refractive index during SEAVS. These refractive indices will now be used to estimate dry accumulation mode aerosol size parameters employing the same calibration method and lognormal fitting program discussed in Section 3.1. The appropriate refractive index was applied to each distribution in the data inversion. Revised estimates of hygroscopicity (D/D_o), light scattering coefficients (b_{sp}), and light scattering growth curves (b/b_o) will be presented, for both non-absorbing and absorbing aerosol. Sensitivity studies reported in Appendix B demonstrate the effects of elemental carbon and daily varying refractive index on these results.

Section 6.1. Accumulation Mode Dry Size Parameters for Non-Absorbing Aerosol

Figure 6.1.1 presents timelines of dry accumulation mode aerosol lognormal size parameters with varying chemical composition. Refractive indices used for the data inversion were presented in Figure 4.4.2. On average, size parameters increased from those obtained in Section 3.1 using the rural aerosol model refractive index, however, the trends with time remained the same. Table 6.1.1 provides study average, maximum, and minimum values and standard deviations of size parameters during SEAVS. The average dry refractive index ($m = 1.49 \pm 0.02$) was less than that used for dry aerosol in the rural aerosol model ($m = 1.53$), therefore the data inversion resulted in larger size parameters. Comparisons of Tables 3.1.2 and Table 6.1.1 demonstrate that although the average values do not increase significantly, the maximum and minimum values did increase for the daily varying refractive index case, with the largest increase occurring for the maximum volume concentration (18 %). Appendix B presents comparisons of each size parameter for the rural aerosol model and daily varying refractive index cases.

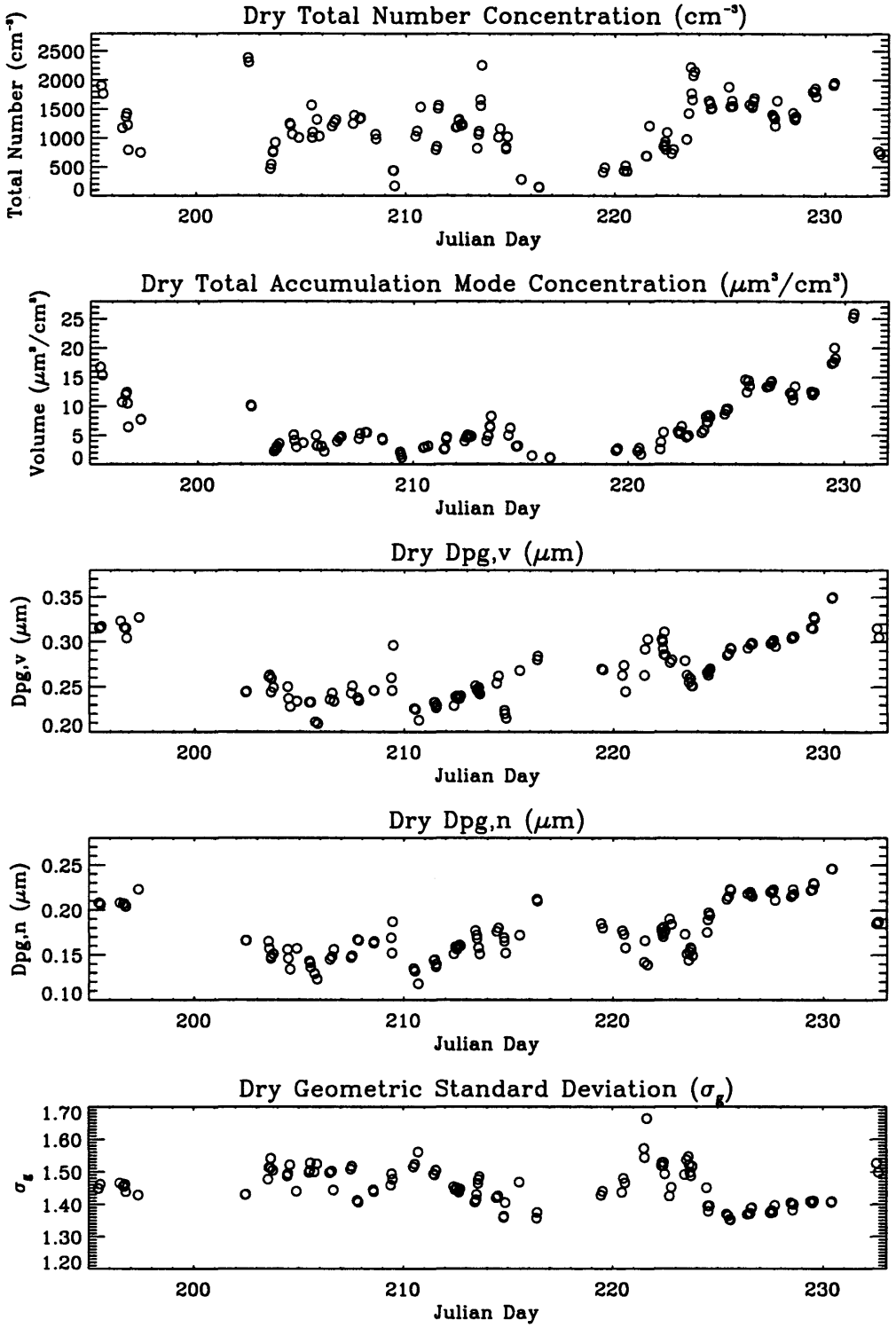

Figure 6.1.1. SEAVS timelines of dry (RH < 15%) accumulation mode lognormal size parameters for daily varying refractive index.

Table 6.1.1. Average dry accumulation mode size parameters for the SEAVS study, based on varying chemical composition and no absorbing components.

Size Parameter	Study Average	Standard Deviation	SEAVS Maximum	SEAVS Minimum
N (cm^{-3})	1200	± 500	2385	145
V ($\mu m^3 m^{-3}$)	7	± 5	25.92	1.1
$\overline{D}_{pg,n}$ (μm)	0.18	± 0.03	0.246	0.118
$D_{pg,v}$ (μm)	0.27	± 0.03	0.35	0.209
σ_g	1.45	± 0.06	1.664	1.352

Section 6.2. Hygroscopicity (D/D_o)

Hygroscopic growth was calculated similarly to Section 3.2, but with size distributions derived from daily varying wet and dry refractive indices. Results of diameter and accumulation mode volume ratios can be found in Figures 6.2.1a and 6.2.1b, respectively. Fourth-order polynomials corresponding to the data are also plotted. For an 85% relative humidity, $D_d/D_{d,o} \approx 1.24$ and $D_v/D_{v,o} \approx 1.29$, similar to the rural aerosol model case (Figures 3.2.2a,b). The values remained within the two hygroscopic modes observed by Svenningsson *et al.* (1992) (1.1 ± 0.07 and 1.44 ± 0.14). Although values of hygroscopicity less than unity existed in Figures 3.2.2(a,b), the number of these cases decreased for the daily varying refractive index cases (Figures 6.2.1a,b), suggesting more consistent values of wet and dry refractive index. Sensitivity studies reported in Appendix B suggested good agreement between hygroscopicity for the daily varying refractive index and rural aerosol model. A conclusion from this result was that although daily variations in chemical composition resulted in larger size

parameters for both wet and dry distributions, ratioing the two parameters nearly canceled the effect.

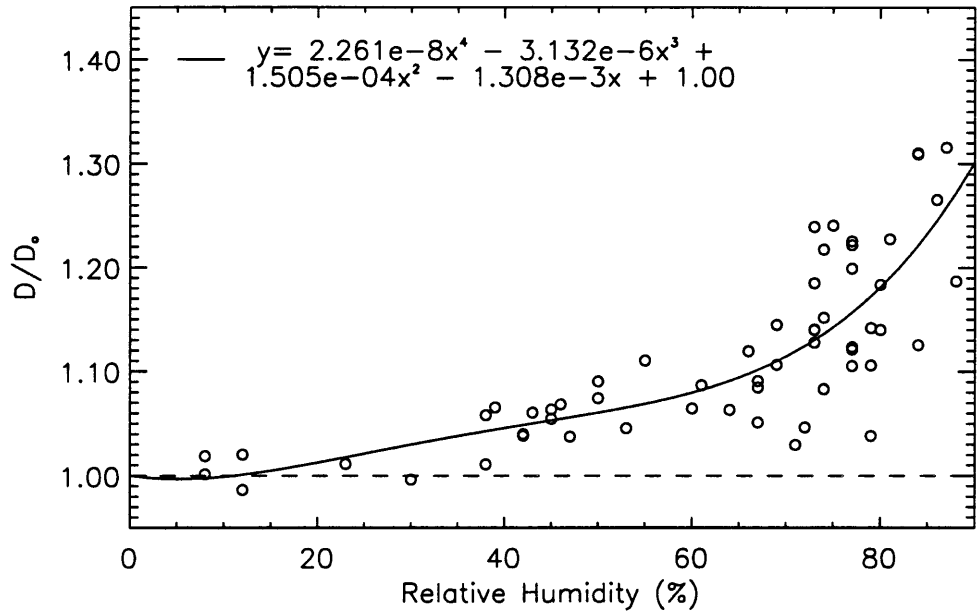

Figure 6.2.1(a). Hygroscopicity estimates using diameter ratios for daily varying refractive index.

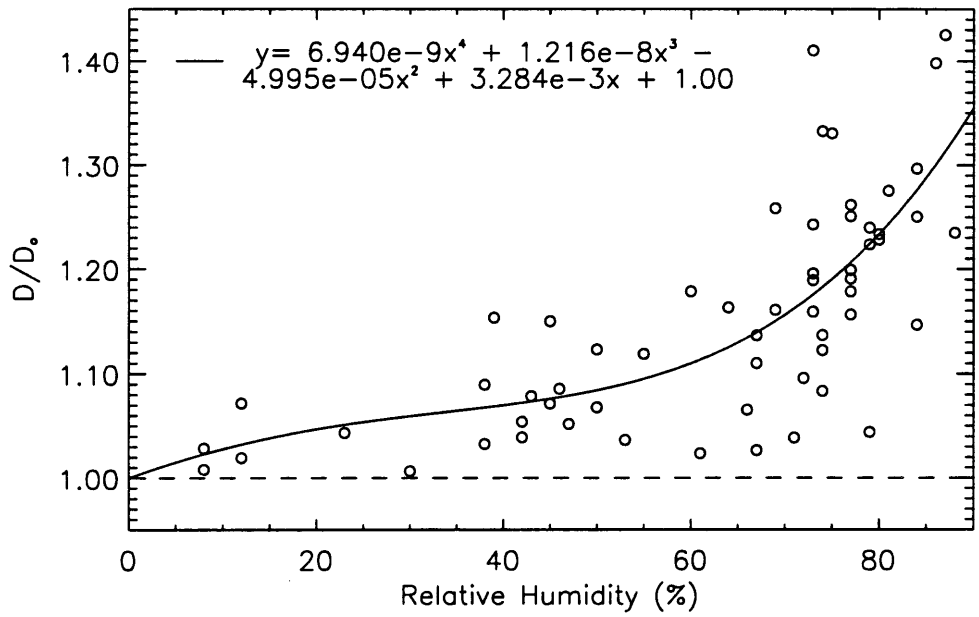

Figure 6.2.1(b). Hygroscopicity estimates using accumulation mode volume ratios for daily varying refractive index.

The significance of this observation is that although the aerosol chemical composition is needed to determine aerosol size parameters, it may not be critical for deriving hygroscopicity (or other ratios of size parameters). This result may be specific to this study, as the variation in refractive index with relative humidity assumed in the rural aerosol model was likely a good estimate for that observed during SEAVS (see Figure 6.2.2).

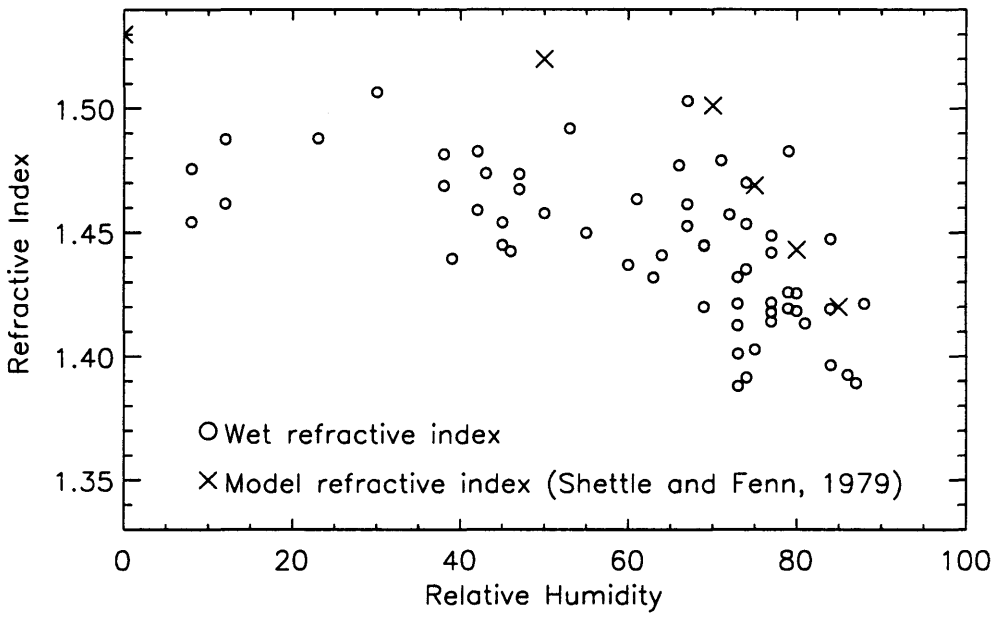

Figure 6.2.2. Relative humidity versus iterated refractive index for SEAVS. Also plotted are interpolated refractive indices derived from Shettle and Fenn (1979) (Ames and Kreidenweis, 1996).

Section 6.3. Particle Light Scattering (b_{sp})

Particle light scattering coefficients were recomputed using daily varying values of dry and wet real refractive index and corresponding size parameters. Figure 6.3.1 presents timelines of these estimates of b_{sp} along with semi-empirical b_{sp} and nephelometer measurements, illustrating good agreement between nephelometer and ASASP-X b_{sp}. Comparisons of b_{sp} calculated with varying and constant dry refractive

index are reported in Appendix B. The study average b_{sp} for the daily varying refractive index was 0.0406 km^{-1}, compared to 0.0440 km^{-1} for the rural aerosol model. As discussed in Section 3.3.1, calculations of b_{sp} depend on refractive index, size parameter, scattering efficiency, and number concentration. Particle scattering would increase for larger refractive index, as well as for larger size particle (depending on the value of the scattering efficiency). In comparison to the rural aerosol model, the lower daily varying refractive indices resulted in larger inverted particle sizes, effects which act oppositely on b_{sp}. Overall, the effects of larger refractive index dominated, resulting in larger values of dry b_{sp} for the rural aerosol model, despite the smaller median diameters.

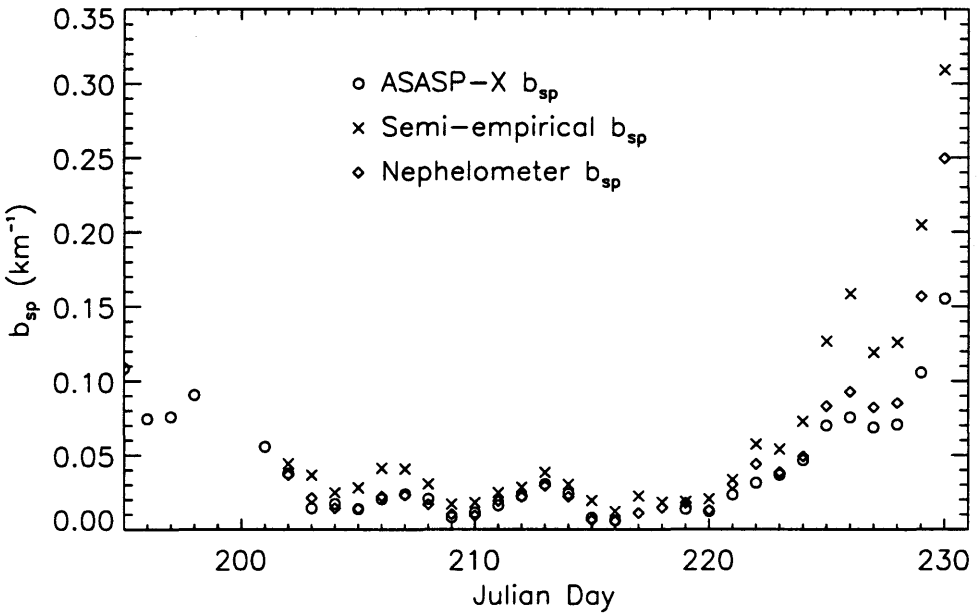

Figure 6.3.1 Dry (RH < 15%) particle light scattering coefficients from ASASP-X, nephelometer, and semi-empirical estimates using daily varying refractive indices.

Section 6.4. Particle Light Scattering Growth Curve (b/b_o)

The scattering growth curve calculated from the ratio of $b_{sp,wet}$ and $b_{sp,dry}$ is shown in Figure 6.4.1, along with a fourth-order polynomial fit. One noticeable difference between these results and those reported in Chapter 3 was a decrease in the amount of

scatter in the values, with all values greater than unity. More realistic estimates of wet refractive index may have accounted for this. The magnitude of b/b_o at RH = 85% increased from ≈ 1.9 in Chapter 3 to ≈ 2.1, most likely due to increases in $b_{sp,wet}$ for the iterated wet refractive indices. These results were compared to nephelometer b/b_o results and agree well (see Figure 6.4.1) (Day *et al.*, 1996).

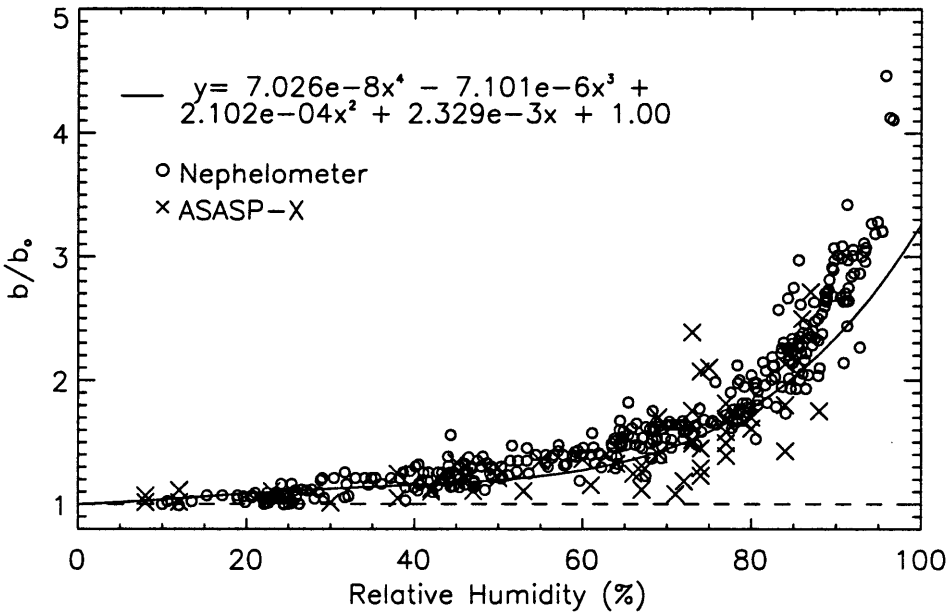

Figure 6.4.1. Estimates of b/b_o for daily varying non-absorbing refractive index from measurements made with a radiance research nephelometer and the ASASP-X. The polynomial fit corresponds to ASASP-X data.

Section 6.5. Absorbing Aerosols: The Effects of Including Elemental Carbon.

The complex refractive indices determined in Section 4.5 were also applied to the ASASP-X data inversion. The scaling procedure for diameter as a function of real refractive index was used as an approximation for the inversion (e.g., only the real part of the refractive index was considered in the data inversion). The real part of the average dry complex refractive index during the study increased slightly from $m = 1.49$ to $m = 1.51 - 0.0184\,i$. As was seen in Figure 4.5.2, the Mie scattering response decreased with non-

zero imaginary part of refractive index above D_p = 0.4 μm. The derived size parameters for diameters above this value were therefore underestimated by the scaling procedure. The study average dry accumulation mode size parameters for absorbing aerosol were the same as for the non-absorbing case (see Table 6.4.1), except σ_g increased from 1.45 to 1.46.

The differences in calculated hygroscopicity, when compared to estimates for non-absorbing aerosol, were insignificant due to the small changes in size parameters. Differences were expected in light extinction, which was calculated in a similar manner to that described in Section 3.3.1. The light absorption coefficient, b_{ap}, was determined by calculating both the light extinction and scattering and taking the difference, as in equation (6.4.1):

$$b_{ap} = b_{ext,p} - b_{sp} \qquad (6.4.1)$$

Figures 6.5.1(a,b) show timelines of $b_{ext,p}$, b_{sp}, and b_{ap} for the absorbing aerosol measured during SEAVS. Light scattering coefficient was similar to the non-absorbing case, however the light extinction increased due to the added absorption. Particle absorption coefficients (b_{LAC}) were estimated from elemental carbon concentrations, assuming an absorption efficiency of 10 $m^2\ g^{-1}$. Figure 6.5.1b illustrates good agreement of these estimates of b_{ap} with trends in time and in magnitude. This agreement was expected because both estimates were made from elemental carbon concentrations.

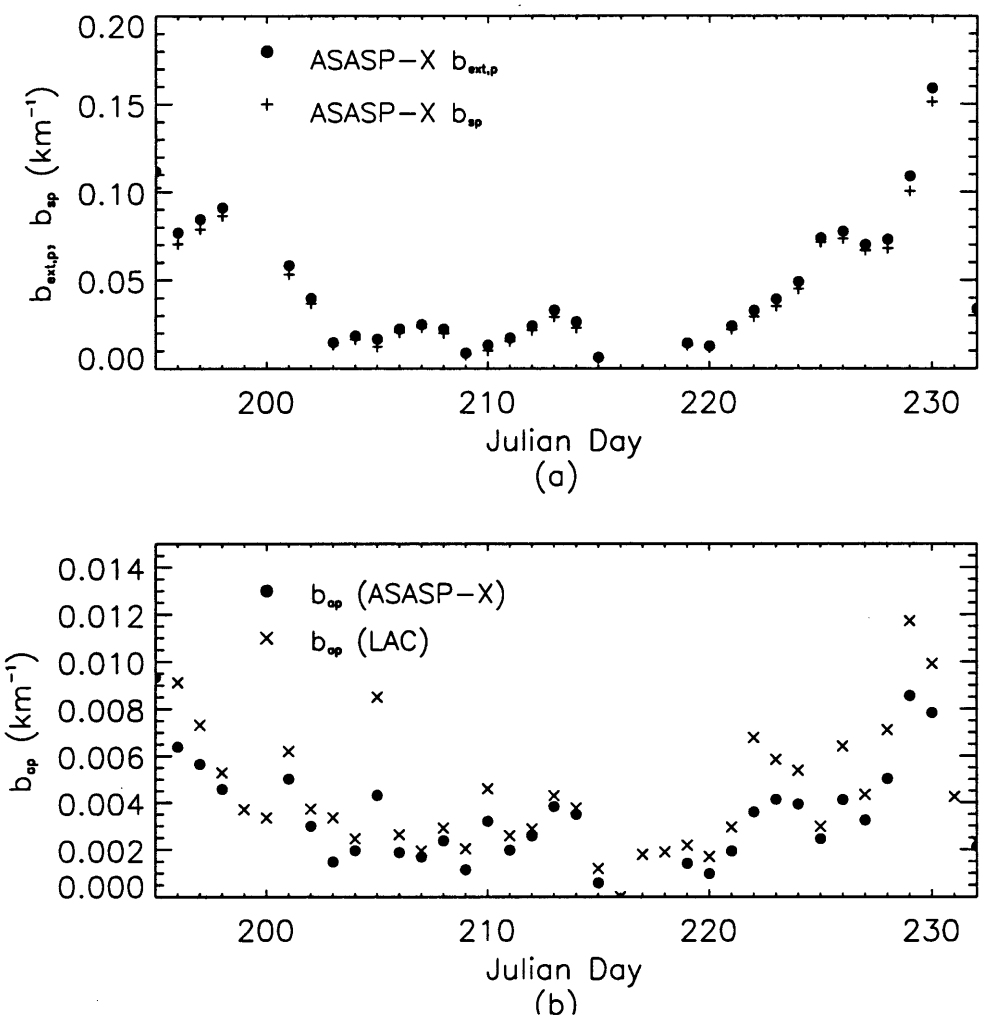

Figure 6.5.1(a-b). **(a)** Estimates of ASASP-X $b_{ext,p}$ and b_{sp}, (km^{-1}) for aerosol with daily varying absorbing chemical composition. **(b)** Estimates of absorption coefficients (b_{ap}) from the ASASP-X and from elemental carbon measurements assuming an absorption efficiency of 10 m^2 g^{-1}.

CHAPTER 7. CONCLUSION

Optical aerosol measurements made during SEAVS resulted in the determination of lognormal size parameters, aerosol hygroscopicity, and light scattering coefficients. Daily varying dry refractive indices were calculated using the partial molar refractive index method (Stelson, 1990), and IMPROVE chemical composition data. Although these calculations were made for dry aerosol, a small amount of water corresponding to a 10% by mass ammonium and sulfate solution was included. Because of the average high ambient relative humidity at the study site, it was assumed that the RH controlled aerosol measurements occurred on the efflorescence curve (the aerosol were being dried, not humidified) and some water was always associated with it. Other chemical species included in the dry refractive index calculation were NH_3^+, SO_4^{-2}, organic carbon and KNO_3. Elemental carbon was included in a separate calculation to test the sensitivity of absorbing aerosol on light scattering calculations. A study average dry real refractive index of $m = 1.49 \pm 0.02$ was derived, along with an average dry density of $\rho = 1.59 \pm 0.02$ g cm^{-3}.

Number distribution data from the ASASP-X were inverted by a scaling procedure developed to take into account any real refractive index. Number distributions were fit with a single mode lognormal function (Whitby, 1991) from which size parameters were determined. A study average dry (RH < 15%) number median diameter was determined to be 0.18 ± 0.03 μm. Study average dry accumulation mode volume concentration and volume median diameter were calculated to be $V = 7 \pm 5$ μm^3 cm^{-3} and $D_{pg,v} = 0.27 \pm 0.03$, respectively. A study average geometric standard deviation was calculated to be 1.45 ± 0.06.

A newly-developed iteration method was used to determine wet refractive index as a function of relative humidity and chemical composition. Dry accumulation mode volume

derived from the ASASP-X, accumulation mode mass, dry refractive index, and dry density were used as inputs for the iteration. Wet volume and water mass concentration as a function of relative humidity were also determined. Sensitivity studies suggested that derived water amounts were very sensitive to variations in dry volume mean diameter (equivalent to dry volume concentration), and less sensitive to dry refractive index and density by comparison. Accurate determination of volume mean diameters was therefore more important for determining water mass by this method, however, the data inversion depended on accurate estimates of dry refractive index and density.

Theoretically predicted water mass was calculated with a chemical equilibrium model (Pilinis and Seinfeld, 1986) assuming ammonium and sulfate were the only hygroscopic species. Comparisons of ratios of water mass concentration to ammoniated sulfate mass resulted in 33 of the 61 values larger for the theoretically predicted case.

Light scattering coefficients (b_{sp}) were estimated using wet and dry refractive indices. Dry b_{sp} underestimated semi-empirical light scattering results, but agreed well with nephelometer results, and followed meteorological trends observed during the study. Particle light scattering growth curves, (b/b_o), were calculated from the ratio of $b_{sp,wet}$ to $b_{sp,dry}$. Good agreement of (b/b_o) with results from nephelometer measurements were found. Hygroscopicity estimates were made from ratios of wet to dry size parameters (volume median diameter and accumulation mode volume), resulting in values ranging from 1.24 to 1.29 at 85% RH depending on the method. These results fell within the range observed by other investigators (Svenningsson *et al.* 1992), however they were lower than expected for pure ammoniated sulfate compounds.

Sensitivity studies were performed to test the assumptions made in the data inversion methods. Derived size parameters were not significantly sensitive to the assumption of a lognormal size function used to characterize the aerosol distributions. The calibration method used in the data inversion had more significant effects in the derived size parameters. Although considering daily-varying refractive indices in the data inversion

resulted in larger size parameters than the rural aerosol model of refractive index, hygroscopicity and other ratios of size parameters appeared to be relatively insensitive to varying chemical composition. This result suggested that knowledge of the daily varying chemical composition may not be critical in the estimation of hygroscopicity, however this might apply only for the conditions observed during SEAVS.

CHAPTER 8. FUTURE WORK

The results presented in this thesis were restricted to the accumulation mode. Two volume modes were shown to often exist during SEAVS, and including these modes in calculations of particle light scattering and water mass concentrations may be important depending on the chemical composition of the bimodal aerosol. The same DISTFIT lognormal fitting program will be used to perform a bimodal fit on volume distributions. The bimodal volume distributions will give estimates of the total fine mode volume concentration during the soil event (JD 206-208) when the second volume mode was significant.

Sulfur size distributions measured with a DRUM sampler during SEAVS will be investigated to determine whether significant amounts of sulfur were unaccounted for when assuming only an accumulation mode. Sulfate size distributions will be compared to the ASASP-X data to determine if the sulfate mass distributions extended beyond the accumulation mode. Sulfate mass scattering efficiencies will be calculated from ASASP-X data and compared to mass scattering efficiencies determined from the DRUM data.

It is likely that the hygroscopicity measurements during SEAVS were made on the efflorescence branch. EQUILIB water mass predictions assumed chemical equilibrium on the deliquescence branch, usually resulting in no predicted water mass concentration for lower relative humidities, compared to nonzero values of experimental water mass at the same RH. Interpolations between water uptake for ammoniated sulfate species from Tang and Munkelwitz (1994) will be determined for the efflorescence branch, allowing for estimates of predicted water mass concentration at the lower relative humidities.

Other mixing methods exist for determining complex refractive indices. In this thesis, the volume weighted method was used. Chylek *et al.* (1988) reported that other mixing rules, such as the Maxwell Garnet mixing rule, resulted in smaller values of complex refractive indices when compared to the volume weighted method. These other

methods could be used to determine complex refractive index to determine the sensitivity of results to the mixing rule.

As discussed in Section 6.5, the real part of the complex refractive indices were used with the scaling procedure to invert ASASP-X data. A modification to the scaling method needs to be derived which can take into account the imaginary part of the refractive index for more accurate estimates of absorbing aerosol size parameters. Another area of investigation to pursue regarding light absorbing aerosols is appropriate values of absorption efficiency to apply to the SEAVS data. A value of 10 $m^2 g^{-1}$ was used in this thesis, however this value has been reported to range from experimental values of 3.8-17 $m^2 g^{-1}$ and theoretical values of 8-12 $m^2 g^{-1}$ (Horvath, 1993).

Other SEAVS investigators measured aerosol hygroscopicity, size parameters, particle light scattering and refractive index using different instruments and techniques. As these data become available, comparisons will be made to the results presented in this thesis.

REFERENCES

Active Scattering Aerosol Spectrometer Probe PMS Model ASASP-X Operating Manual, Serial No. 805-0978-10, Particle Measuring Systems, 1977.

Ames, R. B., and Kreidenweis, S. M., 1996, Optical Measurements of Aerosol Size Distributions in Great Smoky Mountains National Park: Particle Hygroscopicity and its Impact on Visibility, CIRA report, ISSN 0737-5352-33, Colorado State University.

Bohren, C. F., and Huffman, D. R., 1983, Absorption and Scattering of Light by Small Particles, John Wiley and Sons, New York.

Covert, D.S., Hansson, H.-C., Winker, P., and Heintzenberg, J., 1991, The Degree of Mixing of Hygroscopic Properties in Source and Receptor Locations in Northern Europe, *Proceedings of AAAR'91*, Available from American Association for Aerosol Research, 4330 East West highway, Suit 1117, Bethesda, MD 20815

Chylek, P., Srivastava, V., Pinnick, R.G., Wang, R.T., 1988, Scattering of Electromagnetic Waves by Spherical Particles: Experiment and Effective Medium Approximations, *Applied Optics,* **27(12):** 2396-2404.

Day, D., Malm, W.C., Kreidenweis, S.M., 1996, National Park Service Contribution, Southeastern Aerosol and Visibility Study (SEAVS): A Preliminary Report, Colorado State University.

Garvey, D.M., and Pinnick, R.G., 1983, Response Characteristics of the Particle Measuring Systems Active Scattering Aerosol Spectrometer Probe (ASASP-X), *Aerosol Science and Technology,* **2**:477-488

Hand, J. L. and Kreidenweis, S. M., 1996, Size Corrections Based on Refractive Index for Particle Measuring Systems Active Scattering Aerosol Spectrometer Probe (ASASP-X), CIRA report, ISSN 0737-5352-31, Colorado State University

Handbook of Chemistry and Physics, 61st edition, 1980-1981, Editor, Weast, R.C. CRC Press, Inc, Boca Raton, Florida

Hasan, H., and Dzubay, T.G., 1983, Apportioning Light Extinction Coefficients to Chemical Species in Atmospheric Aerosol, *Atmospheric Environment,* **17(8):** 1573-1581.

Hegg, D., Larson, T, and Yuen, P. 1993, A Theoretical Study of the Effect of Relative Humidity on Light Scattering by Tropospheric Aerosols, *Journal of Geophysical Research,* **98(D10)**: 18435-18439

Hering, S. V., and McMurry, P. H., 1991, Optical Counter Response to Monodisperse Atmospheric Aerosols, *Atmospheric Environment* **25A(2)**:463-468.

Horvath, H., 1993, Atmospheric Light Absorption: A Review, *Atmospheric Environment*, **27(A:3)**: 293-317.

Kim, Y. J., 1995, Response of the Active Scattering Aerosol Spectrometer Probe (ASASP-100X) to Different Chemical Composition, *Aerosol Science and Technology*, **22**:33-42

Kim, Y. J., and Boatman, J. F., 1990, Size Calibration Corrections for the Active Scattering Aerosol Spectrometer Probe (ASASP-100X), *Aerosol Science and Technology*, **12**:665-672

Kim, Y. P., Seinfeld, J. H., and Saxena, P., 1993, Atmospheric Gas-Aerosol Equilibrium I. Thermodynamic Model, *Aerosol Science and Technology*, **19**:157-181.

Malm, W.C., Sisler, J. F., Huffman, D., Eldred, R.A., Cahill, T.A., 1994a, Spatial and Seasonal Trends in Particle Concentration and Optical Extinction in the United States, *Journal of Geophysical Research*, **99(D1)**:1347-1370.

Malm, W.C., Gebhart, K. A., Molenar, J., Cahill, T. Eldred, R., and Huffman, D., 1994b Examining the Relationship Between Atmospheric Aerosols and Light Extinction at Mount Rainier and North Cascades National Parks, *Atmospheric Environment*, **28(2)**:347-360

McMurry, P.H. and Liu, B. Y. H., 1978, The Tandem Differential Mobility Analyser Applied to Studies on Particle Growth and Gas Phase Titration. *Particle Technology Laboratory Publication Number 380.* Minneapolis, Minnesota

McMurry, P.H. and Stolzenburg, M.R., 1989. On the Sensitivity of Particle Size to Relative Humidity for Los Angeles Aerosols. *Atmospheric Environment* **23**, 497-507

Nemesure, S., Wagener, R., Schwartz, S. E., 1995, Direct Shortwave Forcing of Climate by the Anthropogenic Sulfate Aerosol: Sensitivity to Particle Size, Composition and Relative Humidity, *Journal of Geophysical Research*, **100(D12)**:26105-26116

Ouimette, J.R., and Flagan, R.C., 1982, The Extinction Coefficient of Multicomponent Aerosols, *Atmospheric Environment*, **16(10)**: 2405-2419.

Perry, K.D., Cahill, T.A., Eldred, R.A., Dutcher, D.D., Gill, T.E., 1996, Long-range Transport of Saharan Dust to the Eastern United States, submitted for publication in *Journal of Geophysical Research-Atmospheres*, August 1996.

Pilinis, C., and Seinfeld, J. H., 1983, Continued Development of a General Equilibrium Model for Inorganic Multicomponent Atmospheric Aerosols, *Atmospheric Environment*, **21(11)**:2453-2466.

Pinnick, R. G, and Auvermann, H. J., 1979, Response Characteristics of Knollenberg Light-Scattering Aerosol Counters, *Journal of Aerosol Science*, 10:55-74.

Pueschel, R. F.; Overbeck, V. R.; Snetsinger, K. G.; Russell, P. B.; Ferry, G. V.; Wilson, J. C.; Livingston, J. M.; Verma, S., and Fong, W., 1990, Calibration Correction of an Active Scattering Spectrometer Probe to Account for Refractive Index of Stratospheric Aerosols, Comparisons of Results with Inertial Impaction, *Aerosol Science and Technology*, **12**:992-1002.

Richards, L.W., Anderson, J. A., Blumenthal, D. L., McDonald, J. A., Macias, E.S., Hering, S.V., and Wilson, Jr., W.E., 1985, Chemical, Aerosol and Optical Measurements in the Plumes of Three Midwestern Coal-Fired Power Plants, *Atmospheric Environment*, **19(10):**1685-1704.

Saxena, P., Hildemann, L. M., McMurry, P. H., Seinfeld, J. H., 1995, Organics Alter Hygroscopic Behavior of Atmospheric Particles, *Journal of Geophysical Research,* **100(D9)**: 18755-18770.

Seinfeld, J.H., 1986, Atmospheric Chemistry and Physics of Air Pollution, John Wiley and Sons, New York.

Sherman, D.E., Kreidenweis, S.M., and McKee, T., 1997, The Influence of Synoptic and Local Meteorological Conditions on Ambient Particle Concentrations During the Southeastern Aerosol and Visibility Study (SEAVS), CIRA Report, ISSN No. 0737-5352-34, Colorado State University.

Shettle, E.P., and Fenn, R.W., 1979, Models for the Aerosols of the Lower Atmosphere and the Effects of Humidity Variations on Their Optical Properties, Environmental Research Paper, No. 676, AFGL-TR-79-0214

Stelson, A. W., 1990, Urban Aerosol Refractive Index Prediction by Partial Molar Refraction Approach, *Environmental Science and Technology*, **24**, 1676-1679.

Svenningsson, I. B., Hansson, H. -C., Wiedensohler, A., Ogren, J. A., Noone, K. J., Hallberg, A., 1992, Hygroscopic Growth of Aerosol Particles in the Po Valley, *Tellus*, **44B**:556-569.

Tang, I.N., Munkelwitz, H.R., Davis, J.G., 1978, Aerosol Growth Studies- IV. Phase Transformation of Mixed Salt Aerosols in a Moist Atmosphere, *Journal of Aerosol Science* **9**:505-511

Tang, I.N., 1996, Chemical and Size Effects of Hygroscopic Aerosols on Light Scattering Coefficients, *Journal of Geophysical Research*, **101(D14)**:19245-19250

Tang, I.N., and Munkelwitz, H.R., 1994, Water Activities, Densities, and Refractive Indices of Aqueous Sulfates and Sodium Nitrate Droplets of Atmospheric Importance, *Journal of Geophysical Research*, **99(D9)**:18801-18808

Whitby, E.R., 1991, DISTFIT lognormal fitting program

APPENDICES

APPENDICES

Many sensitivity studies were performed to test the assumptions made in this thesis. Sensitivity of size parameters to the lognormal fits of aerosol size distributions will be investigated in Part I of Appendix A. This sensitivity study was performed on the size distributions presented in Ames and Kreidenweis (1996), therefore the calibration and rural aerosol model of refractive index and relative humidity (Shettle and Fenn, 1979) used in that work was assumed for Part I.

In the Part II of Appendix A, sensitivity of derived size parameters to instrument calibration and data inversion methods was investigated. Comparisons of lognormal size parameters derived from two different instrument calibrations will be presented.

Appendix B includes sensitivity studies on the effects of refractive index and chemical composition on data inversion. Studies reported in Part I of Appendix B compare the application of daily varying dry refractive indices in the data inversion to a constant dry refractive index used in a rural aerosol model. The effects of absorbing aerosols on light extinction coefficients will be investigated in Part II of Appendix B.

The sensitivity studies reported in Appendix A and B correspond to assumptions made in this thesis: lognormal fits to aerosol size distributions, instrument calibration and data inversion methods, and the effects of daily varying chemical composition and refractive index on derived results. These studies suggest that of these assumptions, sensitivity to the instrument calibration used in the data inversion was the most significant.

APPENDIX A.

Part I. Sensitivity to Lognormal Fits and Instrument Calibration

The aerosol size distributions measured during SEAVS were fit with a lognormal fitting program called DISTFIT (Whitby, 1991). Aerosol number distributions presented in Ames and Kreidenweis (1996) were fit with single mode lognormal curves, assumed to capture the accumulation mode. Derived lognormal size parameters were compared to the size parameters calculated in Ames and Kreidenweis (1996), where no size distribution function was assumed. Scatter plots of each parameter will be presented in the following figures.

Section A1.1. Total Number Concentration (cm^{-3})

Scatter plots of total number concentration (cm^{-3}) derived in Ames and Kreidenweis (1996) (denoted OPC), and lognormal fit total number concentration are found in Figures A1.1 (a,b). Figure A1.1a presents comparisons of dry (<15% RH) total number concentration and Figure A1.1b presents comparisons of wet (>15% RH) total number concentration. Data fall between the 1:1 and 2:1 lines as shown, with the lognormal fit total number concentration higher. Figure 3.1.2 in Chapter 3 demonstrated a lognormal curve capturing number concentration corresponding to sizes smaller than the measuring range of the ASASP-X (< 0.1 μm). Including these smaller sizes resulted in larger number concentrations for the lognormal fits. Error bars for total number concentration were smaller than the plotting symbols and therefore were not plotted. Discussion of uncertainty calculations can be found in Section A1.6.

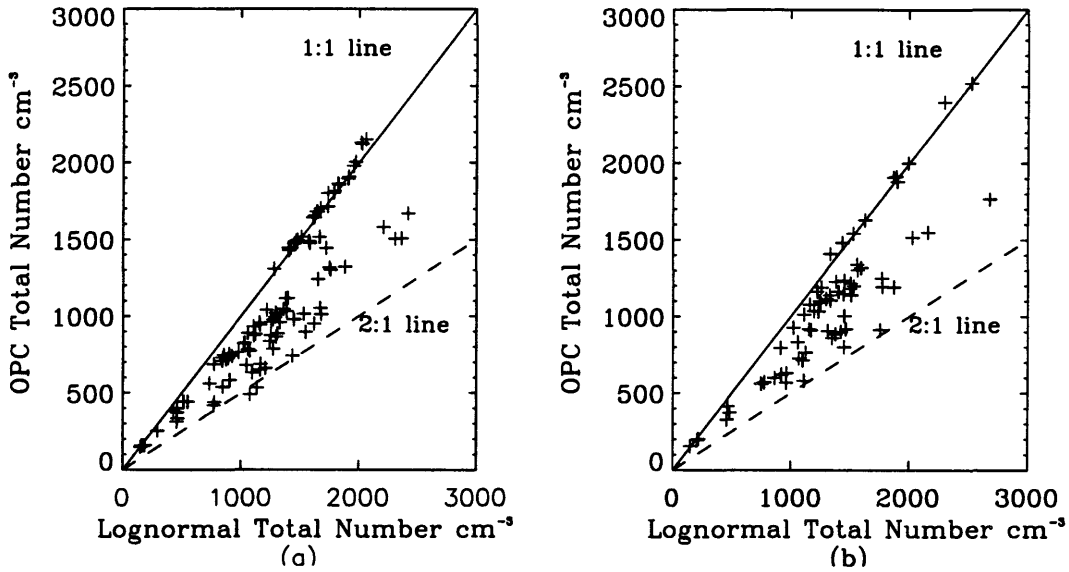

Figure A1.1(a,b) (a) Dry and (b) wet total number concentration (cm^{-3}) comparisons between OPC and lognormal fit.

Section A1.2 Accumulation Mode Volume Concentration ($\mu m^3\ cm^{-3}$)

Accumulation mode volume concentrations were calculated using the equations from Section 3.1. Figures A1.2(a,b) present scatter plots of wet and dry accumulation mode volume concentrations for lognormal and OPC values. The OPC integrated accumulation mode volume was larger for both the wet and dry cases. These larger volumes resulted from a combination of the lognormal curve smoothing through the size distribution, and the accumulation mode cut-off diameter used in the analysis in Ames and Kreidenweis (1996). The peak of the volume distribution was smoothed by the lognormal curve (and consequently not included in the lognormal integrated volume). For the wet volume distributions (Figure A1.2b), the accumulation mode cut-off diameters from Ames and Kreidenweis (1996) analyses were typically smaller than the lognormal cut-off diameters, resulting in larger volume concentrations for the single mode lognormal accumulation mode. This added volume compensated for the volume missed by the

lognormal smoothing. The agreement for the wet case was therefore closer to the 1:1 line than for the dry case.

Section A1.3. Volume Median Diameter ($D_{pg,v}$) (μm)

Both wet and dry volume mean (OPC) and median (lognormal) diameter comparisons showed larger OPC diameters for $D_p < 0.25$ μm, and conversely, larger lognormal fit diameters for $D_p > 0.4$ μm (see Figures A1.3.1a,b). Depending on the values of σ_g and $D_{pg,n}$, the volume median diameter ($D_{pg,v}$) shifted to either large or small sizes in comparison to the OPC diameters.

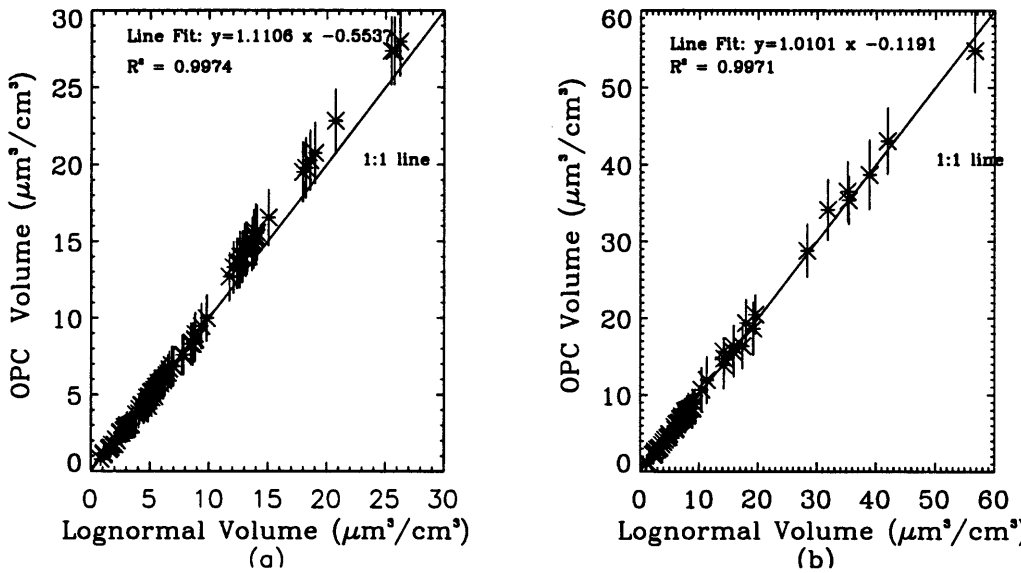

Figure A1.2(a,b) (a) Dry and (b) wet accumulation mode volume concentrations from lognormal fits and the OPC.

The decrease in volume concentration at $D_p \sim 0.4$ μm is a known effect of OPC measurements, and was discussed in Section 3.1. For distributions with small number median diameter, the drop in the distribution around $D_p = 0.4$ μm was noticeable, mainly because there was less number concentration beyond this size range. For the wet distributions, enough number and volume existed beyond $D_p = 0.4$ μm, resulting in significant amounts of volume at these sizes, and therefore no decrease in the distribution

around 0.4 μm (see Figure A1.3.2). The study average experimental uncertainty in wet $D_{pg,v}$ was ± 0.09 μm, and ± 0.08 μm for dry $D_{pg,v}$.

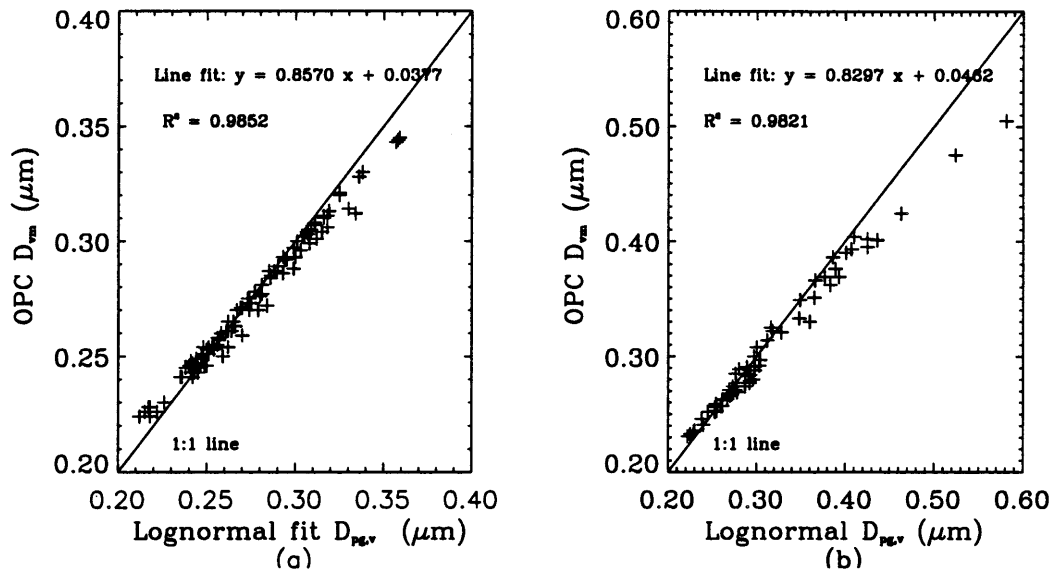

Figure A1.3.1(a,b) (a) Dry and (b) wet volume median diameters from lognormal fits and the OPC.

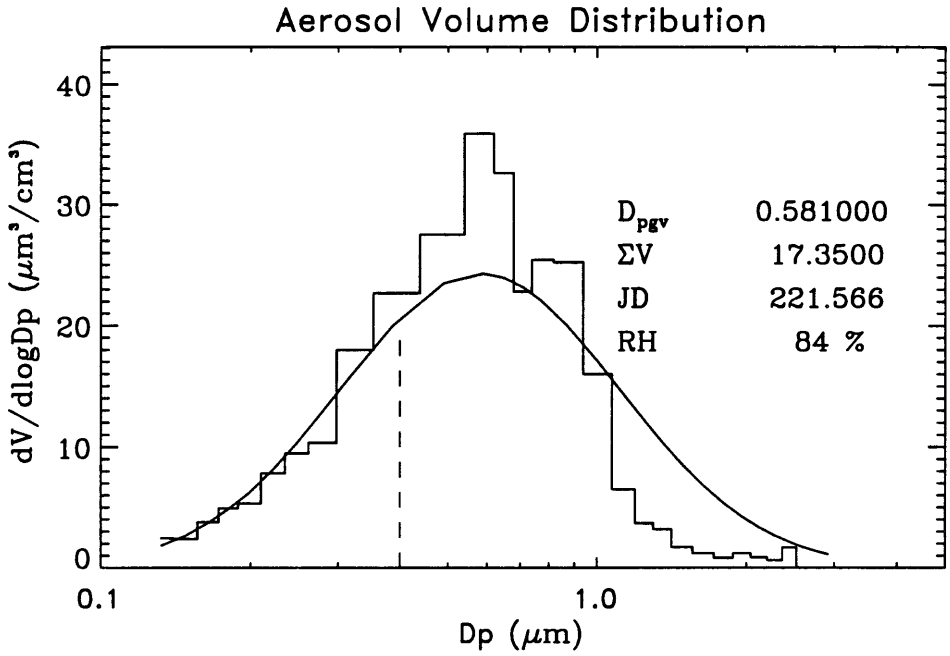

Figure A1.3.2. Example SEAVS wet volume distribution demonstrating the significant amounts of volume at larger diameters. The dashed line corresponds to 0.4 μm.

Section A1.4. Geometric Standard Deviation (σ_g)

Figures A1.4 (a,b) present scatter plots of dry and wet geometric standard deviations from OPC and lognormal analyses. For both cases, σ_g was larger for the OPC size distributions. Because the number median diameter was not calculated for the OPC case, it was difficult to discern why the OPC geometric standard deviations were larger. It was suspected that because the lognormal fit included number concentration in sizes smaller than the ASASP-X measuring range, the geometric standard deviation of the distribution would be affected. When the entire accumulation mode was represented by the lognormal fit, the distributions narrowed considerably.

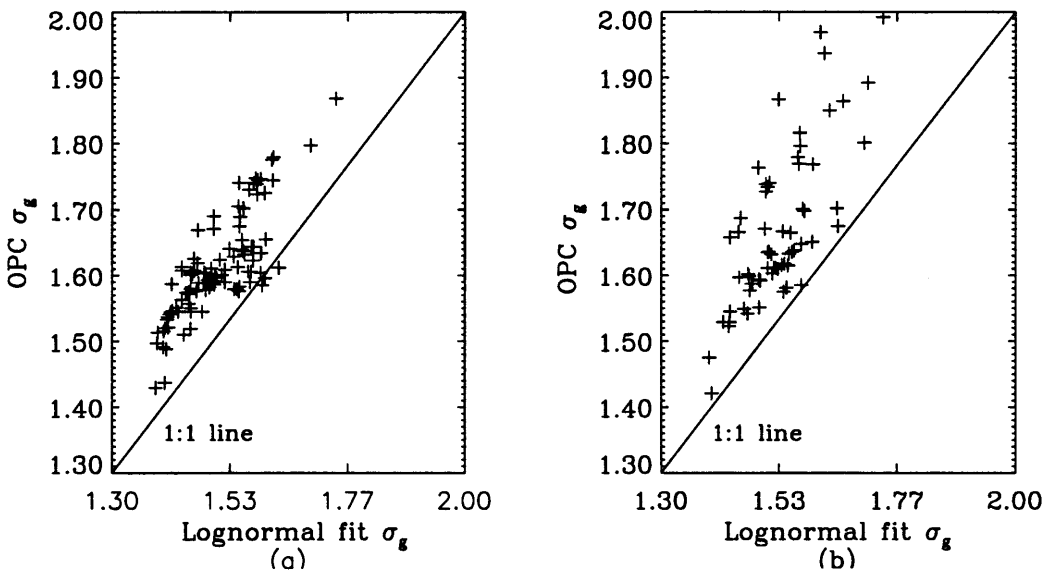

Figure A1.4(a,b) (a) Dry and (b) wet geometric standard deviation for lognormal fits and OPC size distributions.

Section A1.5. Particle Hygroscopicity (D/D_o)

The two methods presented in Chapter 3 for calculating aerosol growth due to water absorption were used to calculate hygroscopicity estimates. Comparisons of these results from OPC and lognormal size parameters, both for which the rural aerosol model was applied, are shown in Figures A1.5(a,b). The results for D/D_o when using lognormal parameters were larger for the diameter ratio method, but in good agreement for the volume ratio method. As seen in Figures A1.3(a,b), $D_{pg,v}$ was larger for the lognormal case, with a greater trend for the wet case. This greater bias toward the lognormal fit wet parameter could lead to larger values of D/D_o for the lognormal fit case. The comparisons of volume ratios for the OPC and lognormal fit fell close to the 1:1 line, consistent with the individual volume comparisons (Figures A1.2a,b).

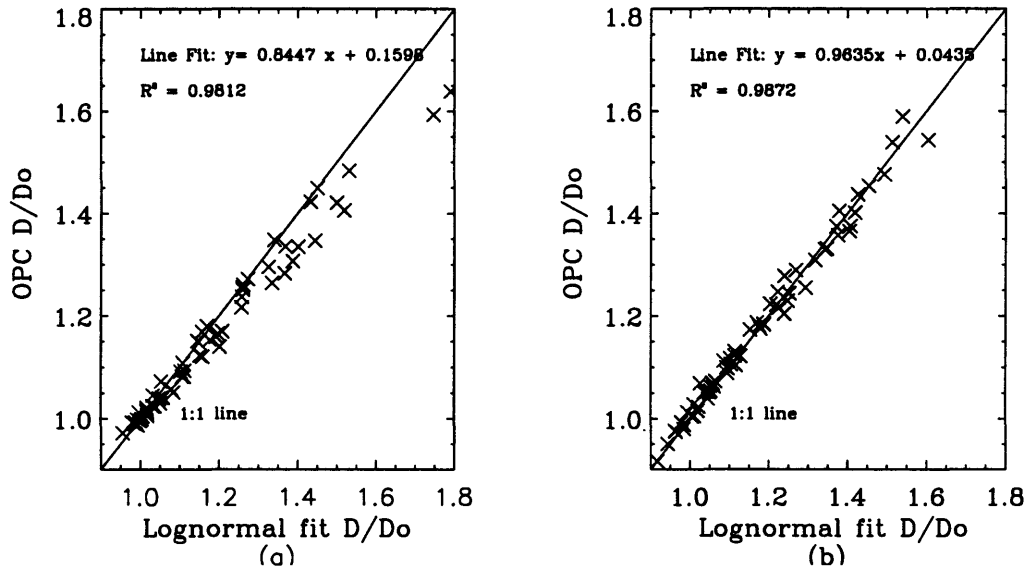

Figure A1.5(a,b) Hygroscopicity comparisons for (a) diameter ratios and (b) volume ratios

Section A1.6. Experimental Uncertainty

Experimental uncertainty in number and volume concentrations and mean volume diameters derived in Ames and Kriedenweis (1996) were calculated in the following way. Consider the volume concentration calculated for a single bin:

$$V_i = \frac{\pi}{6} N_i D_{pm,i}^3 \qquad \text{(A1.6.1)}$$

where $D_{pm,i}$ (μm) is the midpoint diameter of the bin, and N_i is the bin number concentration (cm^{-3}). Considering uncertainty in both the number concentration and midpoint diameter, the uncertainty in bin volume concentration can be written as equation A1.6.2

$$\partial V_i = \left[\left(\frac{\pi}{2} D_{pm,i}^2 N_i \right)^2 (\delta D_{pm,i})^2 + \left(\frac{\pi}{6} D_{pm,i}^3 \right)^2 (\delta N_i)^2 \right]^{1/2} \qquad \text{(A1.6.2)}$$

where the units result in $\mu m^3\ cm^{-3}$ as expected. The uncertainty in midpoint diameter (equation A1.6.3) resulted from experimental uncertainty (σ_{exp}) as well as uncertainty in refractive index used in the data inversion (σ_m). Experimental uncertainty was derived from the spread in response of a monodisperse aerosol measured with the ASASP-X, and was taken to be ~ 0.02 μm. The uncertainty in the effects of refractive index on size varied for wet and dry aerosol, and ranged from σ_m = 0.01- 0.08 (μm).

$$\partial D_{pm,i} = \left[\sigma_{exp}^2 + \sigma_m^2 \right]^{1/2} \qquad \text{(A1.6.3)}$$

The uncertainty in number concentration was estimated from the duration of measurement (t), uncertainty in counts (c), and flow rate (Q) using equation A1.6.4,

$$\partial N_i = \left[\left(\frac{1}{Qt}\right)^2(\delta c_i)^2 + \left(\frac{-c_i}{Q^2 t}\right)^2(\delta Q)^2\right]^{1/2} \qquad \text{(A1.6.4)}$$

where δQ was estimated from the standard deviation of flow measurements, and the uncertainty in counts was assumed from Poisson statistics to be $(c)^{1/2}$. Equation (A1.6.4) can be simplified to equation (A1.6.5) by recalling that number concentration can be written as

$$N = \frac{c}{Qt}$$
$$\partial N_i = \left[\frac{N_i}{Qt} + \frac{N_i^2}{Q^2}(\delta Q)^2\right]^{1/2} \qquad \text{(A1.6.5)}$$

In Ames and Kreidenweis (1996), the volume mean diameter was calculated by equation (A1.6.6), rewritten here in natural logarithms.

$$D_{pg,v} = \exp\left[\frac{\sum V_i \ln D_{pm,i}}{\sum V_i}\right] \qquad \text{(A1.6.6)}$$

For simplicity, equation (A1.6.6) will be written as equation (A1.6.7)

$$D_{pg,v,i} = \exp[C_i] \qquad \text{(A1.6.7)}$$

where

$$C_i = A_i / B_i$$

and

$$A_i = V_i \ln D_{pm,i}$$

$$B_i = V_i .$$

The uncertainties in the quantities *A* and *B* are:

$$\partial A_i = \left[\left(\ln D_{pm,i} \right)^2 \left(\delta V_i \right)^2 + \left(\frac{V_i}{D_{pm,i}} \right)^2 \left(\delta D_{pm,i} \right)^2 \right]^{1/2} \qquad \text{(A1.6.8)}$$

$$\partial B_i = \delta V_i$$

Uncertainty in volume concentration and diameter were calculated with equations (A1.6.2) and (A1.6.3), respectively. The uncertainty in *C* was determined by equation (A1.6.9).

$$\partial C_i = \left[\left(\frac{1}{B} \right)^2 (\partial A)^2 + \left(\frac{-A}{B} \right)^2 (\partial B)^2 \right]^{1/2} \qquad \text{(A1.6.9)}$$

The uncertainty in the mean volume diameter was then calculated by equation (A1.6.10).

$$\partial D_{pg,v} = \exp(C)\, \partial C \qquad \text{(A1.6.10)}$$

These calculations resulted in an average volume mean diameter experimental uncertainty of 0.09 μm for wet diameters, and 0.08 μm for dry diameters for the study period.

Part II. Sensitivity of Instrument Calibration

The effects of instrument calibration on derived size parameters from the ASASP-X data inversion will be investigated in this section. The results in this thesis (denoted H&K) were inverted with the calibration derived in Section 2.2. These results were compared to those reported in Ames and Kreidenweis (1996) (denoted A&K) for which a different calibration was applied. For both cases, the Shettle and Fenn (1979) rural aerosol model and the lognormal size functions were assumed. Size parameters were affected by the assumed calibration, resulting in smaller size parameters and hygroscopicity estimates when applying the calibration derived in this thesis. Possible reasons for this will be discussed.

Section A2.1. Total Number Concentration (cm^{-3})

Both wet and dry total number concentration comparisons are presented in Figures A2.1 (a,b). For both wet and dry cases, the calibration in Ames and Kreidenweis (1996) resulted in larger number concentration. This bias may be due to the differences in assigning and averaging counts to specific bins for the two methods (see Section 2.3 for a discussion of averaging counts).

Section A2.2. Accumulation Mode Volume Concentration ($\mu m^3\ cm^{-3}$)

Accumulation mode integrated volume comparisons are presented in Figures A2.2(a,b). Differences in volume concentrations were noticeable, with the A&K calibration resulting in much larger volume concentrations, especially for the wet cases. These larger volumes were most likely an effect of the diameters assigned to size channels for each calibration. As discussed in Section 2.3, instrument calibration was performed with PSL particles. The PSL number distributions inverted with both calibrations were fit

with lognormal size functions, as seen in Figure 2.3.3. The calibration from Ames and Kreidenweis (1996) resulted in an average PSL number median diameter over the study of $D_p = 0.449 \pm 0.007$ μm for a 0.41 μm diameter PSL particle. The calibration in this thesis resulted in an average PSL number median diameter of 0.413 ± 0.007 μm for a 0.41 PSL particle. The difference in this PSL number median diameter for the two calibrations suggested that diameters corresponding to size bins for the A&K calibration were larger when compared to the H&K calibration, resulting in particles being sized with larger diameters. Hence, larger integrated volume concentrations for the A&K calibration resulted.

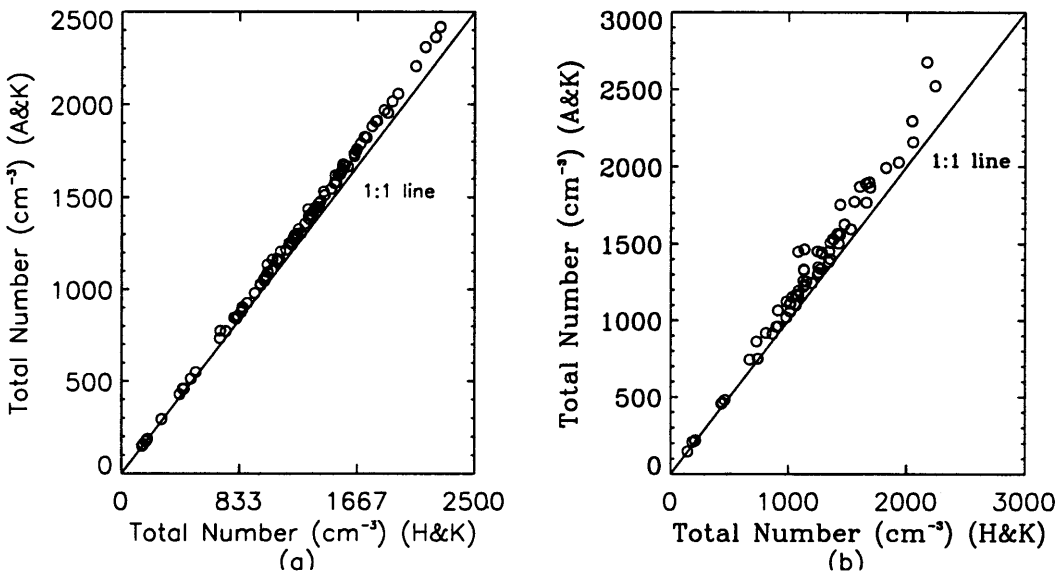

Figure A2.1(a,b) (a) Dry and (b) wet total number concentration derived with two different instrument calibrations.

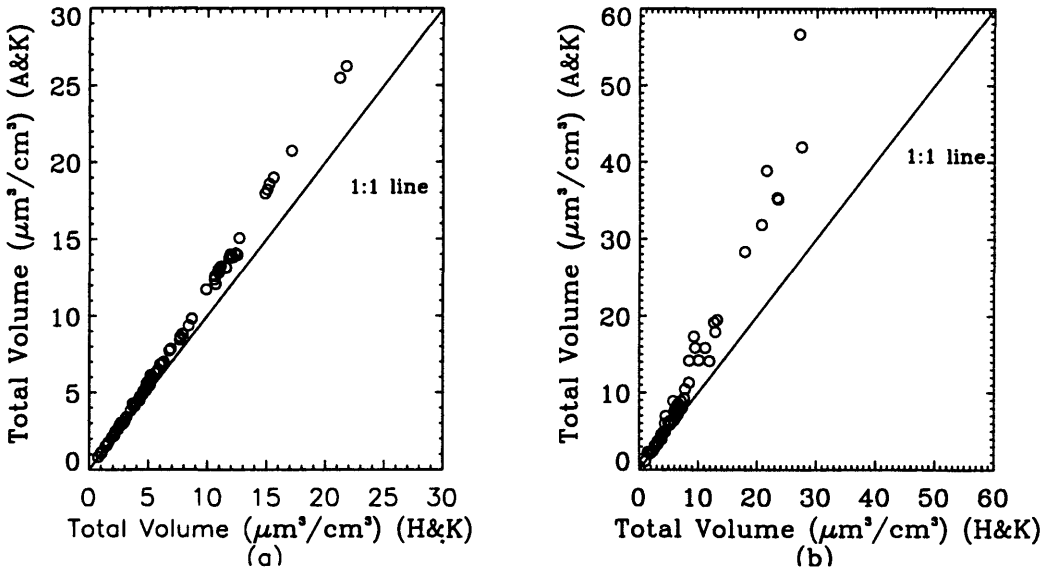

Figure A2.2(a,b) (a) Dry and (b) wet accumulation mode volume concentration for two different instrument calibrations.

Section A2.3. Volume Median Diameter ($D_{pg,v}$) (μm)

Figures A2.3 (a,b) demonstrate the differences in volume median diameter (μm) for the two calibration methods. The calibration in A&K resulted in much larger values of $D_{pg,v}$ than the calibration in this thesis. The reason for this would be the same as in the previous section. Particles sized with larger diameters for the A&K calibration would result in larger volume median diameters.

Section A2.4. Number Median Diameter ($D_{pg,n}$) (μm)

Scatter plots of number median diameter (Figures A2.4 a,b) demonstrate different trends than those for volume concentration and volume median diameter, with the H&K calibration having larger diameters at smaller sizes. Differences in geometric standard deviation, σ_g, presented in Figures A2.5 (a,b) could contribute to the difference. For a distribution with a larger geometric standard deviation, the number median diameter shifted slightly to smaller sizes. Several A&K distributions with smaller number median diameter

also had much larger values of σ_g when compared to parameters derived in this thesis for the same distributions.

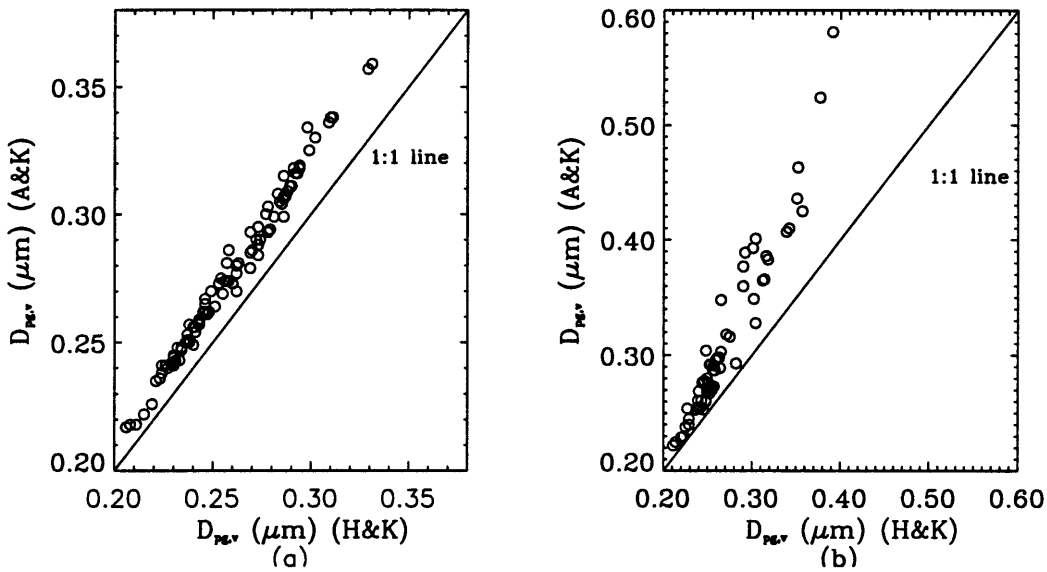

Figure A2.3(a,b) (a) Dry and wet (b) volume median diameters for two different instrument calibrations.

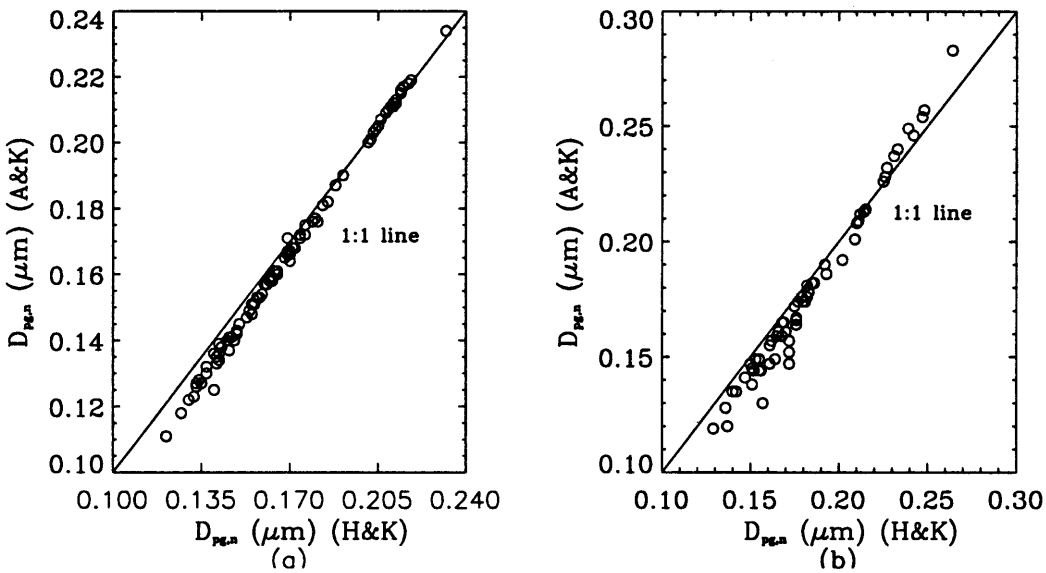

Figure A2.4(a,b) (a) Dry and (b) wet number median diameters for two different instrument calibrations.

Section A2.5. Geometric Standard Deviation (σ_g)

As discussed in the previous section, the geometric standard deviation values for the A&K calibration were consistently larger than when using the calibration in this thesis (see Figures A2.5 a,b). Two reasons most likely account for this trend. The different calibrations resulted in different diameters assigned to size channels, with different procedures for averaging counts between these size channels resulting in different shapes of distributions. A combination of these effects resulted in narrower number distributions for the calibration in this thesis.

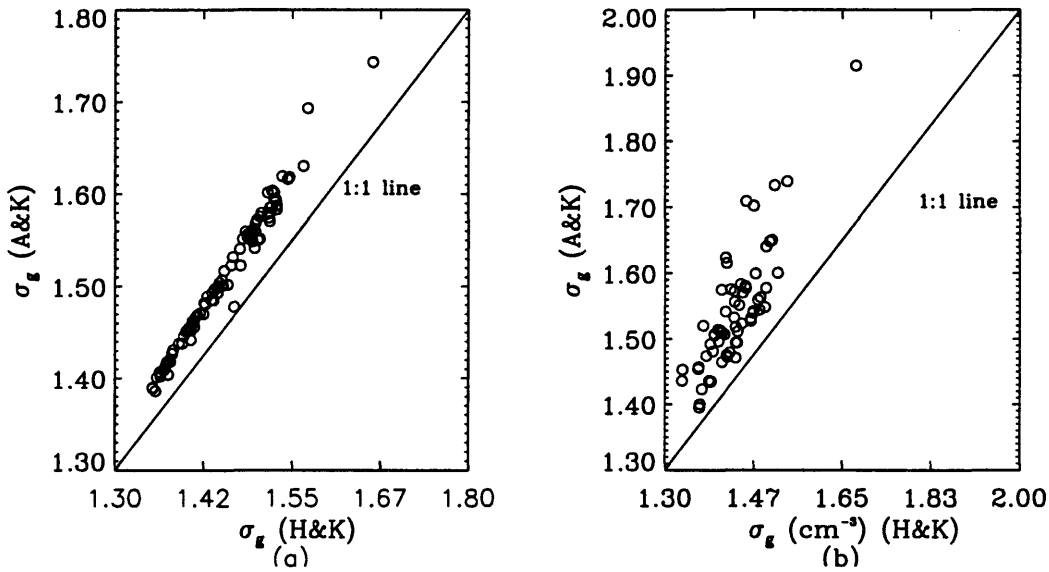

Figure A2.5(a,b) (a) Dry and (b) wet geometric standard deviation for two different instrument calibrations.

Section A2.6. Particle Light Scattering (b_{sp})

Light scattering coefficients (b_{sp}) were calculated with size parameters derived from both calibrations. Figures A2.6.1 (a,b) illustrate comparisons of both wet and dry b_{sp}. The A&K calibration resulted in larger scattering for both the wet and dry cases. The size parameters required for the calculation for b_{sp} were $D_{pg,n}$, σ_g, and number concentration. Although the values of $D_{pg,n}$ were slightly smaller for the A&K calibration, σ_g and total

number concentrations were larger, with a combined effect resulting in larger values of light scattering coefficients for the A&K calibration.

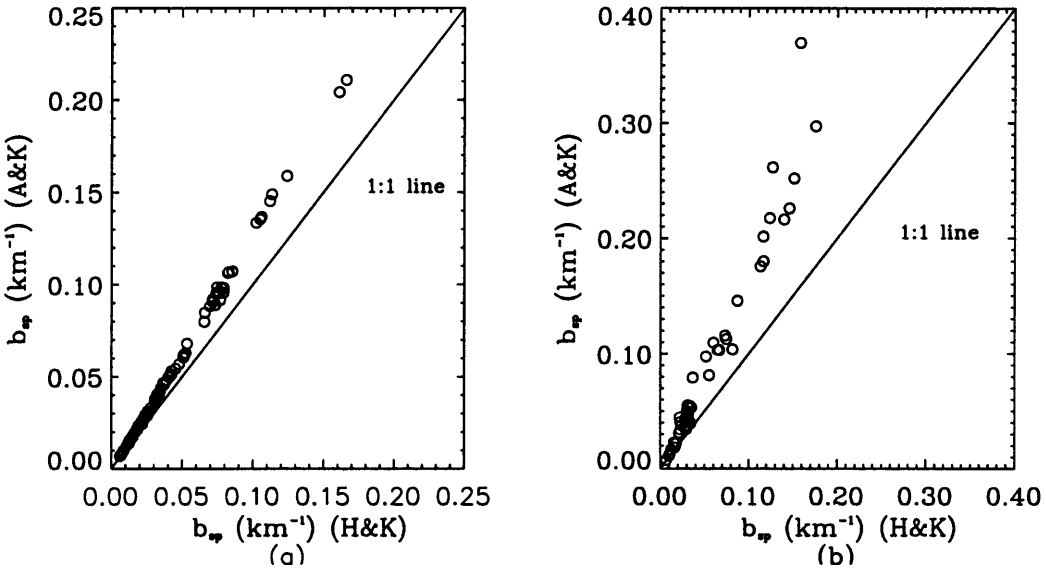

Figure A2.6(a,b) (a) Dry and (b) wet light scattering coefficients for two different instrument calibrations.

Section A2.7. Particle Hygroscopicity (D/D_o)

Calculations of hygroscopicity were made using the same pairs of dry and humidified size distributions discussed in Chapters 3 and 6. Figures A2.7.1 (a,b) present scatter plots of hygroscopicity calculated from ratios of accumulation mode volume, and volume median diameter, respectively, for both calibration methods. As would be expected from the trend in size parameters, the A&K calibration resulted in larger values of hygroscopicity when compared to the values derived from the H&K calibration. The scattering growth curve (b/b_o) comparison is shown in Figure A2.7.2, with larger values derived from the A&K calibration, consistent with observed trends in b_{sp}.

The results in Part II suggest that the instrument calibration had a significant effect on the derived results when compared to the sensitivity studies reported in Part I. It will be shown in Appendix B that variations in aerosol chemical composition and refractive index have less on an effect on the derived results than the instrument calibration.

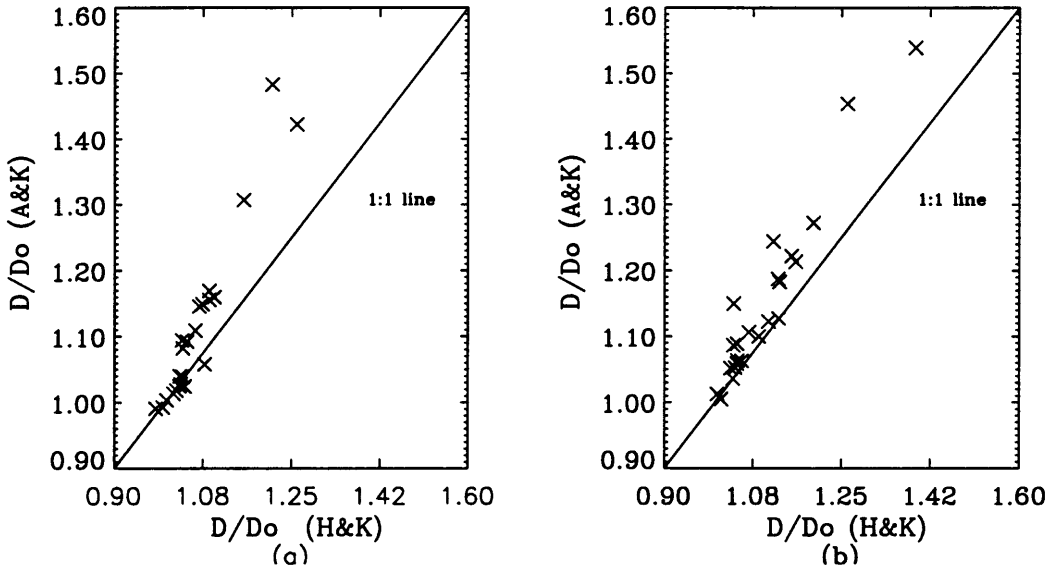

Figure A2.7.1(a,b) Comparisons of hygroscopicity estimates using (a) diameter ratios and (b) volume ratios for two different instrument calibrations.

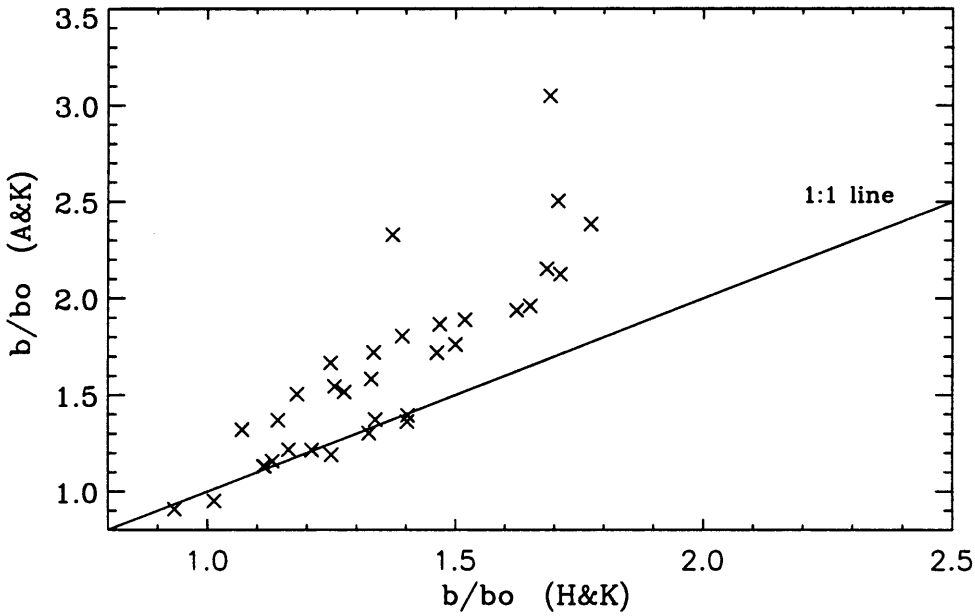

Figure A2.7.2 Comparisons of b/b_o estimates for two different instrument calibrations.

APPENDIX B.

Part I: Sensitivity to Daily Varying Refractive Index

In Chapter 3, a rural aerosol model (Shettle and Fenn, 1979) was used to characterize the aerosol refractive index as a function of relative humidity. Chapters 4-6 detailed the calculation and application of daily varying wet and dry refractive indices to the data inversion. In Appendix B, sensitivity to these choices will be presented. For these results, the calibration derived in this thesis was used to invert data. In Part I of Appendix B, the effects of applying a daily varying refractive index will be investigated by comparing lognormal size parameters derived from size distributions inverted with both the daily varying and rural aerosol model refractive indices. Only dry (RH<15%) size parameters were compared, as it was assumed that the differences in the wet cases scaled in a similar way to the dry cases due to the linear property of the scaling procedure used in the data inversion.

Section B1.1. Total Dry Number Concentration (cm^{-3})

Figure B1.1 presents a scatter plot of dry (<15%) total number concentration for the rural aerosol model refractive index (m=1.530 for RH < 15%), and the daily varying dry refractive indices used in the data inversion (see Chapters 4-6). The good agreement was expected because the count averaging technique was the same.

Section B1.2. Dry Accumulation Mode Volume Concentration ($\mu m^3\ cm^{-3}$)

Accumulation mode volume concentration was calculated from number distributions for both refractive index cases, and compared in Figure B1.2. Divergence from the 1:1 line was noticeable for large values of volume concentration. This trend was expected because

the diameters assigned to size bins were larger for the varying refractive index case than for the rural aerosol model of refractive index.

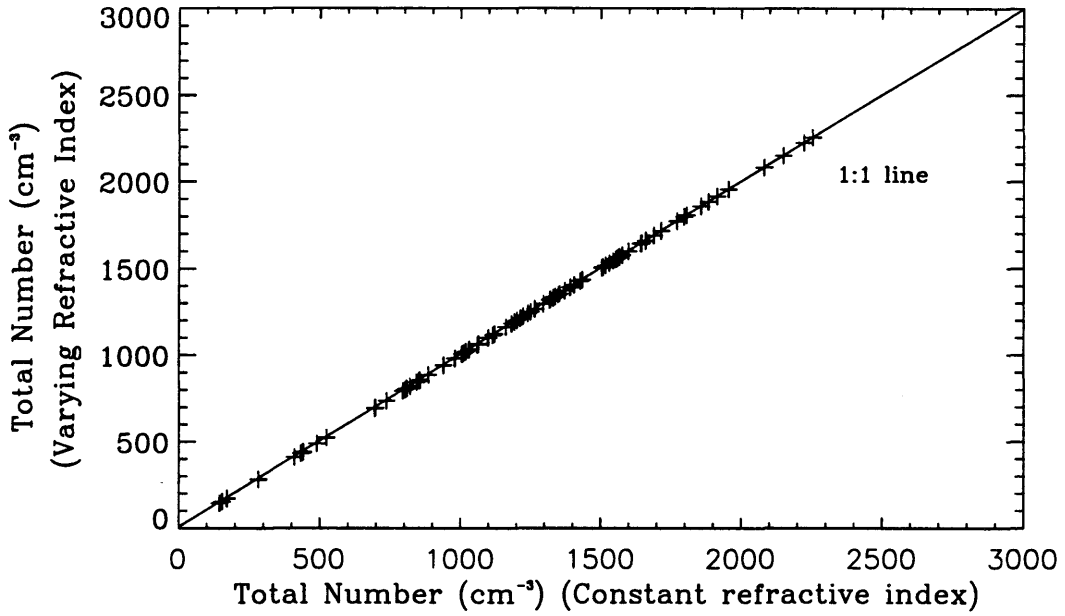

Figure B1.1 Comparisons of dry total number concentration for constant and daily varying refractive index.

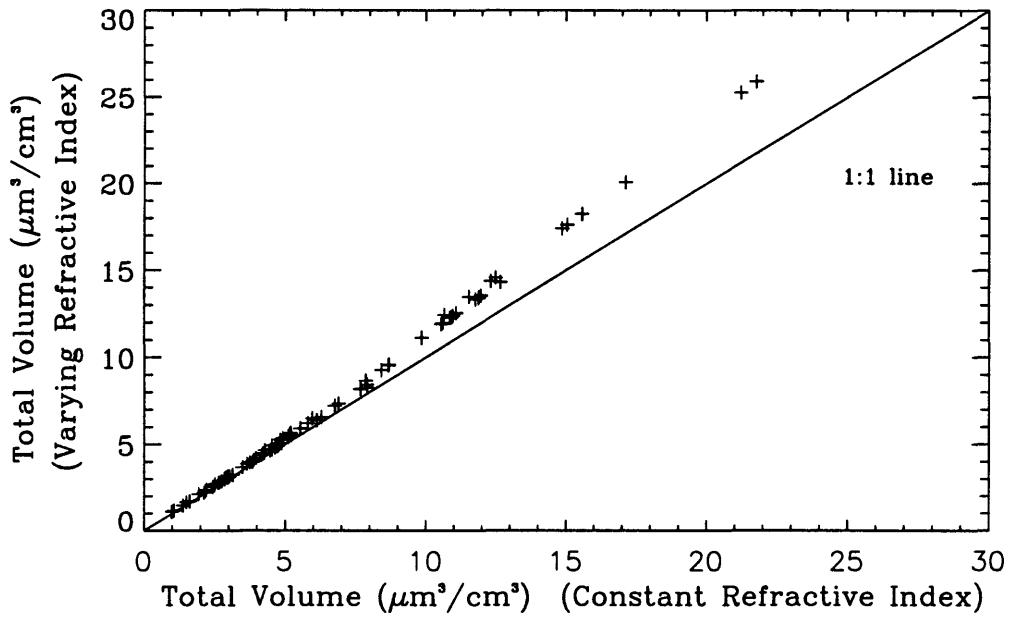

Figure B1.2 Comparisons of dry accumulation mode volume concentration for constant and daily varying refractive index.

Section B1.3. Dry Number Median Diameter ($D_{pg,n}$) (μm)

Comparisons of number median diameter are presented in Figure B1.3. Larger values of $D_{pg,n}$ resulted for the varying refractive index case. This was expected because the number distribution was shifted to larger sizes for smaller refractive index. As will be seen in Figure B1.5, the shape of the distribution remained the same regardless of the refractive index values. The differences in $D_{pg,n}$ therefore were due mainly to a shifting of the entire distribution to larger sizes.

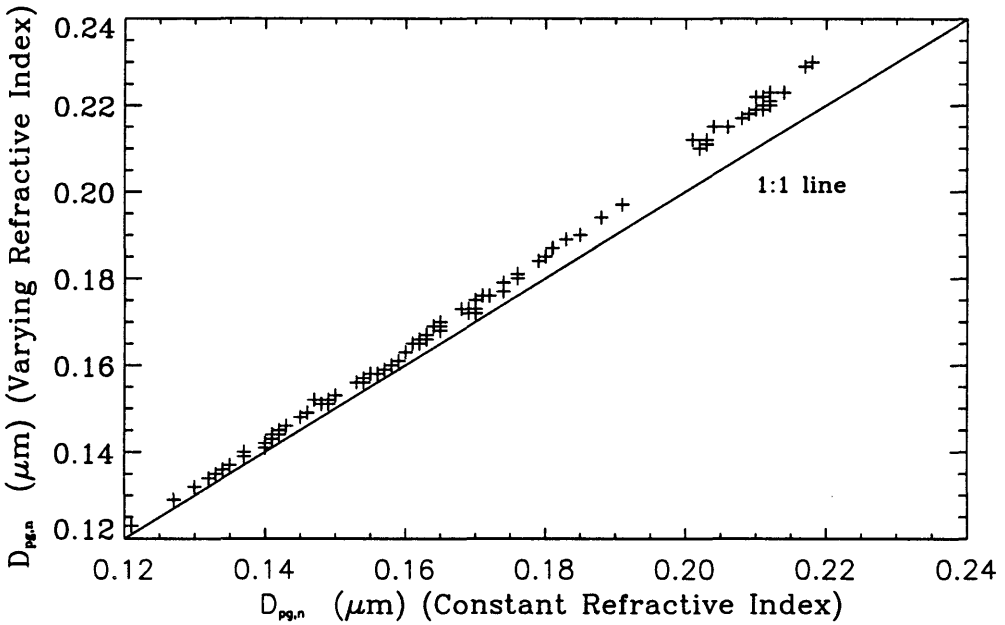

Figure B1.3 Comparisons of dry number median diameter for constant and daily varying refractive index.

Section B1.4. Dry Volume Median Diameter ($D_{pg,v}$) (μm)

Figure B1.4 presents the comparison of volume median diameter for the daily varying refractive index and rural aerosol model applied in the data inversion. Larger values for the daily varying refractive index case existed for this size parameter as well, due a shifting of the distribution to larger sizes.

Section B1.5. Dry Geometric Standard Deviation (σ_g)

The shape of the distribution did not change for the two sets of refractive indices applied (Figure B1.5). This agreement was expected because the calibration did not change for the two cases, with number being averaged and assigned to similar size bins for both cases. The diameters assigned to these size bins did change, however, based on refractive index.

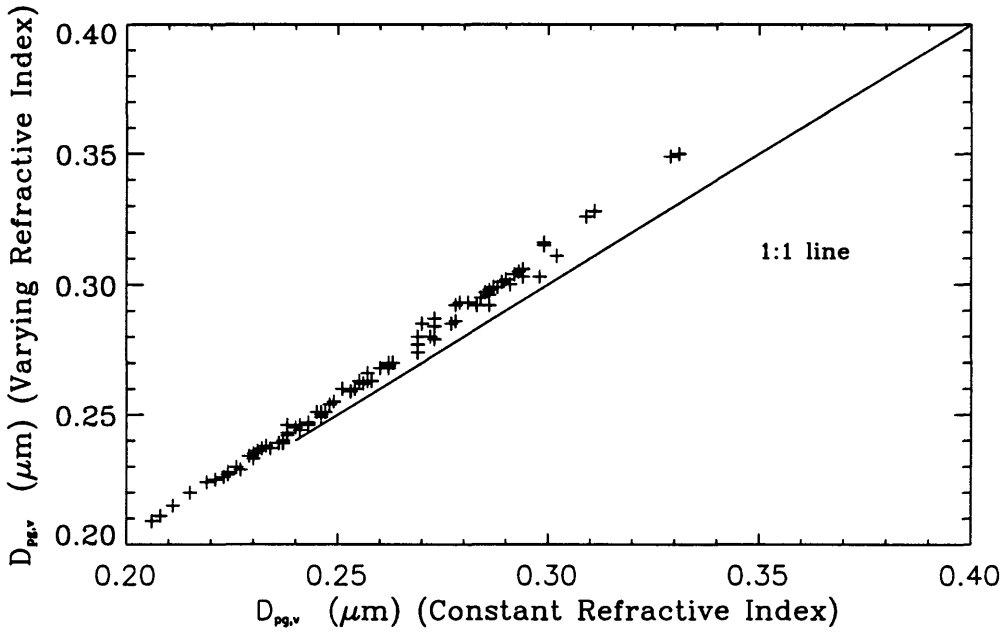

Figure B1.4 Comparisons of dry volume median diameter for constant and daily varying refractive index.

Section B1.6. Particle Light Scattering (b_{sp})

Light scattering coefficients were calculated with daily varying and rural aerosol model refractive indices. Figure B1.6 presents a comparison of dry b_{sp} for these cases. The trend suggests that rural aerosol model refractive index resulted in slightly larger values of scattering, as was reported in Section 6.3. The effect of larger refractive index from the rural aerosol model in the scattering calculation outweighed the effect of larger size

parameters (such as the number median diameter) corresponding the daily varying refractive index case.

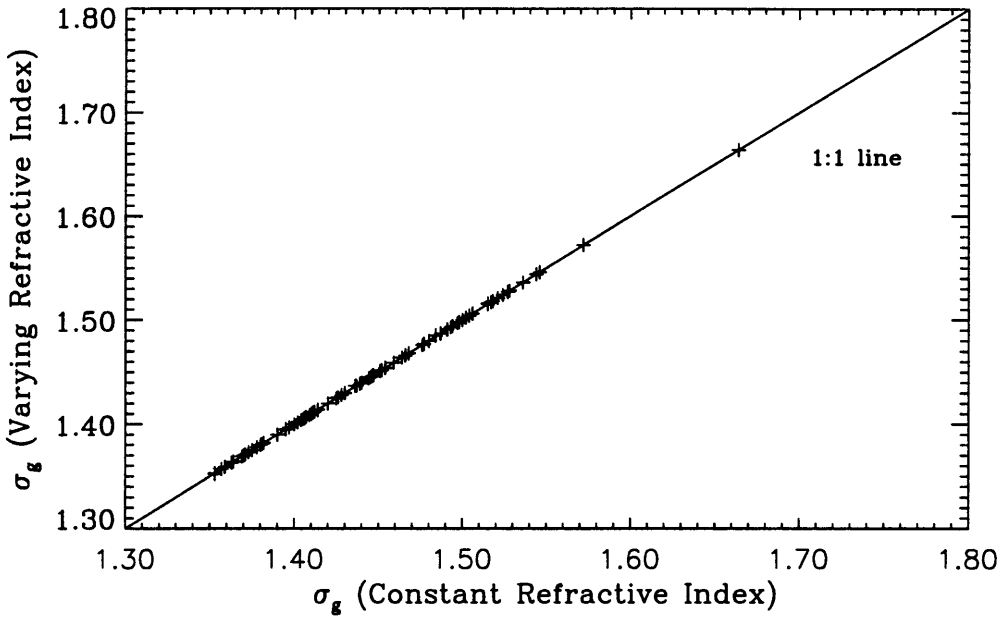

Figure B1.5 Comparisons of dry geometric standard deviation for constant and daily varying refractive index.

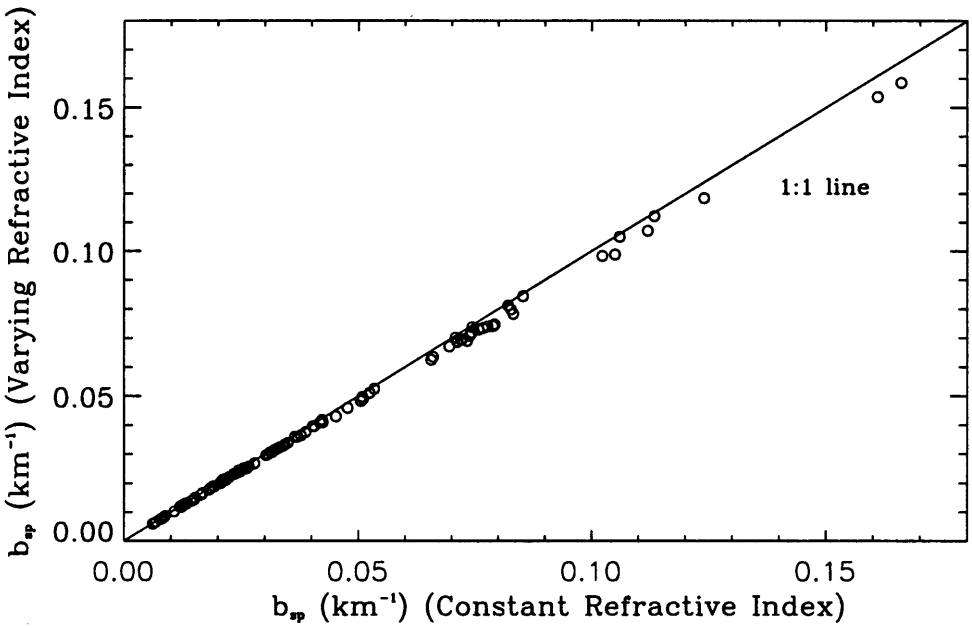

Figure B1.6 Comparisons of dry b_{sp} for daily varying and rural aerosol model refractive index.

Section B1.7. Particle Hygroscopicity (D/D_o)

Although Sections B1.1-B1.6 reported an increase in size parameters for daily varying refractive indices, Figures B1.7.1(a,b) suggest that ratioing these values nearly canceled these effects. Comparisons of hygroscopicity estimates using the two sets of refractive index are presented in Figures B1.7(a,b), showing scatter around the 1:1 line. Similar comparisons for the light scattering growth curve (b/b_o) can be found in Figure B1.7.2. Differences in light scattering coefficients nearly canceled, resulting in fairly good agreement between daily varying and non-varying refractive index. These results suggest that although knowledge of the varying chemical composition of aerosol was important for deriving size parameters, it was not critical in the calculation of hygroscopicity.

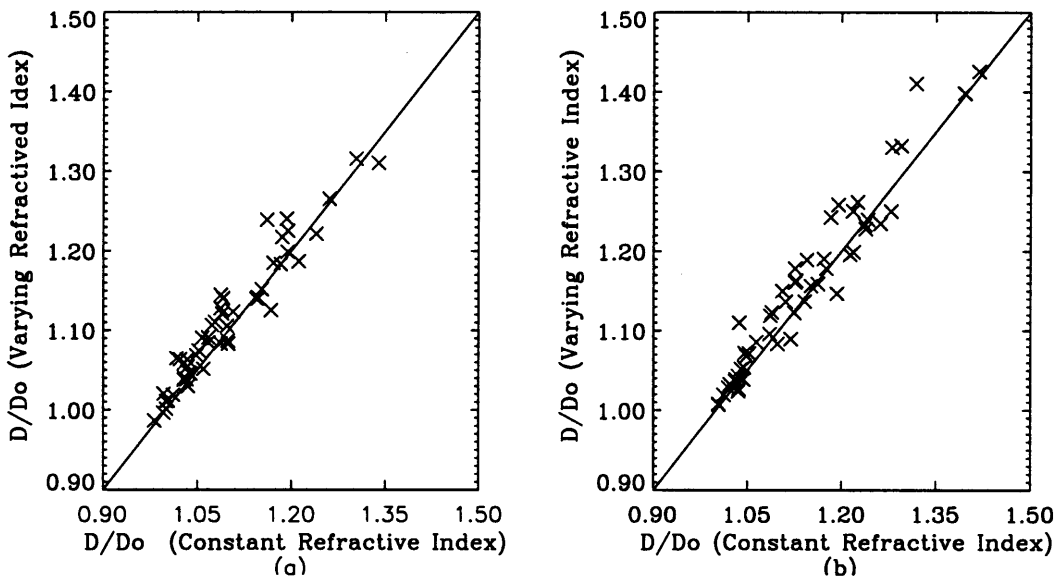

Figure B1.7.1(a,b) Comparisons of hygroscopicity estimates using (a) diameter ratios and (b) volume ratios for both cases of refractive index.

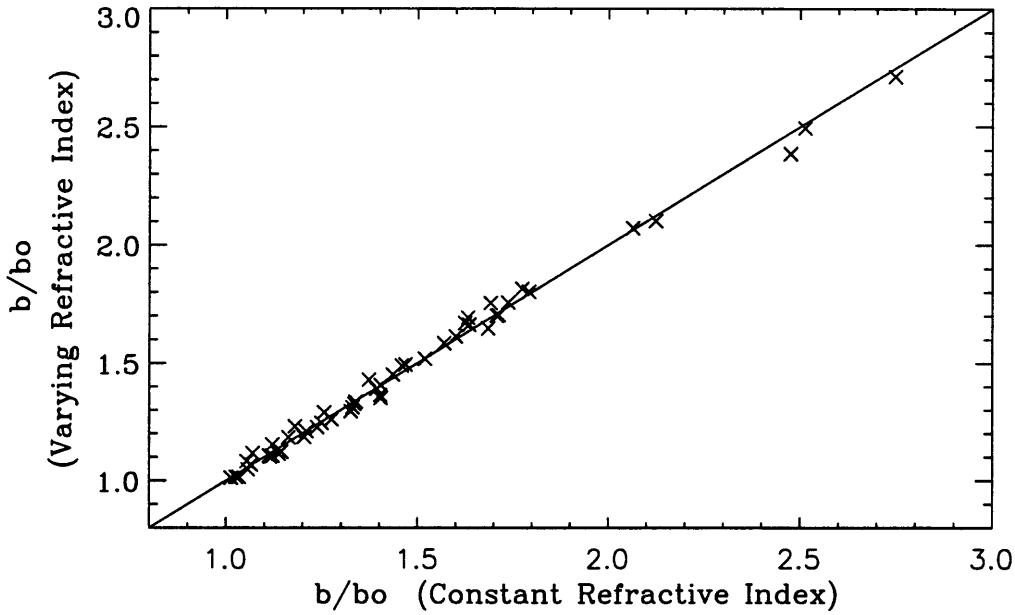

Figure B1.7.2 Comparisons of b/b_o for both cases of refractive index.

Part II. Sensitivity of the Effects of Elemental Carbon

Sensitivity studies performed on the effects of including elemental carbon as a part of the aerosol chemical composition will be reported in this section. Calculations were made for absorbing aerosol by including elemental carbon in the calculations of refractive index (Section 4.5). Because the scaling procedure was based on real refractive index, the resulting size parameters changed very little due to the small change in real refractive index between the absorbing and non-absorbing cases (see Figure 4.5.1). Inclusion of the imaginary part of the refractive index in the scaling procedure was expected to yield larger sizes for diameters above 0.4 μm, therefore, calculations of size parameters underestimated particle sizes above 0.4 μm.

Section B2.1. Particle Light Scattering and Extinction (b_{sp}, b_{ext})

Light extinction and scattering calculations were performed with the complex refractive indices derived in Section 4.5. Figure B2.1a presents comparisons of b_{ext} for the cases of absorbing and non-absorbing aerosol. The resulting trend was expected; for the absorbing aerosol case, the light extinction coefficient increased slightly due to the added removal of light by absorption. The light scattering coefficient was slightly less for the absorbing case (Figure B2.1b) due to larger values of size parameters for the non-absorbing aerosol. Comparisons of the light scattering growth curve, b/b_o, are found in Figure B2.2, with smaller values of b/b_o for absorbing aerosol.

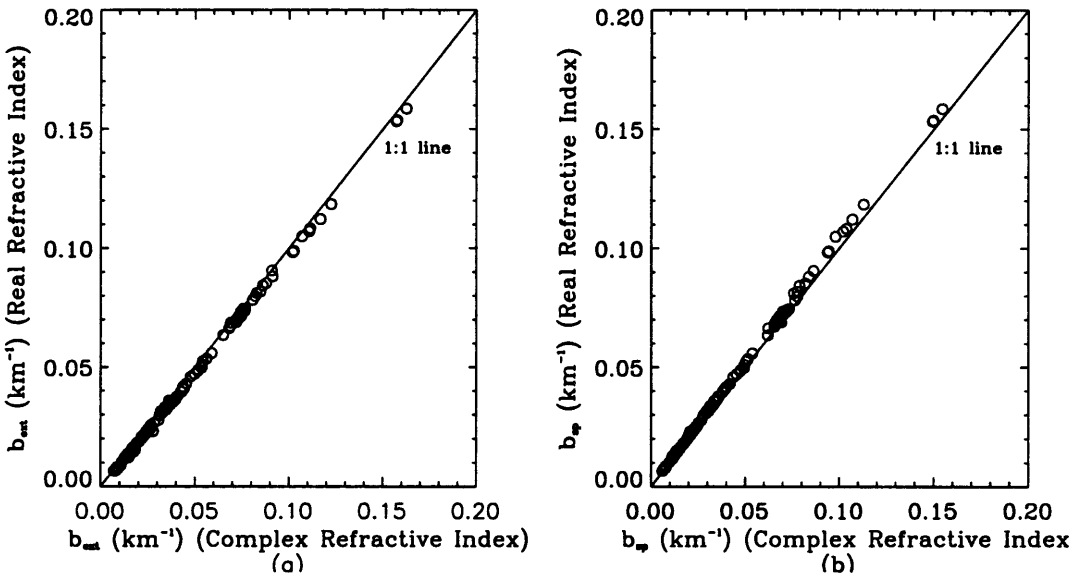

Figure B2.1(a,b) Comparisons of (a) dry b_{ext} and (b) dryb_{sp} for absorbing and non-absorbing aerosol.

Including elemental carbon in the aerosol mass and refractive index calculations did not appear to have a large effect on size parameters, hygroscopicity, or light scattering. Modifying the scaling procedure to include the imaginary part of the refractive index would be expected to produce larger effects on derived results.

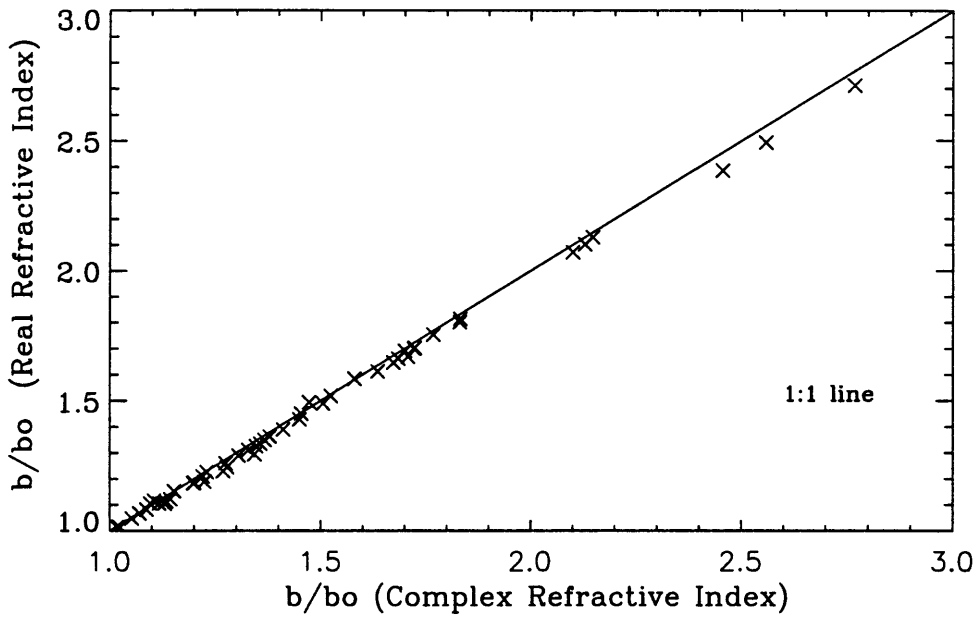

Figure B2.2 Comparisons of b/b_o for absorbing and non-absorbing aerosol.